Spatially Resolved Optical Measurements on Supported Metal Particles and Oxide Surfaces with the STM

Hadj Mohamed Benia

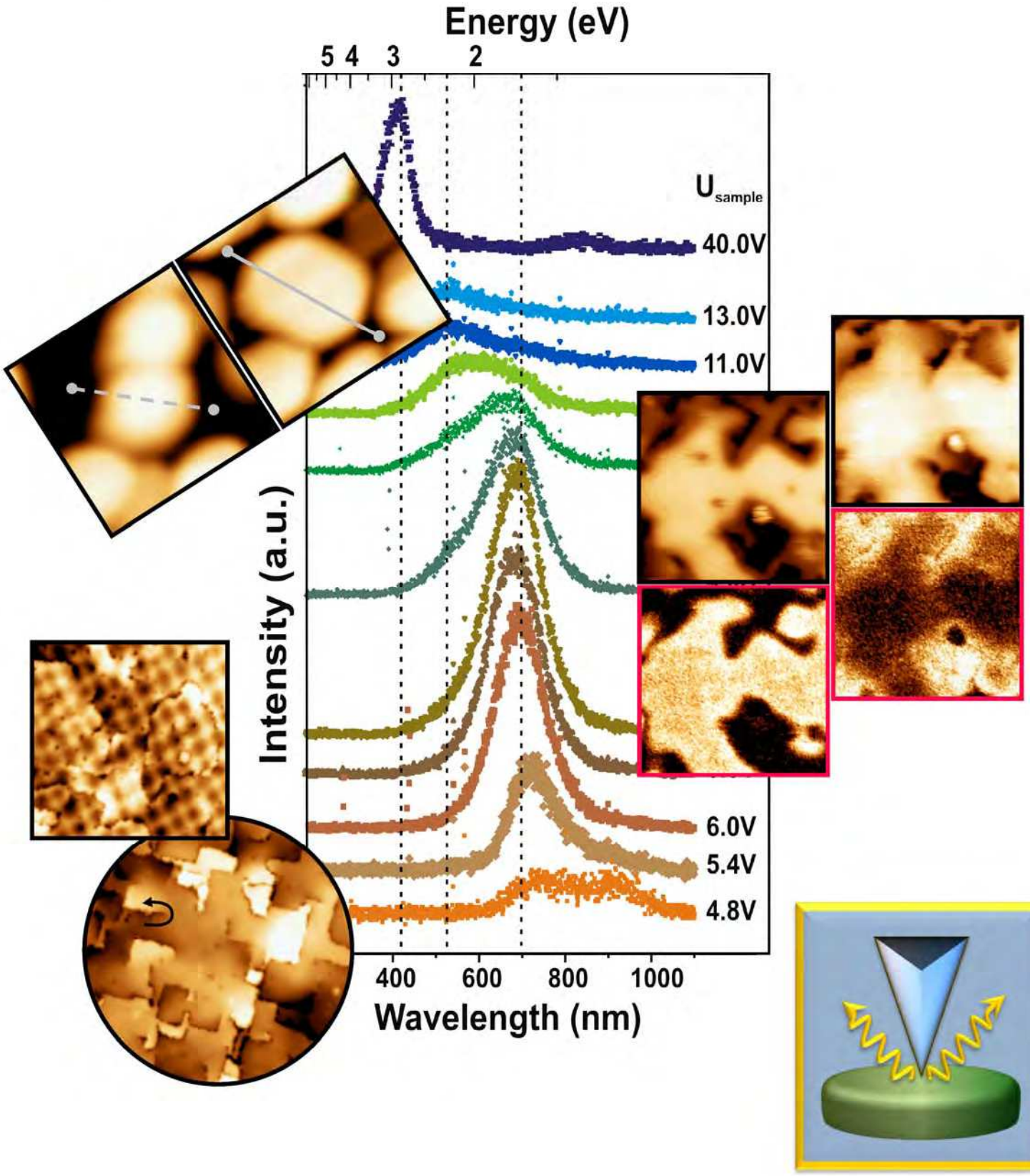

Spatially Resolved Optical Measurements on Supported Metal Particles and Oxide Surfaces with the STM

DISSERTATION

zur Erlangung des akademischen Grades
doctor rerum naturalium
(**Dr. rer. nat.**)
Im Fach Physik

eingereicht an der
Mathematisch–Naturwissenschaftlichen Fakultät I
der Humboldt-Universität zu Berlin

von
Hadj Mohamed Benia
geboren am 07.01.1977 in Setif, Algerien

Präsident der Humboldt-Universität zu Berlin:
Prof. Dr. Christoph Markschies

Dekan der Mathematisch–Naturwissenschaftlichen Fakultät I:
Prof. Dr. Lutz-Helmut Schön

Gutachter:
1. Prof. Dr. Hans-Joachim Freund
2. Prof. Dr. Helmut Winter
3. Prof. Dr. Sergio Valeri

Tag der mündlichen Prüfung: 19 November 2008

Abstract

In this thesis, the correlation between the optical properties and the local morphology of supported silver nanoparticle ensembles and MgO thin films deposited on Mo(001) systems is explored by means of Photon-STM. In the first section, dome and disk shaped Ag nanoparticle ensembles with increasing density on an alumina film on NiAl(110) were analyzed as well as ordered and disordered ensembles of Ag nanocolloids on HOPG. The aspect ratio of the Ag nanoparticles was found to have a significant influence not only on the Mie plasmon resonance of a single particle, but also on the electromagnetic coupling within the nanoparticle ensembles. The Mie resonance in the ensemble of dome shaped Ag nanoparticles shows a strong dependence on the interparticle distance, where it shifts to higher energies with increasing particle density, due to destructive interference effects. In the disk-like Ag ensembles, however, the plasmon energy is independent of particle-particle separation. The long-range lateral ordering of size-selected Ag nanocolloids is found to induce a high dipole-dipole coupling within the ensemble. This is mainly reflected by the enhancement of the spectral intensity of the in-plane Mie mode, due to constructive coupling. However, ensembles with either well-ordered or disordered arrangements reveal no important difference in their optical properties, reflecting the weak influence of the long-range order in the particle ensemble. Thin MgO films with different thicknesses were grown on a Mo(001) surface. The stress resulting from the 5.3% lattice mismatch between the MgO(001) and the Mo(001) lattice parameters is found to control the surface morphology of the MgO film until thicknesses of around 25ML at which flat and defect-poor films are obtained. The relaxation of the stress induces a periodic network in the first 7ML of the MgO film, consisting of alternated flat and tilted mosaics. The presence of screw dislocations, steps oriented along the MgO<100> directions, and tilted planes is observed when the MgO films are approximately 12ML thick. In addition, an increase of the MgO work function around these new surface features is revealed from STM spectroscopy. The photon emission induced by field-emitted electron injection from the STM tip into the MgO films is dominated by two emission bands located at 3.1eV and 4.4eV. To check the origin of these bands, further experiments, namely, nucleation of Au particles and creation of F-centers on the MgO surface, have been performed. The nucleation of Au particles at the low coordinated sites is found to quench the MgO optical signal, while the creation or annihilation of F-centers does not alter the MgO emission bands. The 3.1eV and the 4.4eV bands are therefore assigned to the radiative decay of MgO excitons at corner and kink sites, and step sites, respectively. Besides, spatially resolved optical measurements in the tunneling mode of the STM revealed different light emission mechanisms. These radiative processes are mainly related to tip-induced plasmons that form between the tip and the Mo support and to electron transitions between field-emission-resonance states in the STM tip-MgO film junction. The signal from exciton decays at corners and kinks of the MgO surface is however only observed at excitation conditions where the spatial resolution is already strongly reduced.

Zusammenfassung

In der vorliegenden Arbeit wurde mit Hilfe eines Photon-STM die Korrelation zwischen optischen Eigenschaften und der lokalen Morphologie an zwei unterschiedlichen Systemen untersucht. Hierfür wurden zum einem oxidgetragene Ensemble von Silber-Partikeln präpariert, wobei sowohl die Partikelform (Kuppel- und Scheibenform) als auch die deponierte Partikeldichte variiert werden konnte. Neben der Präparation solcher Partikel auf $Al_{10}O_{13}$/NiAl, konnten sphärische Silber-Kolloide geordnet, als auch ungeordnet auf HOPG aufgebracht und untersucht werden. Dabei zeigte sich, dass das Verhältnis von Höhen zu Breiten nicht nur einen signifikanten Einfluss auf die Mie-Resonanz des einzelnen Partikels hat, sondern auch die elektromagnetische Kopplung der Partikel in einem Ensemble stark kontrolliert. Die energetische Lage der Mie-Resonanz zeigt im Fall der kuppelförmigen Ag-Partikel eine starke Abhängigkeit vom Intepartikel-Abstand, was sich in einer Verschiebung zu höheren Energien für eine steigende Partikeldichte äußert. Eine solche Abhängigkeit konnte bei den Ensembles der scheibenförmigen Partikel nicht beobachtet werden. Des weiteren zeigte sich, dass, verglichen mit den ungeordneten Ensembles, die selbstorganisierte langreichweitige Ordnung der Silber-Kolloide auf HOPG nur einen schwachen Einfluss auf die energetische Position der Mie Resonanz hat.Das zweite hier untersuchte System sind dünne MgO Filme unterschiedlicher Dicken auf einem Mo(001) Substrat. Diese zeigen ein reichhaltiges Wachstumsverhalten, welches durch eine Differenz in den Gitterkonstanten von 5.3% begründet ist und erst ab etwa 25 ML zu einem flachen und defektarmen Film führt. Die so induzierte Spannung relaxiert bis zu einer Dicke von etwa 7 ML in einer periodischen Überstruktur die aus abwechselnd flachen und verkippten Ebenen an der MgO-Mo Grenzschicht hervorgeht.

Für MgO Filme mit einer Dicke von etwa 12 ML werden dann Schraubenversetzungen, ausgedehnte verkippte Ebenen und Stufenkanten mit einer Orientierung entlang der <001> Richtung beobachtet. Die optische Charakterisierung durch Feldemission von Elektronen aus der STM-Spitze in den MgO-Film wird dominiert von zwei Emissionsmaxima bei Energien von 3.1 eV und 4.4 eV. Die kontrollierte Nukleation von Gold Partikeln und die Erzeugung von Farbzentren im MgO Film erlaubten eine Zuordnung dieser Emissionen zu strahlenden Zerfällen von Exitonen an Ecken, Kinken bzw. Stufen des Magnesiumoxids. Solche Emissionsprozesse konnten allerdings nur unter Einstellungen beobachtet werden, bei denen ein gleichzeitiges Rastern der Oberfläche unmöglich ist. Bei moderaten Einstellungen war auch eine ortsaufgelösten Spektroskopie möglich, wobei dann neue Emissionsmechanismen beobachtet wurden. Dabei sind zwei Prozesse wesentlich; zum einen die Ausbildung von sog. Spitzen-induzierten Plasmonen im Bereich zwischen Spitze und dem Mo-Substrat, zum anderen strahlende Elektronenübergänge zwischen sog. Feldemissionsresonanzen, die sich im Spitze/MgO-Film System ausbilden.

Acknowledgements

My first gratitude is for Professor Hans-Joachim Freund. I would like to thank him for giving me the chance and the honor to work under his supervision in his research group, and for making available the means, allowing a good achievement of the work and a comfortable PhD journey. I would like to express my great respect and esteem for his person, for his wisdom, wide knowledge, and kindness.

I am deeply grateful to Professor Helmut Winter for co-supervising my work, for supporting and encouraging me, and for his kindness. I would like also to thank him very much for inviting me at different stages of my PhD work-time and giving me opportunities to present and discuss the results of my work with him and his research-group members.

My next thanks go to the International Max Planck Research School (IMPRS) and all its members. I particularly thank Professor Hans-Joachim Freund, the school speaker, Dr. Thomas Risse, the school coordinator, and the amiable Frau Bettina Menzel, the school secretary, without forgetting Professor Jörg Libuda, the former coordinator. While being a member of the IMPRS, I considerably benefited from the organized block courses, soft skill seminars, and scientific as well as social activities. I appreciate the convivial atmosphere between the school members. In addition, I would like to thank the IMPRS for the financial support during my PhD work and for my German-language courses.

I am profoundly grateful to Dr. Niklas Nilius for his active cooperation and extensive discussions, which were essential to accomplish this study. His valuable comments and suggestions were important for the achievement of my thesis. I wish to thank him for the nice time I spent working with him during my PhD and for his patience and kindness.

I would like to thank particularly: Dr. Stefania Benedetti, for the nice and productive collaboration we made together, and also for her sympathy; Stefan Ulrich, Dr. Xiao Lin, Philipp Myrach, and Jan-Frederik Jerratsch for the multiple and fruitful discussions and suggestions, and especially for their friendliness; Dr. Norbert Ernst, for initiating me in the beginning of my stay in Berlin; The very friendly and kind Alexander Uhl, for his valuable support; All the members of the departments, the administration, the library, and the workshops of the Fritz-Haber-Institute. I especially thank Klaus Peter Vogelgesang, Frau Gabriele Mehnert, Frau Manuela Misch, Frau Elisabeth Stankewitz, and Frau Angela Ziebarth for the precious help and for their infinite kindness.

I am thankful to Dr. Helmut Kuhlenbeck and Dr. Martin Sterrer for the good ideas they gave me when I consulted them, and to Dr. Katrin Domke who provided me gold STM-tips.

My thanks now go to Rouabeh Badis, Dr. Mohamed Torche, Dr. Mohammad Abu Haija, Dr. Imad Belabbas, Prof. Pierre Légaré, Prof. Mohamed Guemmaz, Prof. Jean-Claude Parlebas, and Prof. Aimé Mosser for their encouragements. I also wish to thank Martin Baron and Dr. Dario Stacchiola for their nice friendship.

Dedication

To my parents, who fully supported, encouraged and motivated me with endless love and confidence

To my grandmother EMMA for her love, support, and encouragements

To my grandmother Sassia, may her soul rest in peace!

To my brother Rabeh

To my sisters Mouna & Loubna and their husbands Djamel & Fodhil

To my nephews and niece

To my aunt Djahida, may her soul rest in peace!

To my aunt Farida,

To all my aunts and uncles

Contents

Introduction and Motivation

In the last few years, a great development in the research tools to study optical materials on the nanoscale has been achieved, allowing a more detailed knowledge on their local optical properties. This progress in the optical measurements was possible thanks to the large advances in the laser technology, electronics, and computers on one hand [1], and in the use of new analysis techniques characterized by high spatial resolution, such as, the scanning probe microscopy, on the other hand [2,3,4].

Optical spectroscopy with the STM has evolved into a powerful tool to measure optical properties of a sample surface with nanometer spatial resolution [3]. It allows direct correlation between the optical characteristics and the structural properties of the studied material. This is in contrast to classical optical spectroscopy methods, where the extracted information is averaged over macroscopic areas, and often exhibit broadening effects due to sample inhomogeneity. In terms of spatial resolution and versatility, optical emission spectroscopy with the STM competes only with a few other local optical methods, like the scanning near-field optical microscopy (SNOM) and related methods [4,5]. Consequently, an STM-based approach has been selected to explore the optical properties of individual species, selected from an ensemble of metal particles [6], semiconductor quantum dots [7] or molecules [8,9,10].

Using such an STM approach, the relationship between the surface optical and structural properties of two optically active systems is investigated in this PhD work.

The first system concerns noble metal nanoparticles, which are particularly interesting optical objects [11]. Their optical properties exhibit distinct extinction bands induced by strong plasmon resonances in the visible spectrum [11,12]. The corresponding optical response can be understood in terms of the classical Mie theory [12], using most of the time simple quasi-electrostatic models of the particle polarizability and bulk dielectric functions [12]. This is in contrast to optical spectra of molecules and semiconductor quantum dots, where the interpretation often requires quantum mechanical calculations [13]. Furthermore, the nanoparticles play a crucial role in various applications, such as, in optical filters [14], plasmon wave-guides [15,16], Surface-Enhanced Raman Spectroscopy (SERS) [17], and photochemistry [18,19]. However, there is a strong relationship between the geometry and spatial arrangement of particles and their optical behavior. The plasmon resonance energy can considerably shift due to changes in the shape of a metal particle and its surrounding medium,

and it can also be affected by the particle density and arrangement within an ensemble [12]. Hence, the optimal performance of devices based on particle plasmon excitations can only be ensured when this relationship is fully established. In this thesis, a detailed investigation of the influence of particle shape, density, and lateral arrangement on the optical behavior of ensembles of supported silver nanoparticle is presented (chapter 3).

The second system under investigation is a wide-gap insulator, namely MgO films on Mo(001). Also in this example, the application of local techniques is desirable to explore the optical properties of oxide materials. Metal oxide surfaces have been subject to a growing interest over the last few years, because of their importance in different applications, especially in the field of heterogeneous catalysis [20,21]. The optical response of wide bandgap oxides is strongly related to the presence of imperfections in the crystal lattice, e.g. defects or low coordinated sites [22,23,24] and should exhibit pronounced spatial variations across their surface. Structural defects act as trapping centers for electron-hole pairs (excitons), which then decay via the emission of photons with trap specific energies [25,26]. Thus far, correlation between the various defect types on the surface (vacancies, corner or step sites) and their optical signature is only based on a combination of non-local optical spectroscopy and model calculations, and relies on the comparison of measured and calculated photon energies. To verify this assignment on a purely experimental base, local structural and optical information have to be acquired from the insulator surface, which is in principle feasible using light emission spectroscopy with the STM. Such experiments are now discussed in chapter 4. The investigation reveals a correlation between the surface morphology and optical properties of differently thick MgO films grown on a Mo single crystal at the local scale.

In the first part of this manuscript (chapter 1), a brief overview over the theory and the working principle of the scanning tunneling microscope is presented. In addition, mechanisms that govern light emission from different STM-sample junctions are described. Special care has been taken to update the available knowledge on photon-emission mechanisms in the STM and connect it with the results of this study. The details of the experimental setup, including the different stages of sample preparation and analysis, are given in chapter 2. In addition, the main technical information about the STM head as well as the optical detection system are specified. At the end of the chapter 2, a number of upgrades on the experimental setup made during my PhD period are presented. The experimental results discussed in chapters 3 and 4 are followed by a summary and outlook section.

Chapter 1

Theoretical Considerations

I. Scanning Tunneling Microscopy (STM)

I.1. Introduction

Since the advent of quantum mechanics in the early years of the 20th century, the tunneling effect of a quantum particle through a potential barrier is recognized. The exploitation of this effect led in 1981 to a revolutionary invention, the "*STM*" [2]. Scanning tunneling microscopy is one of the most fascinating scientific techniques for the analysis of solid surfaces as it permits the exploration of the surface in real space and at the atomic scale. The two inventors of the STM, Binnig and Rohrer, have been awarded with the Nobel Prize in physics in 1986 [27].

The large potential of the STM induced an avalanche of new applications and innovative ideas [28,29]. Besides being a tool to image the atomic structure of surfaces, the STM became a device to locally probe other properties, such as, the local density of states (LDOS) by means of Scanning Tunneling Spectroscopy (STS) [28,30,31], optical properties by Photon-emission STM (PSTM) [3,32,33], magnetic properties by Spin-Polarized STM (SP-STM) [29,34,35,36], and vibrational properties of single adsorbed molecules by means of Inelastic Electron Tunneling Spectroscopy (IETS) [37]. Recently, the combination of STM with a Laser source has resulted in a powerful instrument for Raman spectroscopy of single molecules employing Tip-Enhanced Raman Spectroscopy (TERS) [38,39], as well as for optical spectroscopy in the femtosecond timescale [4].

The diversity of functions and the possibility to perform measurements in vacuum, liquid, and ambient environments at various temperatures made the STM a valuable technique in a variety of research fields. STM is widely used for instance to investigate quantum effects on surfaces [40,41,42], to identify active centers in heterogeneous catalysis [43,44,45], to characterize *in situ* the surface of electrodes in electrochemistry [46,47,48], and to study the properties of biological molecules like DNA [49,50,51]. Furthermore, STM is, nowadays, a potent tool for the development of future electronic devices. These promising devices are

based on atomic and molecular electronic switches as STM permits the manipulation of atoms and molecules on different surfaces [52,53].

I.2. Operation principle

The idea of scanning tunneling microscopy is based on the exploitation of the exponential dependence of the transmission coefficient of electrons through a potential barrier (the tunnel current) on the thickness of the barrier. Thereby, a small variation of the barrier thickness results in a dramatic change in the tunnel current. So practically, if an atomically sharp conductive tip is brought near to the surface of a conductive sample, and if the gap distance between the tip and the surface is very small (few Å), electrons can tunnel from (to) the tip to (from) the surface. By applying a bias to the tip-sample junction, the direction of tunneling is chosen according to the sign of the bias. In a simplified description, electrons tunnel between the top atom of the sharp tip and the counter atoms in the surface. The tunneling current is therefore sensitive to the position of the tip and will vary when the tip is on the top of a surface atom or in between two atoms. Thus, by scanning the surface with the tip and measuring the tunneling current, an atomically resolved picture of the sample surface is produced.

The STM is basically composed of the following parts: (1) A sharp conductive tip, (2) scan system that operates in three dimensions, (3) a power supply, (4) a current amplifier, (5) an electronic feedback loop, (6) a computer for data processing, and (7) a damping system to suppress external vibrations. Figure 1.1 presents a schematic setup of an STM.

The scan control works with piezoelectric ceramics so that the tip can move with a precision better than 0.01 Å. While *x* and *y* piezos are responsible for the lateral scan, the *z* piezo is responsible for the tip-sample separation *d* and is under control of the feedback loop.

The microscope can operate in two modes: (1) *Constant current mode*, where the tunneling current *I* is set to a fixed value. The feedback loop guarantees a constant *I* by controlling the *z* piezo and therefore the distance *d*. The control signal of the Z-piezo is recorded and translated into an image of the surface. The image contains topographic and electronic information. (2) *Constant height mode*, where *d* is fixed and *I* variations are recorded.

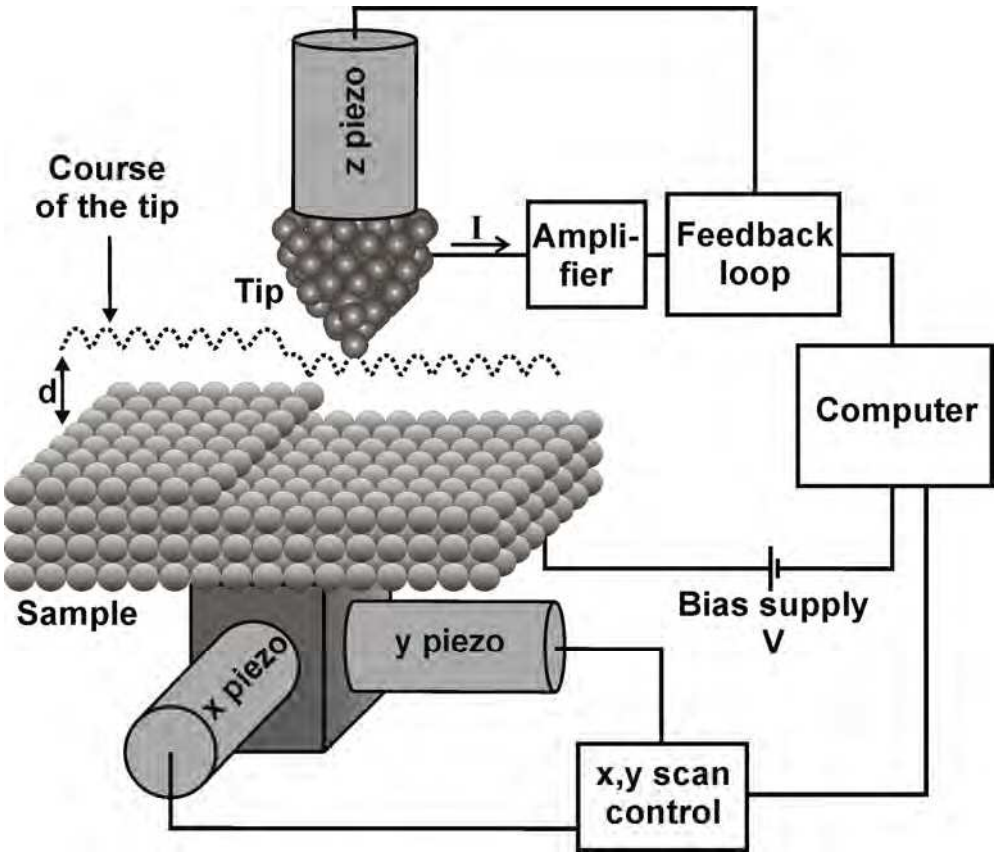

Figure 1.1: *Schematic representation of an STM setup*

I.3. Theoretical approach

With an STM, atomic scale images of different surfaces can be produced. However, the understanding of what is seen on these images and its connection to the real atomic configuration of the probed surfaces is not straightforward and is in many cases rather complicated. The complexity comes from the fact that the contrast as well as the lateral resolution of the images depend on the applied bias, the tip material, and the tip-sample distance. In other words, STM imaging depends on the tip-sample interaction defined by the degree of overlap between electron wave functions and their symmetry on both sides of the tip-sample junction. Therefore, theoretical modeling of the tunneling process in an STM junction is necessary to enable the interpretation of STM images.

Before the invention of the STM, the tunneling phenomenon was already observed in metal-insulator-metal tunneling junctions (MIM) [30]. The most used model to understand MIM junction is *Bardeen's model* [30,54]. Using *Fermi's golden rule*, Bardeen calculated the elastic tunneling current based on the overlap of the wave functions in the two electrodes of a

MIM junction. In case of a tip-sample junction, the tunneling current flowing between the tip and the sample at positive sample bias V is written as [30]:

$$I = \frac{4\pi e}{\hbar} \int_{-\infty}^{+\infty} [f(E_F - eV + E) - f(E_F + E)] \rho_T(E_F - eV + E) \rho_S(E_F + E) |M_{TS}|^2 dE \qquad (1.1)$$

Here $f(E)$ is the Fermi-Dirac distribution, and $\rho_T(E)$ and $\rho_S(E)$ are the local density of states (LDOS) of the tip and the sample, respectively. M is the tunneling matrix element and is defined by the integral over a surface of separation S:

$$M_{TS} = \frac{\hbar}{2m} \int_S (\Psi_T^* \nabla \Psi_S - \Psi_S \nabla \Psi_T^*) dS \qquad (1.2)$$

S is an arbitrary surface anywhere between the tip and the sample and covers the region of significant overlap of the wave functions.

A good evaluation of the M_{TS} matrix needs a good description of tip and sample wave functions. However, the unknown structure of the tip apex makes the modeling of STM images difficult. To circumvent this problem, Tersoff and Hamann modeled the tip apex as a spherical potential well [55,56]. They assumed the resulting eigen wave functions to be only *s*-like wave functions at the center r_0 of the tip apex curvature. The form (1.1) of the tunneling current is then simplified. At low bias, the tunneling current is only proportional to the Fermi-level LDOS of the sample at the center of tip curvature r_0 [30]:

$$I \propto eV . \rho_S(r_0, E_F) \qquad (1.3)$$

Equation (1.3) permits an easy interpretation of STM images by neglecting tip properties and assuming that an STM image is the Fermi-level LDOS representation of the bare surface.

Despite the successful application of the Tersoff and Hamann model in many cases, it failed in predicting the observed high corrugation amplitude in STM images of close packed metal surfaces [30]. Chen [57] attributed this artifact to the restriction to *s*-like tip wave function. He successfully improved the model by assuming localized tip orbitals oriented towards the sample, such as the d_Z^2 orbital of a tungsten tip. Subsequently, depending on the tip material, an appropriate tip orbital is chosen and a suitable model is generated, which then reproduces the experimental resolution.

Besides, based on the WKB (Wentzel–Kramers–Brillouin) semiclassical approximation, an alternative description of the tunneling current is obtained using the tunneling transmission probability *T(E,eV,Z)* between two planar electrodes at temperatures close to 0K and bias voltages lower than the work function of both tip and sample [58]:

$$I \propto \int_{-\infty}^{+\infty} \rho_T(r, E_F - eV + E).\rho_S(r, E_F + E).T(E, eV, Z).dE \tag{1.4}$$

where

$$T(E, eV, Z) = exp\left(-\frac{2Z\sqrt{2m}}{\hbar}\sqrt{\frac{\phi_S + \phi_T}{2} + \frac{eV}{2} - E}\right) \tag{1.5}$$

ϕ_S and ϕ_T are sample and tip work functions, respectively, while Z is the tip–sample distance.

II. Image potential and field emission resonances in the STM junction

II.1. Introduction

Creating a surface in a crystal induces a modification of the electronic structure in its vicinity, due to the interruption of the periodic potential of the solid. Hence, new electronic states appear. These states have no equivalent in the bulk band structure. The corresponding wave functions are peaked at the surface plane and their amplitudes decay when going from the surface towards the bulk and the vacuum. When such a surface state has a continuation into the extended bulk states, the state is a *surface resonance*. When the energy position of the state is in the forbidden region of the projected bulk structure, it is a *bound surface state* [59,60].

In this thesis, such surface states, namely image-type surface states, are observed in STM measurements performed over a wide-gap metal oxide (chapter 4). In the following paragraphs, a brief introduction to image potential states and field-emission resonances is given.

II.2. Image potential states

Image potential states are localized states in the vacuum region near the surface. They belong to the category of bound surface states and are typical for metal surfaces presenting a bandgap around the vacuum level [60]. These states were first predicted by Cole and Cohen [61], then treated in more details by Echnique and Pendry [62], and finally observed experimentally by means of LEED [63] and IPES [64,65]. The nature of image potential states is rather simple: An electron in front of the surface induces a local positive charge in the crystal, i.e., an image charge, figure 1.2.

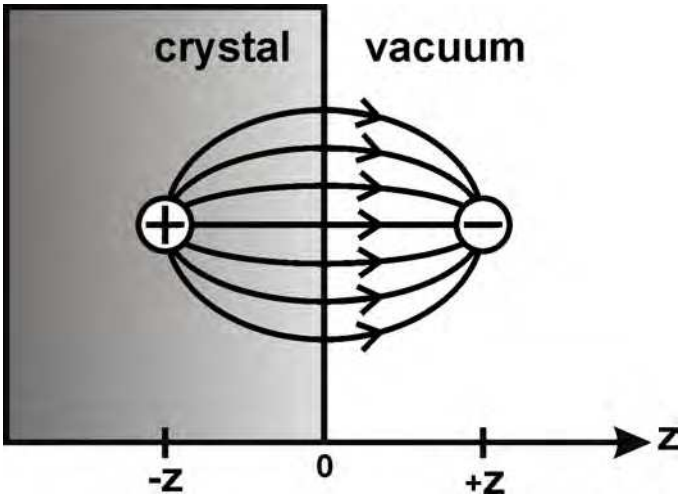

Figure 1.2: *An electron in front of the surface at distance z creates a positive charge (mirror image) at -z with respect to the surface. The Coulomb interaction between the two different charges defines the image dipole potential.*

The situation can be described as a particle in quantum well, where the particle can occupy only discrete energy levels. In the image-potential case, the electron is trapped at approximately one Bohr radius from the surface by his own induced potential [59].

The image potential is described by:

$$U(z) = -\frac{e^2}{4\pi\varepsilon_0}\frac{1}{4|z|} \tag{1.6}$$

where z = 0 marks the image plane (plane of the surface).

As presented in figure 1.3, the potential resembles a central well. The solution of the Schrödinger equation of the system is more complex than for the standard case of a rectangular well. The system is treated in analogy to the hydrogen atom with an orbital quantum number *l=0* [59]. Like the Rydberg states, the energy eigenvalues are given by:

$$E_n = E_{vac} - \frac{0.85\,eV}{(n+a)^2} + \frac{\hbar^2 k_{//}^2}{2m} \tag{1.7}$$

n is the quantum number; *a* is a correction that accounts for the influence of the surface potential. It allows a better description of the resonant levels ($0 \le a \le 0.5$) [59,62,66].

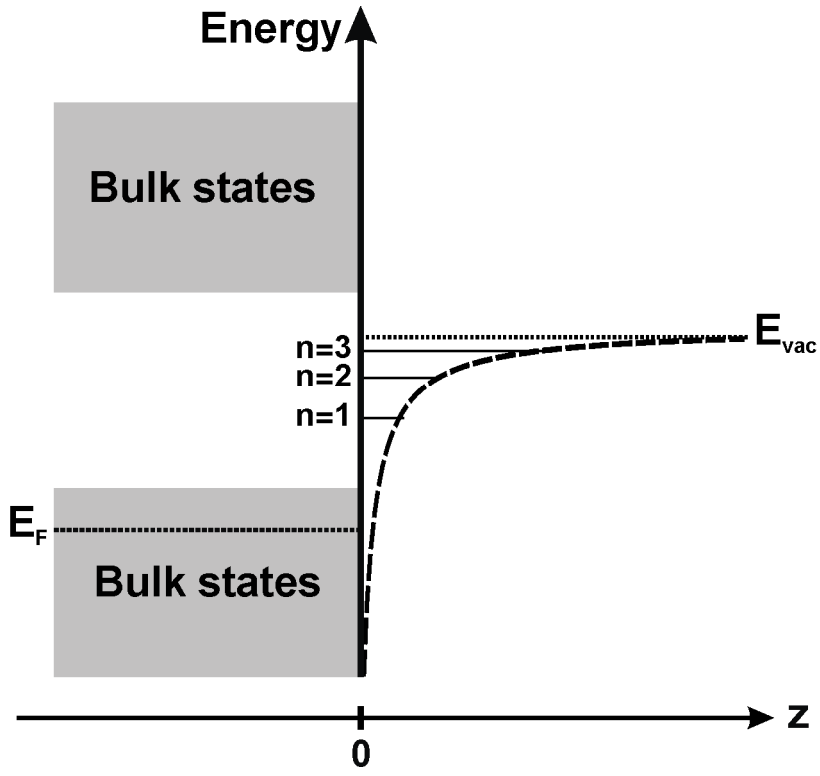

Figure 1.3: *Representation of the image potential form $U(z) \propto -e^2/z$ (dashed line) and the surface electronic structure of a metal crystal having a band gap around E_{vac}. The first three energy levels are also drawn.*

In opposite to box-like quantum wells, here the energy eigenvalues converge asymptotically to the continuum at the vacuum level, i.e., the separation between the quantum levels gets smaller when approaching the E_{vac}, following the $-1/n^2$ term. The last term in equation (1.7) describes the free electron-like behavior of the bound electron in the plan parallel to the surface. In this picture, the bound states are standing electron waves perpendicular to the surface resulting from the interference of waves reflected at the surface potential step on one side and the image potential wall at the other side. In this picture, the bandgap in the metal is needed to ensure a high reflectance at the surface side [59,60].

Typical examples for metal surfaces presenting a bandgap in the surface-projected bulk band structure around E_{vac} are low index surfaces of noble metals, such as the Cu(100), and Cu(111) surfaces [67] (see figure 1.4).

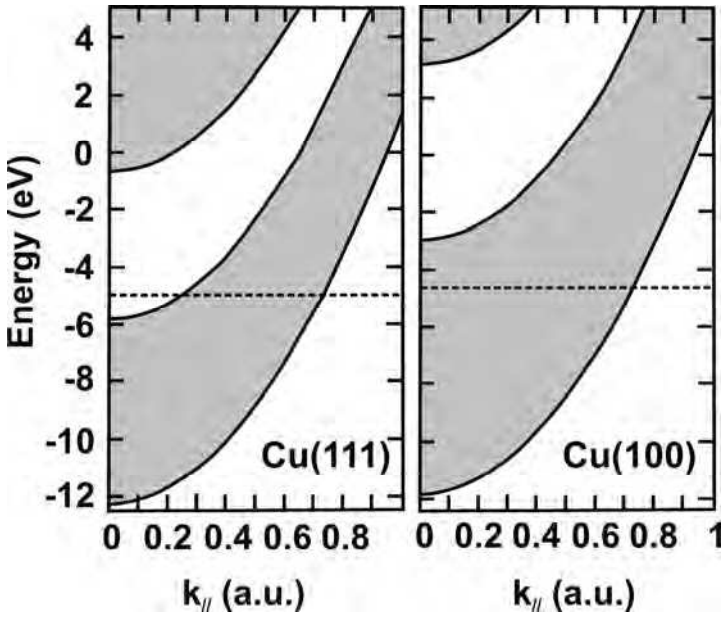

Figure 1.4: *Energy of the electronic states of Cu(111) and Cu(100) surfaces, as a function of the electron momentum parallel to the surface ($k_{//}$). E_{vac} is here the energy reference, E_F is the dashed line. The area in white represents the projected forbidden states [67].*

However, even for metal surfaces where no bandgap exists, the image potential states are observed. The modulation of the crystal potential due to the ion cores is found to induce a sufficient electron reflectivity on the crystal side [68].

Image states exist for semiconductor and insulator surfaces as well [59]. In this case, the static dielectric constant ε is taken into account and the potential (1.6) becomes:

$$U(z) = -\frac{\varepsilon - 1}{\varepsilon + 1} \frac{e^2}{4\pi\varepsilon_0} \frac{1}{4|z|} \tag{1.8}$$

The image potential states are intrinsically empty due to their position above E_F. They are typically probed by IPES [64,65], 2PPE [66,69], or STM [70] techniques. However, with STM, the applied electric field between the tip and the sample induces a Stark shift and the expansion of the states, and therefore, an alteration of the fundamental spectrum of the image potential states [70]. The case of image potential states in STM junctions is treated in the next section.

It should be mentioned that since the image potential states are dependent on the E_{vac}, any perturbation that induces a change in the work function, such as deposition of atoms, molecules or thin atomic layers, results in a shift of the states following the shift of E_{vac}. Therefore, by probing the image states an estimation of work function changes can be deduced.

II.3. Field emission resonances (Gundlach oscillations)

The field emission resonances (FERs) are electronic states, which especially occur in STM geometries where an electric field across the STM junction is applied. They are considered as the result of the shift and expansion of the image potential states due to the presence the electric field. The shifted positions can be therefore theoretically calculated by adding field-related correction terms to formula (1.7) [70,71]. In the following, an alternative approach to the FERs, based on other consideration than image potential states, shall be discussed.

The FERs are variations in the tunneling conductance between two electrodes of a tunneling junction when voltages higher than the work function of the electrodes are applied (figure 1.5). In 1966, K.H. Gundlach made the first prediction of such oscillations by considering a more realistic potential barrier in the tunneling junction and calculating the transmission coefficient and the tunneling current as a function of the applied bias. He connected the conductance variations to the interference of electron waves reflected in the classical part of the junction between the two electrodes [72].

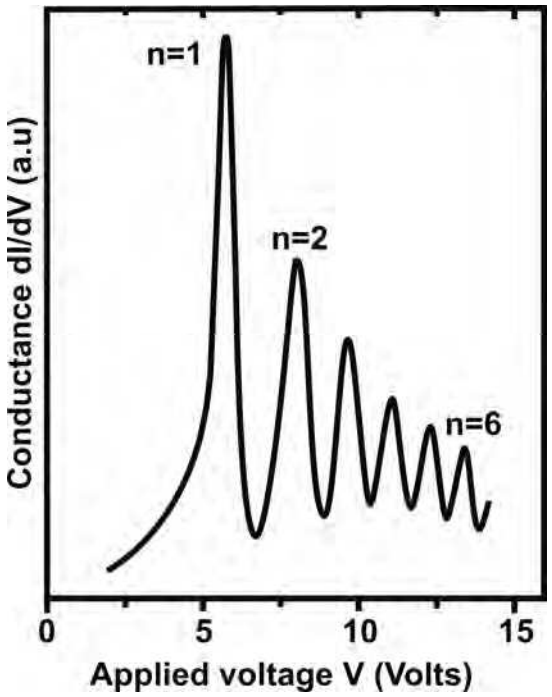

Figure 1.5: *Example of conductance measurements dI/dV within a STM junction as a function of applied voltage [73].*

The phenomenon could be described as follows (figure 1.6): (i) For high biases *V*, electrons with energies *E* bigger than the work function ϕ_t of the electrode (the tip) have a certain probability *D(E,V)* to tunnel to the classical turning point z_0. Once they access the classical part of the barrier (shaded area in figure 1.6), they are accelerated by the applied bias towards the counter electrode (the sample). The regime at which such electron emission is obtained is called the *Fowler-Nordheim Field-Emission* regime, after R.H. Fowler and L. Nordheim who first established a theory describing and calculating the electron field-emission from metal surfaces [74].

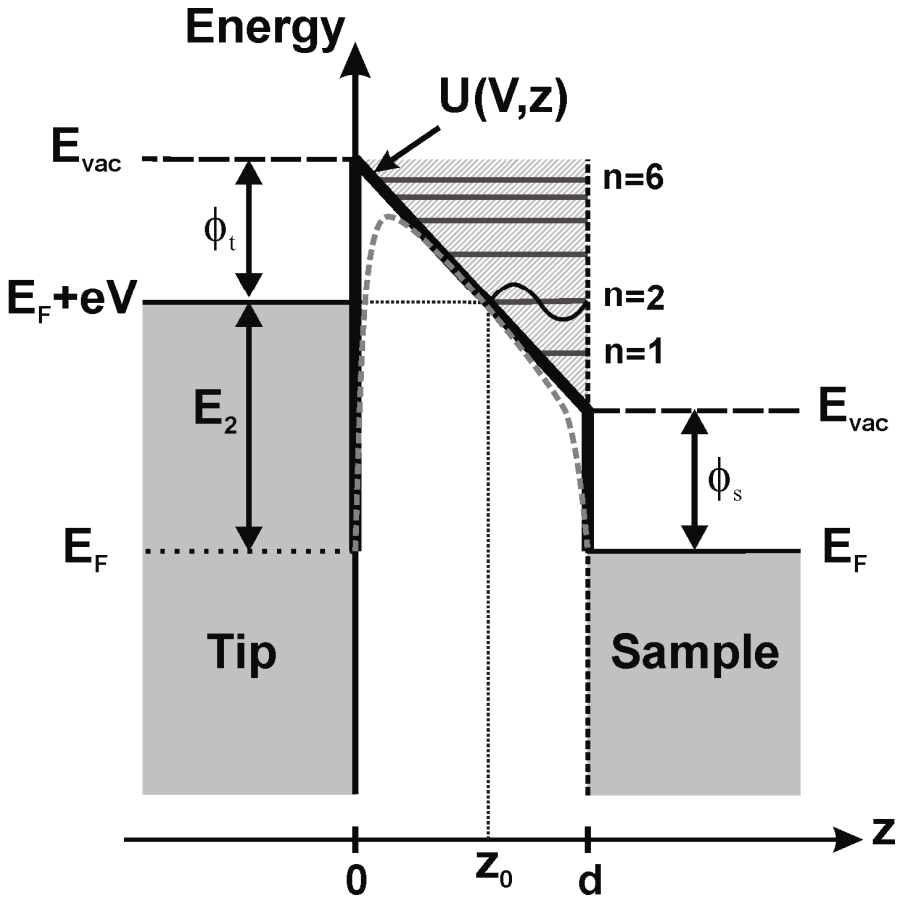

Figure 1.6: *Schematic representation of the formation of Field Emission Resonance states in a STM junction (Sample held at positive bias). The FERs are formed in the classical part of the barrier (Shaded area) between the linearly decreasing part of E_{vac} (dashed line) and the surface potential step at z=d. ϕ_t, ϕ_s are the work functions of the tip and the sample. z_0 is the classical turning point, where the energy of the electron is equal to the potential barrier. n denotes the number of the FERs level. V is the applied bias. E.g.: for $e \cdot V = E_2$, the electron energy is in resonance with the second FER level n=2. The thick dark line delimits the trapezoidal potential barrier. The gray dashed line represents the form of the barrier when the image potential effect is considered.*

The probability *D(E(z),V)* expressing the electron transmission through the potential barrier is written as [72, 75]:

$$D(E,V) \cong \exp\left[-2\left(\frac{2m}{\hbar^2}\right)^{1/2}\int_0^{z_0}(eV-E)^{1/2}\,dz\right] \tag{1.9}$$

If the integration under the exponential term is calculated and under the condition that only electrons near E_F participate in the tunneling, D is written in the Fowler-Nordheim form as [72,75]:

$$D(V) = \frac{4(\phi_t E_F)^{1/2}}{\phi_t + E_F}\exp\left[-\frac{4}{3}\left(\frac{2m}{\hbar^2}\right)^{1/2}\frac{\phi_t^{3/2}}{eF}\right] \tag{1.10}$$

F is the electric field between the electrodes, $F \sim V/d$; d is electrode-electrode distance.

The field-emission current density, also called tunnel current density, is determined at low temperatures (~0K) by the following expression [73]:

$$J(V) = \frac{em}{2\pi^2\hbar^3}\int_0^{E_F}(E_F - E)D(E,U)dE \tag{1.11}$$

After calculating the integral, the well-known *Fowler-Nordheim equation* is obtained [74,75]:

$$J_{FN} = 6.2\times10^6\ \frac{(E_F/\phi_t)^{1/2}}{\phi_t + E_F}\ F^2\exp\left[-\frac{4}{3}\left(\frac{2m}{\hbar^2}\right)^{1/2}\frac{\phi_t^{3/2}}{eF}\right]\ \text{amp/cm}^2 \tag{1.12}$$

(ii) Up to this point, only the electron transmission through the potential barrier, i.e., from $z=0$ to $z=z_0$, was considered and not through the whole junction since the classical part, from $z=z_0$ to $z=d$ (shaded area, figure 1.6), is not taken into account. Gundlach has considered the electron transport behavior inside the second region too. He calculated the total transmission coefficient D through a trapezoidal potential barrier (figure 1.6) after solving the Schrödinger equation for the $z < 0$, $0 < z < d$, and $z > d$ regions.

The resulting total D shows a sinusoidal behavior [72]. The corresponding current density can be written as [73]:

$$J = J_{FN}\sqrt{\frac{E_F + eV}{eV - \phi_s}}\left[1 - \frac{1}{2}\frac{(E_F + \phi_s)\phi_t\sqrt{E_F + eV}}{(eV - \phi_s)^{5/2}}\sin(A+B)\right] \tag{1.13}$$

where $A=\frac{4}{3}\left(\frac{eV-\phi_s}{eFl}\right)^{3/2}$, $\sin B=\frac{2\sqrt{\phi_t\left(eV-\phi_s\right)}}{eV+\phi_t-\phi_s}$, $l^{-3}=\frac{2m}{\hbar^2}eF$

The electrical conductance *dJ/dV* between the two electrodes at voltages higher than their work functions is [73]:

$$\frac{dJ}{dV}=2\frac{\sqrt{2m}}{\hbar}\frac{\phi_t^{3/2}}{eFV}J_{FN}\left(1-\frac{1}{4}\frac{E_F+\phi_s}{\sqrt{\phi_t eV}}\cos\left[\frac{4}{3}\frac{\sqrt{2m}}{\hbar}\frac{\left(eV-\phi_s\right)^{3/2}}{eF}\right]\right) \tag{1.14}$$

Equation (1.14) reflects clearly the oscillations in the conductance (the cosine term). This variation is attributed to electron wave interference between $z=z_0$ and $z=d$. The electrons in the classical part of the junction are partially reflected at the counter electrode ($z=d$), due to the sharp potential change at the surface[1], and at $z=z_0$ by the potential barrier.

So, the electron waves interfere with each other when reflected back and fourth at both sides of the barrier. At certain conditions where the distance d-z_0 (where $z_0 = z_0(V)$) is equal to an integer number times half of the electron wavelength, constructive interferences occur and standing waves are formed. This coincides with high electron transmission, i.e., resonance conditions. The Gundlach oscillations are therefore more commonly called *Field Emission Resonances (FER)*. The FERs could not be predicted using the WKB (Wentzel-Kramers-Brillouin) approximation, which neglects the partial reflectance at the surface when calculating the electron transmission coefficient across the potential barrier [72,76].

The positions of FER levels $E_n=eV_n$ (n = 1, 2, 3…,) are deduced from the condition where the term under the cosine in equation (1.14) is:

$$\frac{4}{3}\frac{\sqrt{2m}}{\hbar}\frac{\left(E_n-\phi_s\right)^{3/2}}{eF}=2\pi\left(n+\frac{1}{2}\right) \tag{1.15}$$

$\Rightarrow$ By supposing $(n + 1/2)^{2/3} \approx n^{2/3}$ one gets the simplified formula:

$$E_n=\phi_s+\left(\frac{\hbar^2}{2m}\right)^{1/3}\left(\frac{3\pi eF}{2}\right)^{2/3}n^{2/3} \tag{1.16}$$

[1] Even though there is no potential barrier at energies higher than the work function of the electrode, an electron in this energy regime has still a finite probability to be reflected when leaving the region of potential barrier or arriving to it, as quantum mechanics predicts. The reflectance decreases exponentially with increasing electron energy.

The substitution of E_n in equation (1.14) for the condition that the cosine terms are equal to -1 gives:

$$\left.\frac{dJ}{dV}\right|_{\max}(n) = 2\frac{\sqrt{2m}}{\hbar} J_{FN} \frac{\phi_t^{3/2}}{F\left(\phi_s + \left(\frac{\hbar^2}{2m}\right)^{1/3}\left(\frac{3\pi eF}{2}\right)^{2/3} n^{2/3}\right)} \times$$
$$\times\left(1+\frac{1}{4}\left(E_F+\phi_s\right)\left(\phi_t\left(\phi_s+\left(\frac{\hbar^2}{2m}\right)^{1/3}\left(\frac{3\pi eF}{2}\right)^{2/3} n^{2/3}\right)\right)^{-1/2}\right) \tag{1.17}$$

Equation (1.17) describes the evolution of maximum amplitudes of the conductance as a function of *n*. A plot of equation (1.17) is presented in figure 1.7. Here, the electric field *F* is supposed to remain constant, as typically assumed for STM measurements in the constant current operation mode.

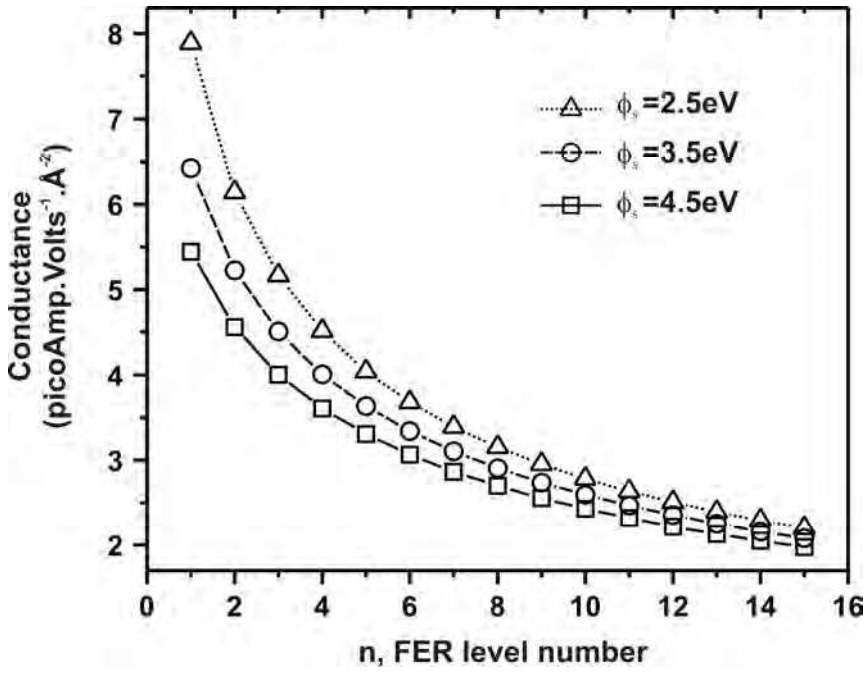

Figure 1.7: *Amplitude of the conductance maximum of an STM junction plotted as a function of the number of the FER level n. The evolution is shown for three different sample work functions. Plot parameters: E_F=5eV, ϕ_t=4.5eV, F=1V/Å.*

From figure 1.7, the fast decrease of the amplitude of the conductance oscillation with increasing voltage is easily recognized (as depicted in figure 1.5).

The drop of the conductance amplitude is related to the exponential decrease of the partial electron reflectance at $z=d$ with increasing energy. Additionally, it signifies that the electrons are not as many times reflected in the higher FER levels and the resulting electron lifetime in these levels is shorter. The electron lifetime can be estimated using Heisenberg uncertainty principle $\Delta t \approx h/\Delta E$, where ΔE is the FWHM of the conductance peak, and h Planck's constant. Δt is typically in the order of femtosecondes (10^{-15} s).

II.4. Image potential effect on FERs

Experimentally measured positions of FER levels in an STM can be fitted using equation (1.16) with a very good agreement for the higher FER levels ($n \geq 2$). Hence, a good estimation of the work function of the sample can be achieved [77]. However, for low FER levels, the experimental data deviate strongly from the theory. The deviation is due to the image potential effect, which is not considered in the above calculation. The presence of the image potential causes a distortion of the trapezoidal potential barrier near the tip and sample surfaces, as shown by the gray dashed line in figure 1.6. This results in an over estimation of the first FER position when using equation (1.16) [73,77].

II.5. Tip shape influence on FERs in STM

When introducing the image dipole effect and the effective tunneling area A, the Fowler-Nordheim field emission current becomes [75,78]:

$$I_{FN} = 6.2\times10^{6} A \frac{\left(E_F/\phi_t\right)^{1/2}}{\alpha^2\left(\phi_t + E_F\right)} F^2 \exp\left[-\frac{4}{3}\left(\frac{2m}{\hbar^2}\right)^{1/2} \frac{\alpha\,\phi_t^{3/2}}{eF}\right] \tag{1.18}$$

where $\alpha = \left(1 - 3.8\times10^{-4}\frac{F^{1/2}}{\phi_t}\right)$ is image effect correction factor.

As it can be seen in equation (1.18), the most important tip-dependant factors are those within the exponential factor, i.e., the field F and tip work function ϕ_t. So, any change in F and/or ϕ_t modifies the form of the trapezoidal potential barrier and therefore causes a shift of the FER positions.

ϕ_t changes can be induced by adsorption of contaminants probably from transfer of sample material onto the tip. The field required to draw the same field emission current is then [78]:

$$F_2 = \left(\frac{\phi_{t2}}{\phi_{t1}} \right)^{3/2} F_1 \tag{1.19}$$

Tip sharpness plays an important role as well. The electric field F at the apex of the tip can be written as a function of applied bias V and tip apex curvature r as [75]:

$$F = \frac{V}{kr} \tag{1.20}$$

k is a geometric factor ($k \approx 5$). From this simplified model it becomes obvious that a presence of a small bump of the tip apex can induce a considerable change of the field, and therefore, of the FER positions.

III. Light emission from a STM

III.1. Introduction

One of the innovative applications of the STM is the ability to analyze optical properties of surfaces [3,32]. The advantage of the STM here resides in the possibility to perform electronic and optical spectroscopies with high lateral resolution, which allows, local investigations of optical properties on the nanometer scale (single atoms and molecules) [79,80]. Indeed, light emission from a STM junction was observed in different experiments. However, it was realized that the emitted light, its spectral distribution, and its intensity depend not only on the properties of the sample, as for classical optical techniques, but also on the material and the shape of the STM tip as well as on the operation conditions of the STM. In the following paragraphs, the different origins of light emission from a tip-sample junction are briefly discussed.

Light emission from an STM junction is mediated by tunneling electrons, which loose a part of their energy within the junction. There are two possible mechanisms for a tunneling electron to cause photon emission: (1) *Inelastic tunneling (IET)*, where the energy of the electron is released in the region between tip and sample, and (2) *hot electron decay (HE)*, where the photon is emitted due to electron recombination just after of the tunneling process, i.e., inside the sample, see figure 1.8 [3].

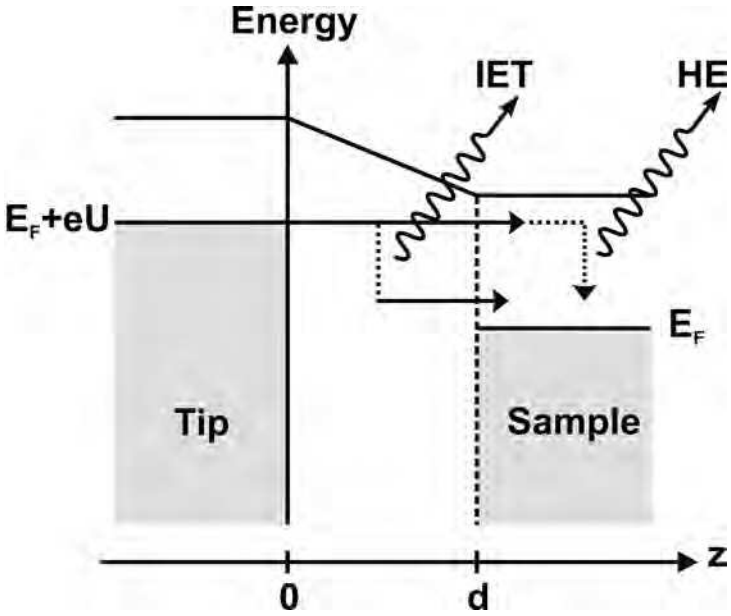

Figure 1.8: *Two possible mechanisms for photon emission from a STM junction. IET: Inelastic tunneling, HE: Hot electron decay [3].*

The probability of IET and HE processes in the STM junction can be determined by the intensity and quantum yield of the emitted radiation (between 10^{-3} and 10^{-5} photon/tunneling electron [3,81]) using theoretical models. The underlying inelastic currents make only a very small contribution to the total tunneling current and are therefore difficult to detect. The photon yield also depends on the degree of coupling between the two mechanisms mentioned above to radiative processes, which are governed by the dielectric properties of the tip and sample materials. Whereas IET is predominant in metal-metal junctions where excitations of the free-electron gas take place, HE decays are found to be responsible for light emission from semiconductor and oxide surfaces as well as from single molecules [3].

III.2. Tip-metal junction

III.2.1. Tip-induced plasmons (TIP)

A basic understanding of the photon emission from STM measurements on a metal surface could be derived from theoretical models developed mainly by Johansson *et al.* [81,82]. In these models, the presence of a metallic tip in close vicinity of a metal surface results in a strong electromagnetic coupling between the free electron gases in the tip and the sample across the STM junction. This coupling influences the tunneling of electrons and gives rise to an inelastic current, which interacts and excites collective-electronic modes (plasmons) in both sides of the cavity. This phenomenon is called *Tip-Induced Plasmon (TIP)*. The plasmon generated in such inelastic tunnel processes can then decay radiatively.

The total radiated power (intensity of photon emission) per unit solid angle Ω and unit photon energy is defined as [81]:

$$\frac{d^2P}{d\Omega d(\hbar\omega)} = 2c\varepsilon_0 \sum_{i,f} r^2 \left|E_{if}(r,\omega)\right|^2 \delta(E_i - E_f - \hbar\omega) \tag{1.21}$$

where

$$E_{if}(\theta, r, \omega) = \frac{i\omega}{4\pi\varepsilon_0 c^2} \int G(\theta, r', \omega) J_{if}(r', \omega)\, d^3r' \tag{1.22}$$

and ε_0 and c are the dielectric function and the light velocity in vacuum, respectively.

Equation (1.22) [81,82] describes the radiated electric field $E_{if}(r,\omega)$ at position r and angle θ of the detector (figure 1.9). It is derived from two contributions: (i) The inelastic

current due to electronic transitions from an initial state $|\, i \,\rangle$ in the tip with energy E_i and wave function ψ_i to a final state in the sample $|\, f \,\rangle$ with energy E_f and wave function ψ_f. (ii) The field enhancement factor $G(\theta,r',\omega)$ which describes the strength of the tip-sample electromagnetic coupling.

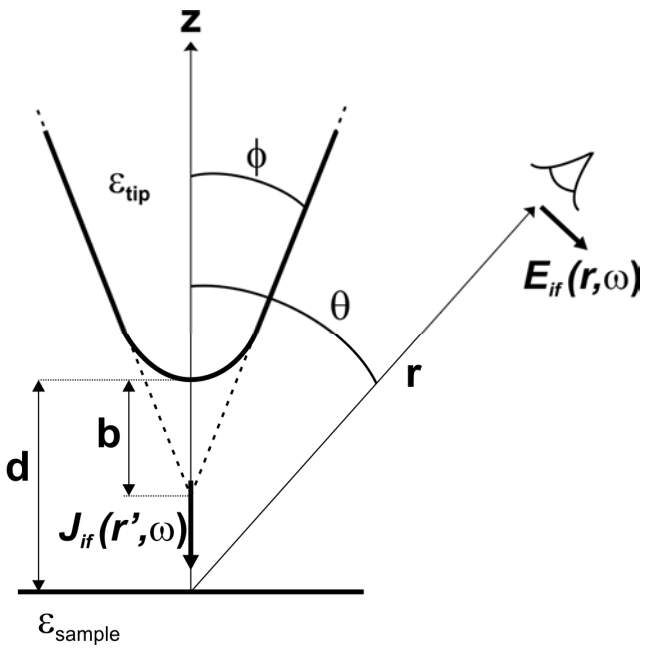

Figure 1.9: *Geometric representation of a STM junction. ε_{tip}, ε_{sample}, are the tip and sample dielectric functions. The shape of the tip here is described by its aperture given by the angle ϕ and the curvature of its apex given by the ratio b/d. J_{if} and E_{if} denote the current density and the radiated electric field at position r and angle θ, respectively [82].*

The tunneling current density $J_{if}(r',\omega)$ is defined by the equation [81]:

$$J_{if}(r',\omega) = -i\frac{e\hbar}{2m}\left(\frac{\partial\psi_f^*}{\partial z'}\psi_i - \psi_f^*\frac{\partial\psi_i}{\partial z'}\right)(r') \tag{1.23}$$

with z' being the point where the inelastic process occurs [82].

The enhancement function $G(\theta,r',\omega)$ depends strongly on the dielectric functions of the tip and the sample and on the geometry of the junction. The energy dependence of G is obtained by solving Laplace's equation for the electrostatic potentials induced at the tip and the sample surfaces using the appropriate boundary conditions [81,82].

Figure 1.10a presents the calculated enhancement factor G for a junction, which consists of an iridium tip and a silver sample for different tip radii. The Ir tip is modeled by a sphere [81]. It is shown that the factor G increases for bigger tip radii. This is attributed to the increase of the polarizability of the cavity. The drop in the enhancement just above 3.5eV reveals the decoupling of the tip and sample electron gases. At this energy, where the real part of the dielectric function of silver is equal to -2, the condition for the plasmon resonance in an Ag sphere is reached in the quasi-static regime (sect. III.2.3) [12]. In other words, the Ir sphere decouples from the Ag sample surface, and the coherent collective electronic excitations in the cavity vanish. This fact demonstrates the predominant influence of the Ag sample on G, since $\varepsilon_1 = -2$ for Ir is reached at around 6eV. In general, the structure of G is dominated by the complex dielectric function ε of the material with smaller imaginary part (lower damping), which is usually the case for the noble metals [3].

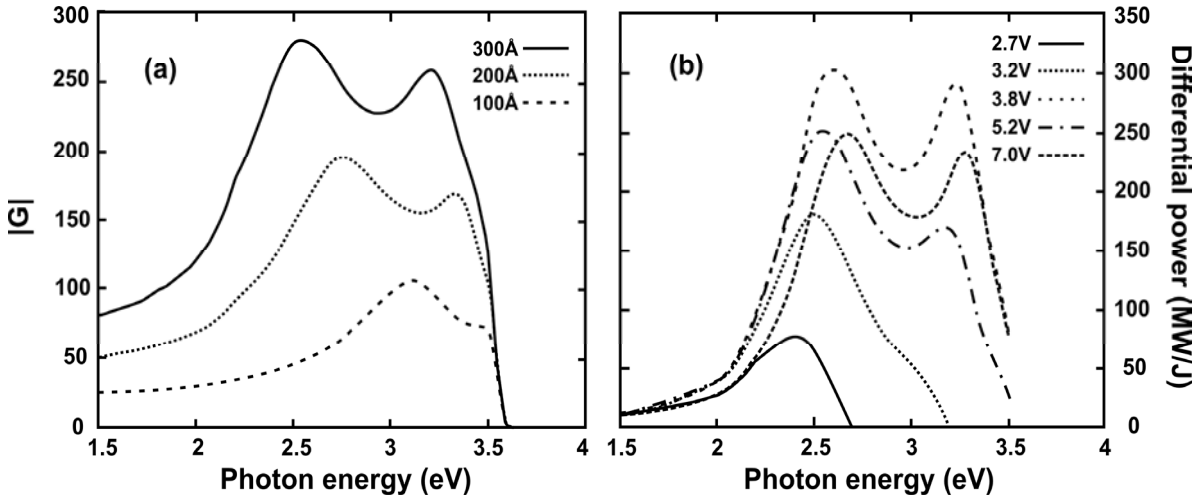

Figure 1.10: *Photon emission characteristics for an Ir tip–Ag sample junction as calculated in [81] where the tip is modeled by a sphere. Emission angle θ is 45°.* ***(a)*** *The absolute value of field enhancement factor G just below the Ir tip for different tip radii.* ***(b)*** *Differential radiated power for various sample bias. Tip radius 300Å, tunneling current I = 300nA.*

From figure 1.10b, which depicts calculated emission spectra for different sample bias U_s, one remarks that the spectral distribution reproduces the behavior of G in this energy range. Note that the maximum energy of emitted photons is limited by the energy of the highest initial state of electrons in the tip above the E_F of the sample, and therefore by eU_s. The emitted light encloses, however, all possible radiative transitions between energy levels in the window range given by $E_i = E_F + eU_s$ and $E_f = E_F$ (equation (1.21)). The fast increase of the light intensity when U_s is between 1.5V and 3.5V (figure 1.10b) is explained by the increasing

number of decay channels involving transitions at around 2.5eV where G has a maximum. For U_s higher than 4V, the intensity decreases again because the tip-sample distance enlarges in order to keep a constant tunneling current. This reduces the electromagnetic coupling across the junction and therefore reduces G, which roughly follows the inverse of tip-sample distance [81].

In conclusion, the photon emission from metal-metal junctions involving TIP is mainly governed by three factors: First, the density of states of tip and sample determining the inelastic tunneling current, second, the dielectric function of tip and sample materials providing the field enhancement, and third, the geometry of the junction where the tip shape is the decisive factor.

From the third point, it becomes apparent that including more details on the tip shape in the calculations leads to a better estimation of the radiation characteristics of an STM cavity. In reference [82], the authors use the boundary charge method, which calculates induced charge density at the interfaces, and describe the tip shape with a hyperbolic geometry (figure 1.9). Hence, more information about the tip influence is accessible. The aperture of the tip is found to control the overall shape of the emission spectrum, while the curvature of the apex affects the intensity. Based on the simulation of the electromagnetic coupling within a tip-metal junction, experimental investigations are well reproduced for different tip and sample material [3,83], and different tip shapes including even multiple tips [84,85]. Also, the local electronic structure related to a distinct sample topography and the different chemical composition of the sample surface is found to be responsible for the emission behavior, as seen in atomically resolved photon emission measurements [3,79,80]. Besides, the large field enhancement associated with TIP is exploited to considerably enhance the Raman signal from supported molecules on metal substrates in Tip-Enhanced Raman Spectroscopy (TERS) experiments [10].

TIPs are also observed when the sample bias exceeds the sample work function [86]. The TIP-induced photon emission in this bias regime is mediated by the field emission resonances (FERs) (sect. II.3) between the tip and sample surface, see figure 1.11.

Finally, it should be mentioned that light emission from flat metal junctions can have other sources than the TIP. A good example are the radiative electron transitions between quantum well states formed in a metal thin film [87].

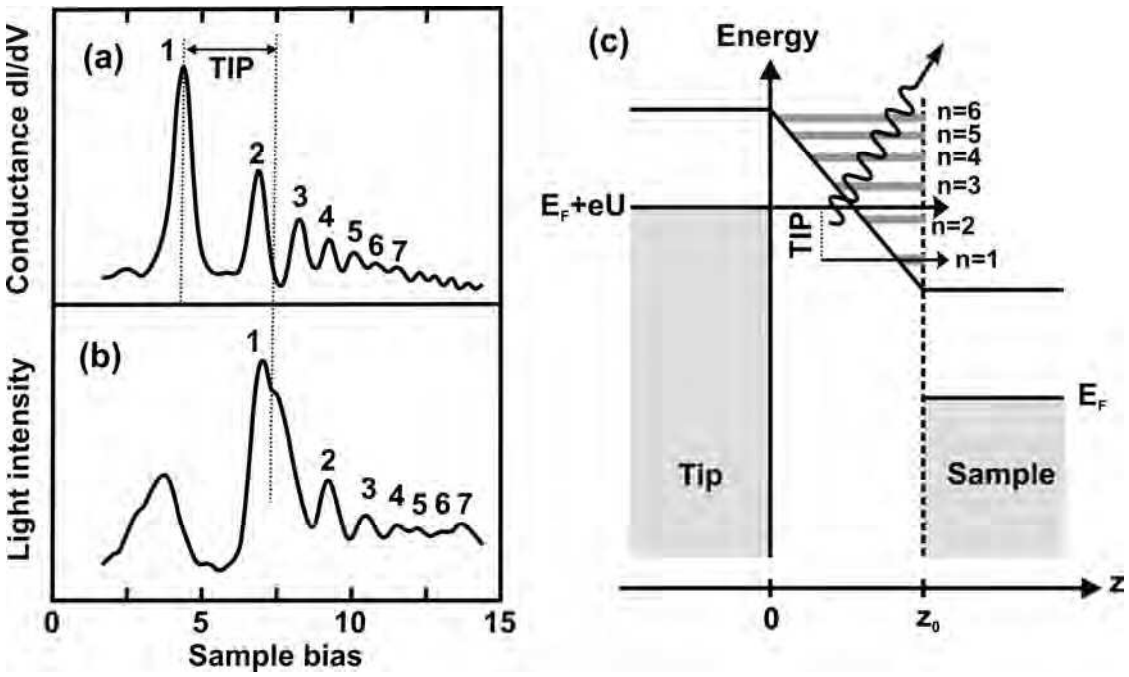

Figure 1.11: (a) *Differential conductance and* ***(b)*** *intensity of photons with 2.1eV energy measured as a function of sample bias for a W-Cu(111) tunnel contact. FERs positions and maxima in photon intensities are offset by ~2.1eV.* ***(c)*** *Energy diagram depicting inelastic tunneling involving TIP radiation mediated by FERs. The final state Ef in the IET process is a FER state [86].*

III.2.2. Tip-metal particle junction

Persson and Baratoff [88] compared possible mechanisms for light emission in the STM by estimating the probabilities of competing radiative and non-radiative processes involving a metal particle in the junction. Two major mechanisms between the tip and the metal particle are taken into account, namely, inelastic tunneling and hot-electron decay. Both mechanisms have certain probabilities to excite either dipolar plasmons or electron-hole pairs. In addition, plasmon has two ways to decay, namely radiative decay and creation of an electron-hole pair. The calculated probabilities for each of theses processes are summarized in figure 1.12. Even though, this model does not describe the spectral and the angular distributions of the emitted light in a realistic manner, and does not consider an eventual electromagnetic coupling between tip and sample, like in the case of TIP, the estimated photon emission yield is in reasonable agreement with experimental photon yield for Ag granular films [3,88]. Whereby, the model considers a large dominance of plasmon decays in the emitted radiations.

Nevertheless, in other works [6,89], the presence of the tip strongly influences the plasmon resonance in the metal particles. This fact is attributed to the increased particle polarizability caused by the coupling with the free-electron gas of the tip in close vicinity.

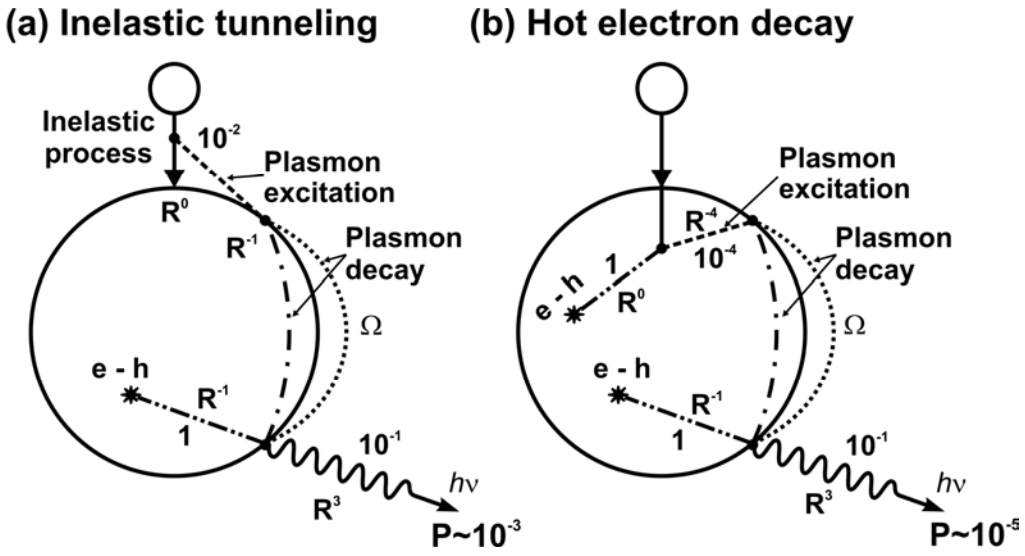

Figure 1.12: *Picture presenting branching probabilities for processes involving excitation of dipolar plasmons and electron-hole pairs via* ***(a)*** *inelastic tunneling or* ***(b)*** *hot electron decay. The probability of radiative decay is indicated by the letter P. The dependence of the various probabilities on the particle radius R is shown in addition. The plasmon frequency is designated by Ω. Radiative and non-radiative decay of the plasmon are schematically represented by dotted and dot-dashed lines, respectively. The relatively high probability of inelastic tunneling process results from the large magnitude of the dipole moment associated with plasmon that facilitates dipolar excitations [88].*

III.2.3. Plasmons in metal particles

Metal nanoparticles exhibit special optical properties compared to the one of the bulk. These properties originate from collective oscillations of conduction electrons inside the particle, the so-called *Mie plasmons* [12]. Depending on the particle size, two regimes of the particle interaction with electromagnetic waves are defined. The *quasi-static regime*, which is of interest in this study, is defined by the condition that the excitation wavelength is much smaller than the particle radius ($\lambda/2 >> R$). In this case, the particle responds to a homogeneous polarization of its volume during excitation. The particle experiences only the time dependence of the field but not the spatial one. The plasmon mode excited at this condition has a dipolar character. In the regime where $\lambda/2 \leq R$, the modulation of the electromagnetic fields occur within the particle. This results in multipolar polarization and retardation effects of the electromagnetic fields and leads to the excitation of higher plasmon modes [12].

The optical response of small metal particles in the quasi-static regime is well described by the Mie Theory [90,12]. It provides an accurate description of the optical extinction spectra of a single sphere of arbitrary material. The theory gives a complete solution of the Maxwell's equations with appropriate boundary conditions, taking into account the size and shape of the particle, its dielectric function $\varepsilon(\omega)$ as well as the one of the embedding medium ε_m.

For the simplest case of a spherical particle with radius R, the polarizability is defined as [12]:

$$\alpha = \alpha_{st} \frac{\varepsilon(\omega) - \varepsilon_m}{\varepsilon(\omega) + 2\varepsilon_m} \tag{1.24}$$

where α_{st} is the classical static polarizability of a metal sphere:

$$\alpha_{cl} = 4\pi\varepsilon_0 R^3 \tag{1.25}$$

The optical extinction cross section ϑ_{ext} for metal particles in the quasi-static regime can be related to their polarizability via [11]:

$$\vartheta_{ext} = k\ \mathrm{Im}\{\alpha\} + \frac{k^4}{6\pi}|\alpha|^2 \tag{1.26}$$

where k is the wave vector ($k = 2\pi/\lambda$), $\mathrm{Im}\{\alpha\}$ and $|\alpha|^2$ denote the imaginary part and the square modulus of α, respectively.

The first term of equation (1.26) is related to light absorption (it describes electron energy losses, such as in EELS measurements, as well [12]). The second term describes losses due to scattering. The dipolar Mie plasmon is associated with the electromagnetic frequency at which the strongest absorption loss is observed, i.e., when $\varepsilon/\varepsilon_m = -2$ [12]. $\varepsilon(\omega)$ is a complex function and primarily only $\varepsilon_{\text{real}}$ is considered for the resonance condition of the Mie plasmon.

The isotropic polarizability of a spherical particle (equation (1.24)) results in a single optical absorption peak, which expresses the three-fold degeneracy of the corresponding Mie mode. However, in certain cases, the particle looses its isotropic behavior and the degeneracy is lifted. A supported spherical particle on a substrate is a good illustration of such a behavior (figure 1.13). The Van der Waals-like coupling between the polarized sphere and its induced image dipoles in the substrate induces an anisotropy of the polarizability. Along the *z* axis, the coupling is different from the one in the (*x*,*y*) plane. While the dipole-dipole interaction parallel to the substrate plane is destructive, it is constructive along the z axis (figure 1.13a). Thus, such a coupling reduces the polarizability of the particle parallel to the substrate plane and increases the perpendicular one. This results in two different Mie plasmon modes where the in-plane mode is two fold degenerate. These two plasmon modes are defined as (1,0) and (1,1) modes according to (*L*,*m*) description, where *L* is the order of multipoles (*L* = 1 for dipole modes). There are *L* +1 eigenmodes distinguished by the value of *m* [12]. The (1,0) and (1,1) are ascribed as vertical and planar modes, respectively. An approximate idea on the inverse relationship between the plasmon resonance ω_p and the particle polarizability can be obtained from the simplified equation (1.27) [12].

$$\omega_p^2 = \frac{Ne^2}{m_e \alpha_{cl}} \tag{1.27}$$

where *N* denotes the total number of conduction electrons in the sphere and m_e is the electron mass.

Thus, according to equation (1.27), the (1,0) and (1,1) modes in a supported particle are red- and blue shifted with respect to the fundamental Mie plasmon of an isolated sphere, respectively (figure 1.13b).

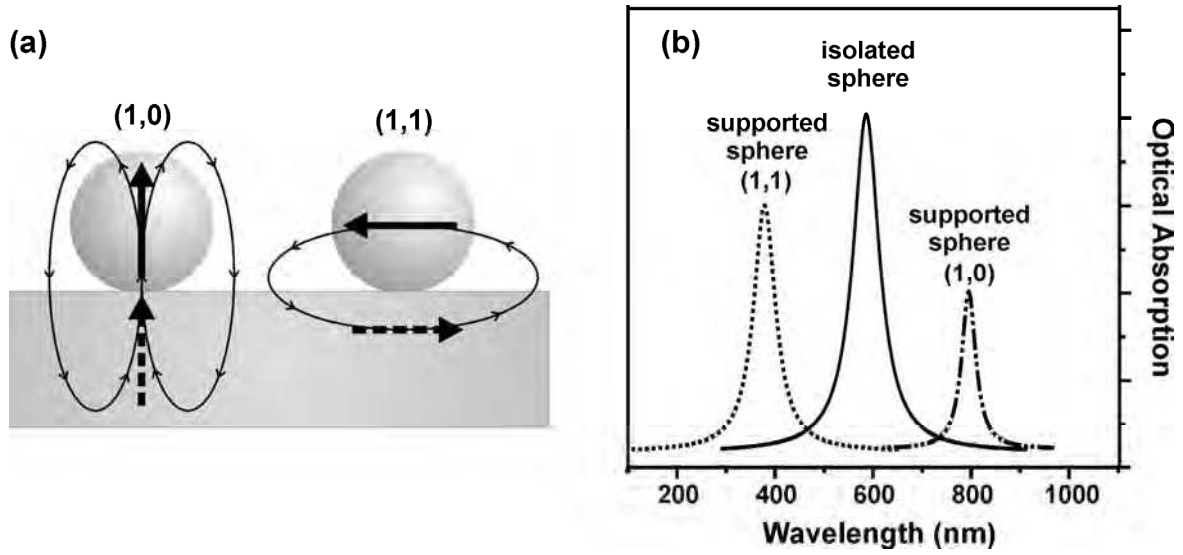

Figure 1.13: (a) *Representation of the interaction between (1,0) and (1,1) dipole modes and their induced image dipoles in the substrate (dotted arrow). Whereas the interaction strengthens the (1,0) mode which increases the polarizability, it weakens the (1,1) mode resulting in smaller polarizability. Field lines for both dipole modes are drawn with weaker lines.* ***(b)*** *Optical absorption cross section plotted for an isolated and a supported spherical particle with arbitrary radius showing the red- and the blue-shift of (1,0) and (1,1) modes due to the presence of substrate. To emphasize the degeneracy of plasmon modes, artificial absorption amplitudes are drawn.*

However, in most cases, the substrate provokes particle-wetting effects, which give rise to complex particle shapes. To estimate the resulting changes in polarizability, the particle is considered to have an ellipsoidal or truncated ellipsoidal shape (oblate/prolate) [91]. The extracted polarizability for an ellipsoidal particle along its principal axes (i= a,b,c) is described by [12]:

$$\alpha_i = \varepsilon_0 \frac{\varepsilon(\omega) - \varepsilon_m}{\varepsilon_m + [\varepsilon(\omega) - \varepsilon_m] L_i} V_{particle} \tag{1.28}$$

V is the particle volume, V=(4π/3)abc. The depolarization factor L_i is determined by the particle shape, where $\sum L_i = 1$. The depolarization factors of a sphere are identical ($L_a = L_b = L_c = 1/3$).

As seen from equation (1.28), the response to an incoming electromagnetic wave is strongly dependent on the angle formed between the polarization vector of the wave and the principal axes i. The aspect ratio[2] (c/a, where $a = b > c$, or $a = b < c$ for an oblate or a prolate

[2] In the literature, the aspect ratio is defined either as c/a or as the reverse quantity a/c.

shape, respectively) characterizes the polarizability of diverse particles with different shapes. This fact is related to the dependence of the depolarization factor along the principal axes on the aspect ratio [92]. For instance, a decrease of the aspect ratio when going from a sphere to an oblate particle leads to the increase of L_c and the decrease of L_a and L_b. Thus, the (1,0) and the (1,1) plasmon modes of such a particle are blue- and red-shifted compared to the mode of a sphere (figure 1.14). This mode shift follows the same direction with a further decrease of the aspect ratio. Note that the mode-shifts induced by the image-dipole coupling with the support and by the aspect ratio decrease are in opposite directions.

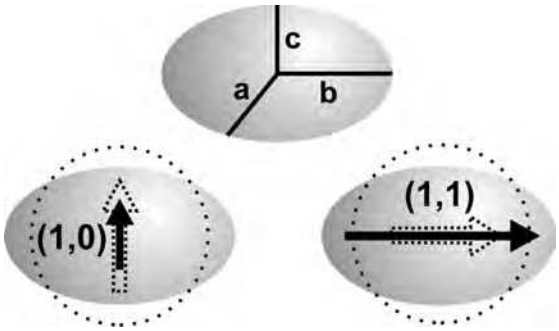

Figure 1.14: *Strength of the (1,0) and (1,1) dipoles in an oblate particle compared to those of a spherical particle with identical volume (dotted lines). The decrease of the aspect ratio c/a induces a variation of the particle polarizability. The polarizability increases along the particle principle axes a and b, and decreases along the c axis. This results in the blue- and the red-shift of the (1,0) and the (1,1) modes, respectively.*

Furthermore, when a spherical particle is present in an ensemble of particles, additional effects on the plasmon positions are observed. These effects originate from the interparticle dipole-dipole interaction, which strongly depends on the interparticle distance. As shown in figure 1.15, coupling along and normal to a chain of particles gives rise to two different polarizabilities. The polarizability increases along the particle-connection line and decreases perpendicular to it. Such a coupling results in two energetically different (1,0) and (1,1) plasmon modes [12].

In general, in order to interpret the observed optical behavior of a particle ensemble all the different interaction mechanisms cited above have to be taken into account in addition to a realistic description of the particle shape. Furthermore, the effects induced by the spatial distribution of particles as well as the properties of the surrounding medium have to be considered. To fulfill this purpose, several models, such as the Maxwell-Garnett model, have been already established enabling rather good interpretation of the optical behavior of the real systems [11,12].

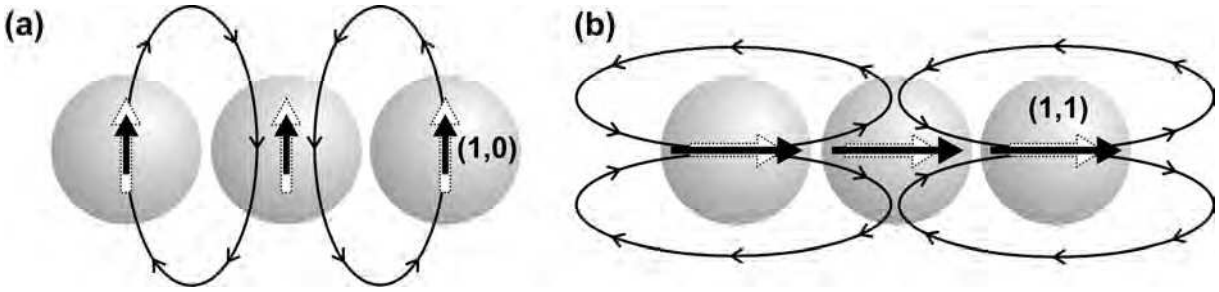

Figure 1.15: *Illustration of the two different dipolar couplings in a chain of particles. While the (1,0) experience destructive coupling* ***(a)****, the interaction along the chain is constructive* ***(b)****. The white dotted arrow represents the dipole strength for the isolated particle. The resulting total polarizabilities lead to a shift of the (1,0) mode to higher energy and of the (1,1) mode to lower energy.*

III.3. Tip–bandgap material junctions

Light emission is also observed for materials without pronounced plasmon modes. STM-induced luminescence from bandgap materials is mainly attributed to intrinsic electronic transitions involving interband and excitonic recombinations in the sample. While in case of tip-induced plasmons the photon emission takes place in the region of the tip-metal junction, the luminescence from tip-semiconductor configuration relates to intrinsic properties of the sample and no dominant influence of the STM tip is revealed [3,93]. The relevant mechanisms for STM-induced luminescence from semiconducting surfaces are schematically summarized in figure 1.16. They can be organized in five categories, which depend primarily on the polarity of the applied bias and its value with respect to the band-edges and the Fermi level position within the bandgap of the sample. In the first category (figure 1.16a), a fraction of tunneling electrons with energies slightly exceeding the conduction band-edge recombine, ones in the sample, with holes in the vicinity of the valence band-edge. The recombination results in light emission with photon energies corresponding to the substrate bandgap [3,94]. In the second category, photons are emitted at tip voltages equal or larger than the threshold energy for electron-hole pair creation. This energy can be estimated using the $3(E_c\text{-}E_v)/2$ rule, which implies that the energy needed to create an electron-hole pair by impact ionization is 1.5 times higher than the size of the bandgap [95]. The mechanism of this category is a two-step process (figure 1.16b). The hot electron injected from the tip creates an electron-hole pair

by impact ionization. The pair relaxes by giving rise to band-edge luminescence before the hole recombines with another electron in the valence band [96]. If the injected electron energy is twice the threshold energy, the probability to get the same luminescence is multiplied by two, i.e., every tip electron can stimulate two electron-hole pairs simultaneously in the sample material [96].

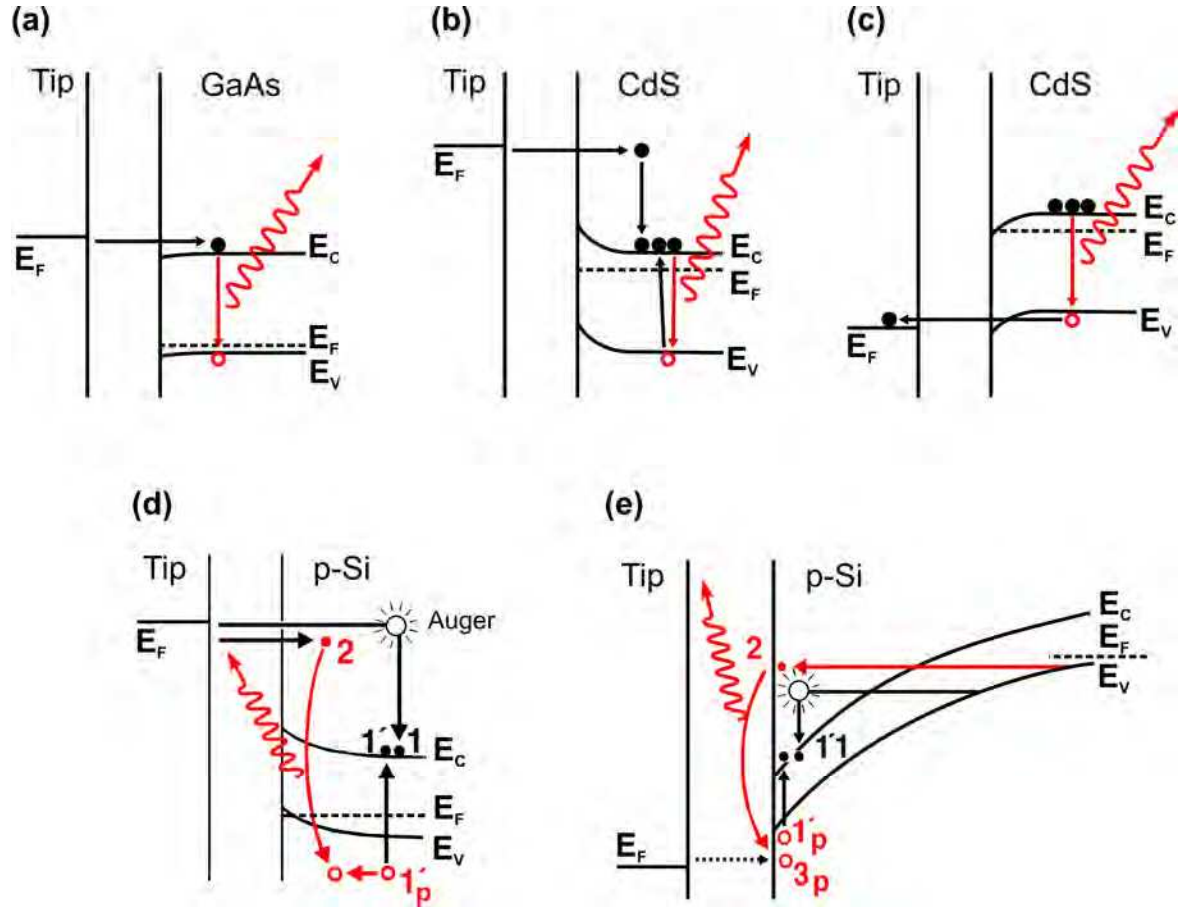

Figure 1.16: *Band diagrams and mechanisms for tunneling-induced luminescence in several band-gap materials.* ***(a) GaAs:*** *A tunneling electron from the tip to the conduction band-edge recombines radiatively with an existing hole at the valence band-edge (near the Fermi level) [94].* ***(b) CdS****: When an injected electron from the tip to the sample carries enough energy, it can create by impact ionization an electron-hole pair across the bandgap, which then relaxes by emitting a photon [96].* ***(c) CdS:*** *At positively biased tip, light can be emitted via the recombination of an electron from the conduction band-edge (near the Fermi level) with the hole left by an electron that has tunneled to the tip [96].* ***(d) p-Si or n-Si****: Hot electrons* **1** *and* **2** *are injected from the tip. Electron* **1** *undergoes an Auger transition creating and electron* **1'** *and a hole* $\mathbf{1'_p}$**.** *Electron* **2** *radiatively recombines with* $\mathbf{1'_p}$ *which may have drifted to the accumulation zone [93].* ***(e) p-Si****: At negatively biased tip, Zener tunneling of electrons* **1** *and* **2** *occurs. Electron* **1** *undergoes an Auger transition creating and electron* **1'** *and a hole* $\mathbf{1'_p}$**.** *Electron* **2** *radiatively recombines with* $\mathbf{1'_p}$ *or with a hot hole* $\mathbf{3_p}$ *tunneled from the tip (dotted arrow) [93]. The figures were adapted from the sited references.*

The light emission in the third category occurs when the tip bias is lower than the valence band-edge of a semiconductor having the Fermi level near the conduction band-edge (figure 1.16c). In other words, the emission process takes place when the absolute value of the tip bias V is approximately equal to $(E_c\text{-}E_v)/e$. Here, holes are created by electron tunneling from the valence band of the sample to the tip. Electrons from the Fermi level can then recombine with the created holes leading to photon emission [96].

The two remaining categories are characterized by the formation of the electron-hole pairs via an Auger-like excitation. The radiative recombination involves more electrons and holes than in the previous categories [93]. Figure 1.16d describes the mechanism where electrons injected from the negatively biased tip have energies high enough to induce Auger ionization processes. The hole resulting from this process recombines radiatively with a second injected electron from the tip. Finally, the mechanism depicted in figure 1.16e concerns only *p*-doped semiconductors. For a positively biased tip, the energy bands of such semiconductors are strongly bend. As a consequence, the Zener effect or tunneling of electrons from the valence band to the conduction band becomes possible. Ones in the conduction band, these electrons gain energy when moving towards the junction. A hole can be created when one of the energetic electrons undergoes an Auger transition. A second Zener electron can then recombine radiatively with the created hole. Besides, light emission can alternatively be generated by the recombination of a Zener-tunneling electron with a hole, which has tunneled from the tip (figure 1.16e) [93]. In the fourth and the fifth categories, figure 1.16d and 1.16e, respectively, the radiative processes involve a set of electron transitions leading to high-energy light emission in the ultraviolet range [93].

In other photon emission processes from semiconducting surfaces, the STM tip is found to be implicated. For example, at certain operation conditions, different than those for luminescence excitations, the decay of localized plasmons excited below the tip is found to be responsible for the detected light from Si(111)-(7×7) reconstructed surface [97]. In other experiments, the emission of linear polarized light from a STM junction made of a tungsten tip and a Si(100) surface is observed. The light is emitted via direct electron transition between tip states and localized states of the sample in an inelastic manner. [98,99].

All the mechanisms described above can, in principle, apply for STM tip–oxide junctions, where particularly electron-hole pairs (excitons) could play an important role for the observed optical activity (see chap. 4, sect. III.3).

Chapter 2

Experimental Setup

I. The UHV system

The UHV system of the Photon-STM consists of two chambers, the preparation chamber and the STM analysis chamber. The two chambers are separated by a gate valve (figure 2.1).

II. The preparation chamber

In the preparation chamber, all tools to manipulate and clean the sample are available. A vacuum of ~$5x10^{-10}$ mbar is ensured by a turbo-molecular pump (pumping speed 150 liter/s). The sample surface can be cleaned by argon-ion sputtering and annealing cycles, and/or by flashing to high temperatures. Since all parts in the high temperature heating stage are made from molybdenum, the sample can be flashed to temperatures as high as 2500K. The heating is realized by electron bombardment: The sample is held at a high bias (from 100 V to 2000 V) and a tungsten filament, heated by a current of ~1.5A to stimulate thermal electron emission is placed near to its backside. The quality of the sample surface in terms of cleanness and long-range order of the crystal structure is checked by means of Low Energy Electron Diffraction (LEED). There are several additional facilities in the preparation chamber to control the sample properties. For film deposition, two electron beam evaporators are available as well as leak valves to introduce reactive gases. Thus, different compound materials with varying stoichiometries can be prepared. The thickness of deposited films is controlled via evaporation rate and exposure time. Sample preparations at temperatures between 100K and 600K can be performed when the sample is located on the copper head of the manipulator. This temperature range is reached either by liquid nitrogen cooling or heating with a tungsten filament. The temperature is measured by a chromel (NiCr alloy)/alumel (NiAl alloy) thermocouple (Type K). For higher temperature preparations, the sample is put in the high temperature heating stage. Temperature measurements in this stage are done with a pyrometer. To allow the preparation and the analysis of different samples without breaking the vacuum, a sample garage able to store at maximum five samples is available.

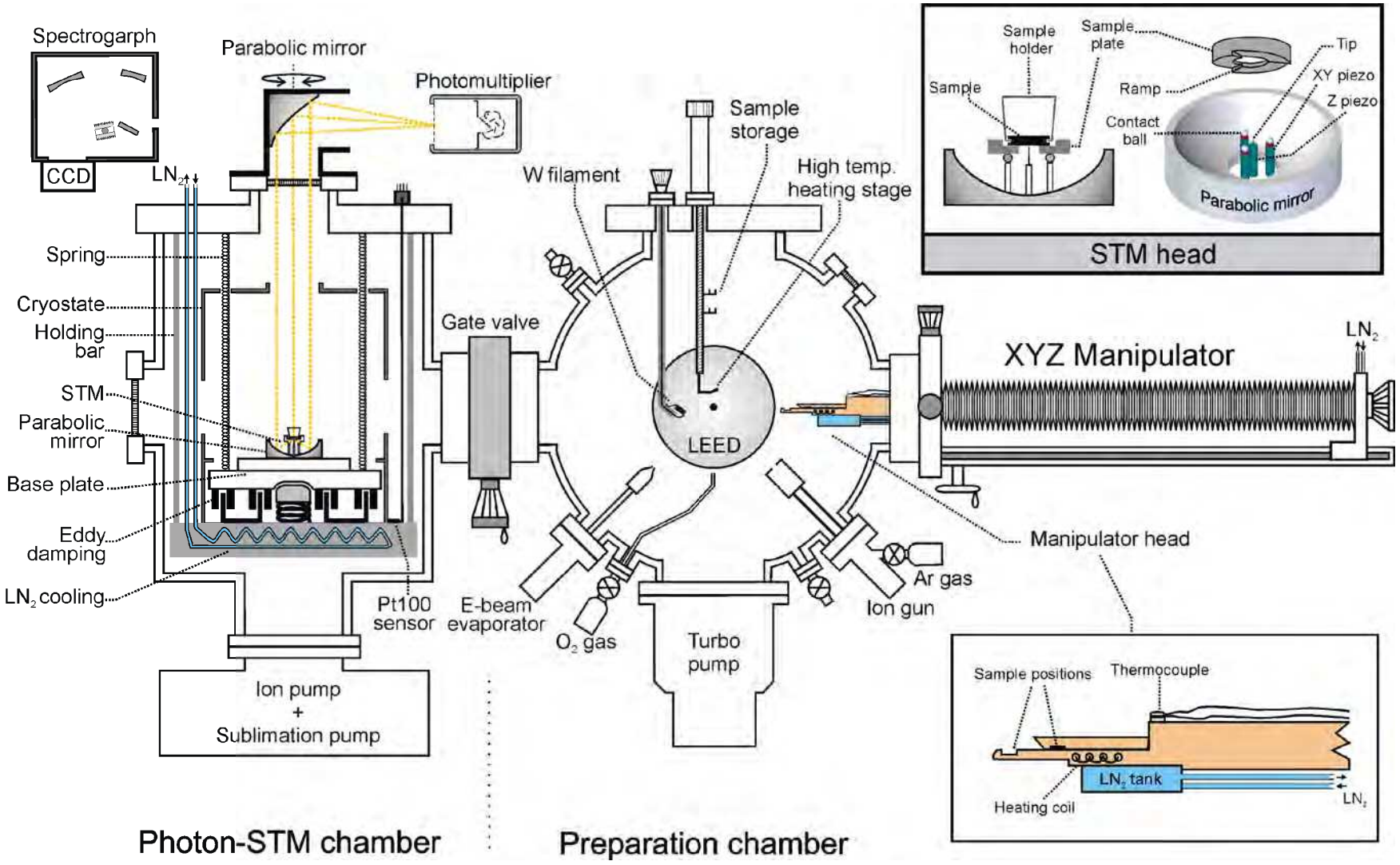

Figure 2.1: *Schematic representation of the experimental setup*

III. The photon-STM chamber

This chamber contains the STM head and the optical detection system.

III.1. The Microscope

The STM head is realized as a Besocke or beetle-type STM [100]. It consists of four piezo-ceramic tubes. Three piezos are responsible to (i) carry the sample and its molybdenum holder, (ii) to approach and withdraw the sample from the STM tip, and (iii) for the lateral XY motion. The fourth piezotube carries the tip. The motion of this piezo is restricted to the Z direction. As depicted in figure 2.1, the Z piezo is placed in the center, and, the three outer piezos form an equilateral triangle around the central one. The tip–sample approach and withdrawal is realized by turning the sample plate via a coordinated motion of the three outer piezos. Three ramps on the lower side of the sample plate transfer the turning into a linear motion and the tip–sample distance decreases or increases depending on the turning direction (figure 2.1). The electric contact to the sample is made through stainless steel balls (radius = 1mm) located at the top side of the outer piezos. To avoid contact with the inner electrode of the piezos, a circular sapphire disk is put between the balls and the piezos. Only one ball is connected through the piezo-tubes to the sample bias output of the STM electronics. The two other balls are disconnected. The isolation of the STM from acoustic and mechanical vibrations is based on (i) a spring suspension coupled with an eddy-current damping system and (ii) a rigid STM head built on a heavy base plate (~1kg). This vibrational isolation system is sufficient to achieve high stability during STM measurements [30]. The reduction of the electronic noise is achieved by a good electric shielding of all STM connections as well as all electronic control devices, and by avoiding electrical ground loops.

The STM head can be cooled down to ~100K via a liquid-nitrogen flow-cryostat, which surrounds the whole microscope. The temperature is measured with a Pt100 sensor. The working pressure in the Photon STM chamber is in average below $2x10^{-10}$mbar.

The STM images are recorded and treated using the WSxM software [101].

III.2. The optical system

The ability to tune the tip-sample distance in this STM setup allows two modes of light excitation in the sample: (1) The tunneling mode, where relatively normal tunneling conditions (voltages up to 10V and currents below 5nA) are used to induce photon emission from local surface regions ($1\times1nm^2$). (2) The field-emission mode, where the tip-sample distance is enlarged to some hundred nanometers and a bias ranging from 25V to 250V is applied to the tip to adjust a current of around 1nA. The field-emitted electrons bombard the sample with high energy inducing a number of phenomena, among them, characteristic radiative excitations of the sample. Depending on the tip-sample distance, the information obtained in this second mode results from a larger excitation area (up to $1\times1\mu m^2$).

To collect the emitted photons from the tip-sample junction, the STM head is surrounded by a parabolic mirror (mirror I), with the tip–sample junction adjusted in the focal point. Mirror I directs the emitted light to a second parabolic mirror (mirror II) outside of the UHV chamber through a quartz window. The light is then focused on either a spectrograph coupled with a liquid-nitrogen-cooled charge-coupled device (CCD), or, on a photomultiplier tube. All emitted photons in a solid angle of ~3sr, delimited by emission angles between 0° and 60° with respect to the sample surface, are collected. Mirror I is made of an $AlMg_3$ compound, which has a very low thermal expansion coefficient, coated with an aluminum film. The optical reflectivity of the Al coating varies from 85% near the UV region to 92% in the visible region [102]. The spectrograph (PI/Acton *SP-2156*) is a grating dispersion device. Two gratings with 150 grooves/mm each and blazed at 300nm and 500nm can be used. The CCD chip (PI/Acton *Spec-10:100*) is characterized by a resolution of 1340x100 pixel, with a pixel size of $20x20\mu m^2$. The sensitivity throughout the optical system covers the wavelength range between 200nm to 1000nm (1.2eV to 6eV). The sensitivity curves of the optical system are shown in figure 2.2. The photomultiplier tube is a side-on type (Hamamatsu *R2949*). It covers the spectral window between 185nm and 900nm with a maximum response at 400nm. Its sensing area is a multialkali photocathode of $8\times6mm^2$ size. The amplification system is based on a circular arrangement of 9 dynodes resulting in a gain of 10^7. The *R2949* is characterized by a low dark current (2nA) and an ultra-fast response (2.2ns).

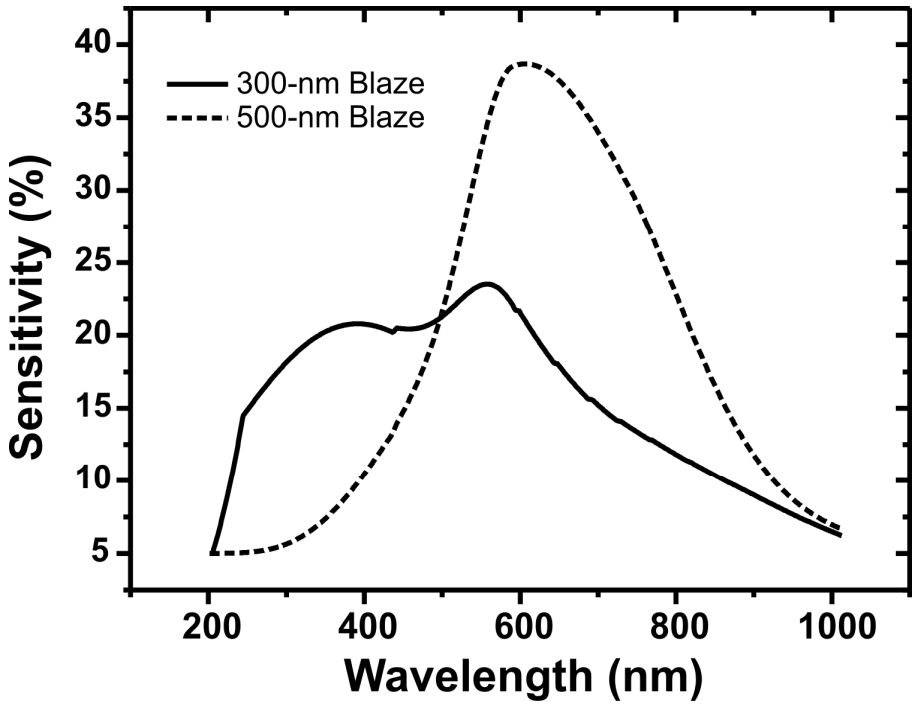

Figure 2.2: *Measured sensitivity curves of the optical system of the photon-STM for the two different gratings in the spectrograph*

IV. Upgrade of the experimental setup

The Photon-STM chamber used for my experiments was built by Dr. Niklas Nilius during his PhD work (2001) [102]. During my PhD (2004-2008), several improvements have been made on the experimental setup, such as:

- Completion of the optical detection system with a photomultiplier, which allows photon detection simultaneously with topographic scanning with high sensitivity (*Photon-mapping*) (see figure 2.3). For this purpose, the sample is scanned with reduced speed (~20nm/s) and enabled feedback loop and the photo-multiplier signal is detected at each pixel of the STM image. To increase the signal to noise ratio, the photon signal is low-pass filtered with a time constant of 10ms before read into the STM controller.

  Furthermore, it is possible to conduct two complementary measurements from the same surface area by just turning the mirror II and switch from the spectrograph to the

photomultiplier. Such combined measurements allow optical spectroscopy and spatial localization of the optical sources on the surface via photon-mapping.

- Operating the liquid-nitrogen cooling system of the STM head in a continuous manner to enable standard STM measurements at ~100K.
- Improvement of the vibrational isolation system of the STM by adding an eddy-current damping system to the previous spring suspension,
- Construction of a high temperature heating stage to prepare samples out of refractory metals,
- Improvement of the protection of the optical system against external shay light,
- Construction of a simple electronic device to control the sample bias and generate voltage pulses to prepare the STM tip in a more controlled way.

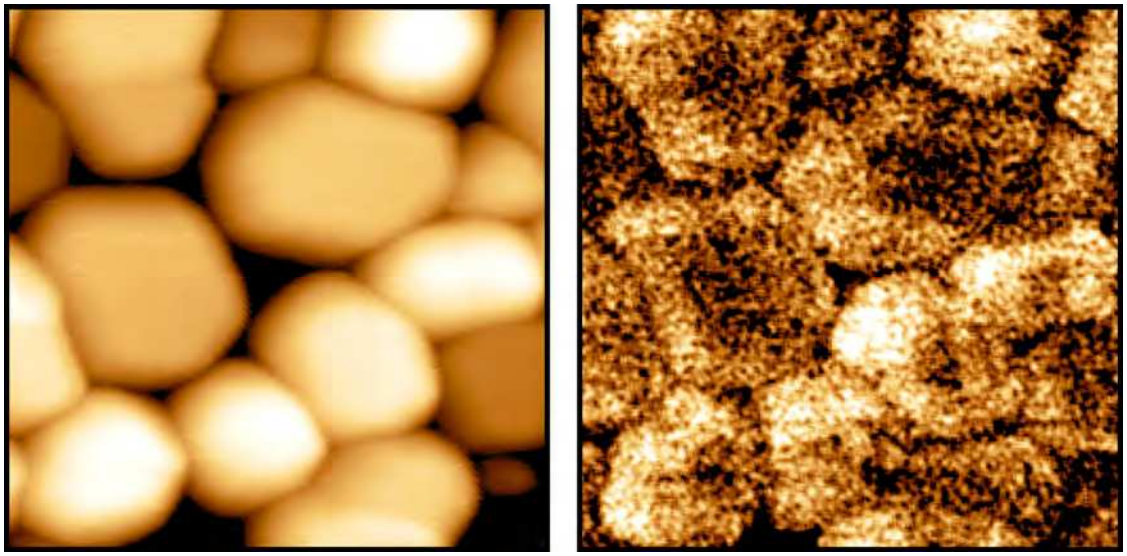

Figure 2.3: *First combined imaging/photon-mapping measurements performed with the photon-STM. On the left side, STM topography image of supported silver particles on a thin alumina film; on the right side, the corresponding photonmap recorded simultaneously. Image size 50×50nm^2.*

Chapter 3

Geometry Effects on Optical Properties of Ag Nanoparticles

I. Introduction

Metal nanoparticles can be prepared by several techniques [11]. The choice of a suitable preparation method is often crucial for the fabrication of ensembles with well-defined properties. In order to accomplish a detailed investigation of the influence of particle shape, density, and lateral arrangement on the optical behavior, supported silver nanoparticle ensembles have been prepared using two different techniques: (i) Vapor deposition of Ag on an alumina film grown on NiAl(110), and (ii) chemical synthesis of Ag nanoparticles followed by a deposition on HOPG. The vapor deposition has the advantage that it enables a good control of the shape, size, and density of the particle ensembles, but the disadvantage that preparation of ensembles with regular particle arrangements and small size distribution is difficult. On the other hand, the rather new concept of making metal particles in a colloidal solution, successfully enabled the formation of a large regular network of particles. In fact, Professor Pileni from the University of Paris has first demonstrated the possibility to self-assemble colloids into ordered 2D and 3D particle structures [103,104]. However, the inter-particle distance is hardly tunable in this approach and requires the recourse to polymer substrates to be controlled [105]. Furthermore, the optical properties are altered by the ligand shells around the particles compared to pure particles prepared by vapor deposition. Nevertheless, a reliable comparison between results from particle ensembles prepared by the two approaches can be made.

Our study on density effects on the optical properties covers Ag particle densities ranging between $0.5\times10^{11}cm^{-2}$ and $11\times10^{11}cm^{-2}$, while keeping the particle shape and size relatively constant. The dependence of the electromagnetic coupling in ensembles with either round or flat particles on the interparticle distance is investigated. Besides, the influence of the long-range order on the optical properties of dense ensembles of spherical Ag particles is explored as well. The combination of scanning tunneling microscopy and photon emission spectroscopy, as possible with the Photon-STM, was particularly suited for simultaneous topographic and optical characterization of the particle ensembles.

II. Shape and density effects

II.1. Particle support: The alumina film

As support material for the bare Ag particle, a well-ordered alumina film has been used. The alumina film is formed by oxidizing the surface of a clean NiAl(110) crystal following the recipe given in [106]: Prior to film growth, the NiAl surface is cleaned by sputtering/annealing cycles, and its quality is checked by means of LEED. The NiAl(110) surface is then exposed to 1200 Langmuir of O_2 at a temperature of 550K, and annealed at 1000K for 5min. This simple procedure results in a well-ordered and atomically flat alumina film with a thickness of ~5Å. Due to the two fold symmetry of the NiAl(110) surface, the film grows in two domains (A and B) rotated by 48° against each other and by ±24° with respect to the $[1\bar{1}0]$ direction of the support. Hence, two kinds of defect lines are observed on the surface of an alumina film: (i) Anti-phase domain boundary (APDB) between identical domains, and (ii) reflection domain boundaries (RDB), which separates domains with different orientation, as shown in figure 3.1. The exact stoichiometry of the alumina film is not Al_2O_3 but rather $Al_{10}O_{13}$ [107].

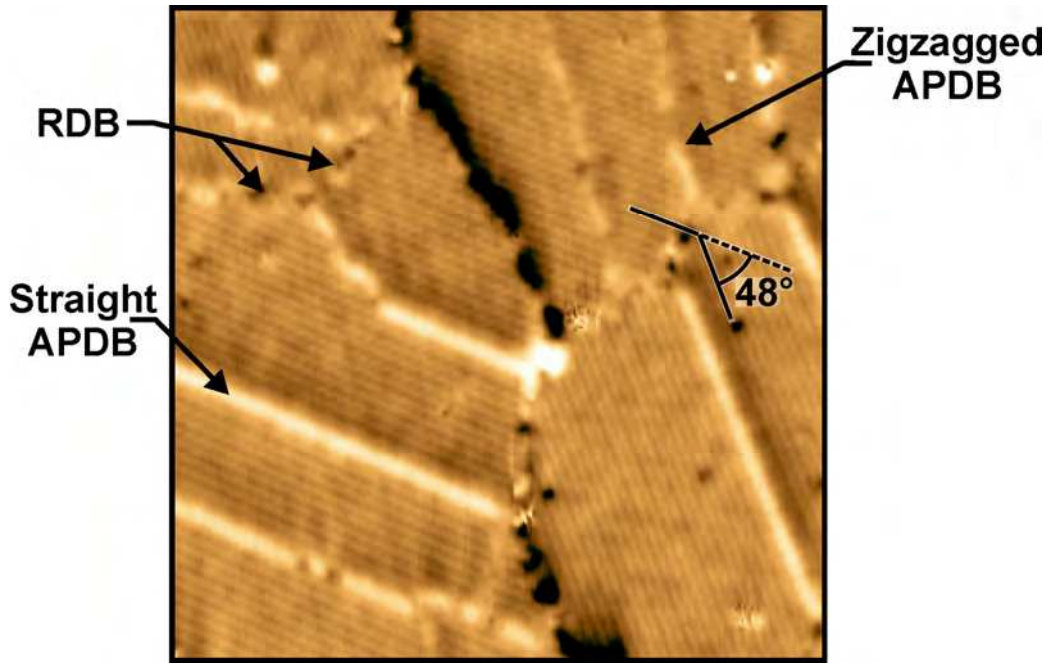

Figure 3.1: *80×80nm² STM topographic image of an alumina film grown on a NiAl(110) surface [108]. On the image, two domains tilted by 48° against each other can be distinguished from the direction of the characteristic line structure. The arrows indicate reflection domain boundaries (RDB) and anti-phase domain boundaries (APDB).*

The anti-phase domain boundaries have a well ordered atomic structure, resulting from the insertion of a row of O and Al atoms in the topmost layer between two neighboring unit cells of the alumina film. The row is inserted either along the short principal vector or along the diagonal of the alumina unit cell. This causes the formation of straight or zigzagged boundaries, respectively [109]. The APDB appear bright in the STM topographic images (figure 3.1) at positive sample bias. This bright appearance of the APDB is caused by the existence of defect-induced energy states in the bandgap, which originate from a deviation of the film stoichiometry along these defect lines [110].

II.2. Ag particle deposition on the alumina film

II.2.1. Experimental aspect

The Ag particles were deposited on the alumina film by thermal sublimation of pure silver (99.95%) using an electron beam evaporator available in the preparation chamber (chap. 2, sect. II). During the evaporation process of silver, only neutral Ag atoms are created since its sublimation energy (~280 kJ/mol) is much lower than the ionization energy (~731 kJ/mol). However, in order to monitor the outgoing atomic flux, a fraction of Ag^+ ions is artificially created inside the evaporator by intersecting the Ag flux with energetic electrons. Based on our own measurements, the atomic flux arriving at the sample surface contains ~99.5% neutral Ag atoms plus ~0.5% of Ag^+ ions. The Ag coverage was calibrated by dosing Ag on clean NiAl(110), where it grows in a layer-by-layer fashion and the amount of deposited Ag can be directly estimated from STM images.

A typical STM topographic image after Ag deposition is shown in figure 3.2. As reported previously [6], Ag particles are inhomogeneously distributed on the alumina surface and mainly nucleate at defect lines leaving the rest of the surface almost uncovered. This results in a high local particle density and the formation of particle chains decorating the defect lines.

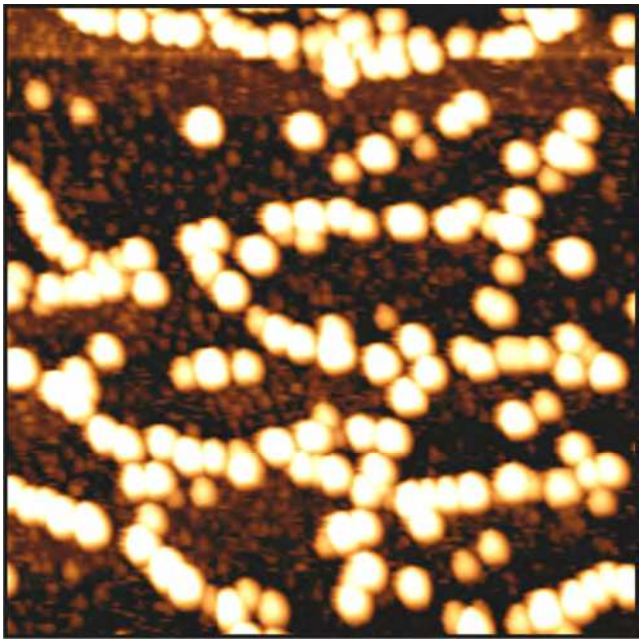

Figure 3.2: *200×200nm^2 STM topographic image of Ag particles supported on $Al_{10}O_{13}$/NiAl(110). The typical defect lines present in the alumina film act as nucleation sites for Ag particles (inhomogeneous nucleation).*

II.2.2. Control of particle shape

The shape of a supported metal nanoparticle on an oxide surface depends on the thermodynamic growth mode of the metal on this particular surface. The different growth modes are governed by the surface free energies of the oxide support γ_o, the metal γ_m, and the metal-support interface γ_i, and can be differentiated into the Volmer-Weber mode (3D aggregates) and the Frank van-der Merwe mode (2D, layer by layer growth). Whereas the metal grows into 3D aggregates for $\gamma_i + \gamma_m > \gamma_o$, 2D growth occurs if $\gamma_i + \gamma_m \leq \gamma_o$ [43,111]. Silver growth on the alumina follows the 3D growth mode, as its surface free energy is higher than the one of the oxide, and as its adhesion to the alumina surface is low [112]. Using the Young-Dupré equation

$$E_{adh} = \gamma_m (1 + \cos\theta) \tag{3.1}$$

which connects the adhesion energy E_{adh} of the metal to the support to γ_m [43,111], an evaluation of the contact angle θ of an Ag particle on Al_2O_3 can be made (figure 3.3). With

E_{adh} of Ag/Al_2O_3 equal to 323×10^{-3} J/m^2 and γ_{Ag} between 814×10^{-3} J/m^2 and 926×10^{-3} J/m^2 [112], the calculated θ has a value of ~127°, which is compatible with the formation of rather dome-like aggregates with a large height to diameter ratio. The prediction is verified by the experimental results, for instance, by topographic STM images [6]. The value of $\gamma_{Alumina}$ is in the range $650\text{-}925\times10^{-3}$ J/m^2 [112], and therefore usually lower than those of metal surfaces.

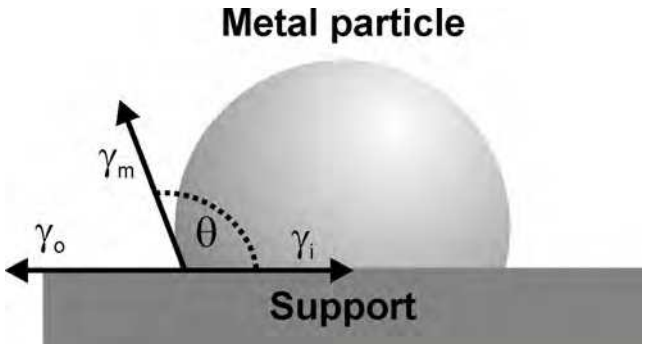

Figure 3.3: *Schematic representation of a metal particle on a flat surface. γ_o , γ_m , and γ_i represent surface free energies of the support, the metal, and the metal-support interface, respectively. θ is the contact angle.*

Apart from dome-shaped Ag particles, Ag particles with a disk-like shape are prepared under defined deposition parameters. In this experiment, the shape of deposited Ag particles is controlled via the sample potential (V_s) with respect to the potential of the Ag crucible in the evaporator (V_c). It was found that when V_s is equal to V_c, dome-like particles are formed, whereas at a negative V_s potential with respect to V_c the formation of disk-like particles is observed. Figures 3.4a and 3.4b show a dome-like and a disk-like Ag particles deposited on $Al_{10}O_{13}$/NiAl(110), respectively. Here, the two types of particle shape were prepared following the same deposition procedure except for the V_s. For the dome-like preparation V_{sc} was set to 0V ($V_{sc} = V_s - V_c$), and for the disk-like ones V_{sc} was -800V. The height profiles of the two particles presented in figure 3.4c clearly demonstrate the shape difference.

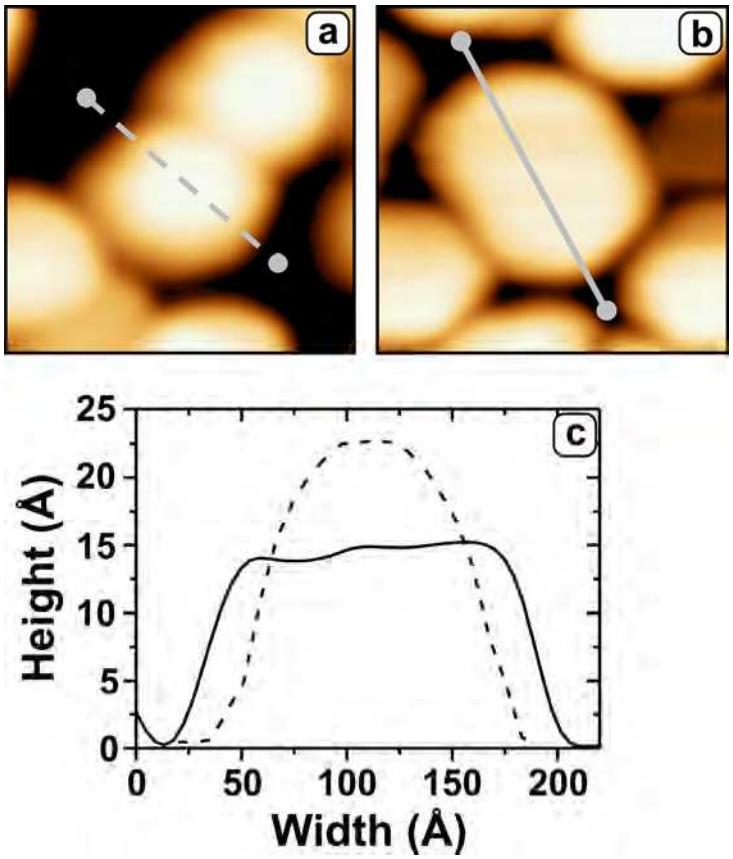

Figure 3.4: *25×25nm^2 STM topographic images of* ***(a)*** *a dome-like and* ***(b)*** *a disk-like Ag particles on alumina film on NiAl(110).* ***(c)*** *Corresponding height profiles of both particles. The measured widths are not corrected for tip convolution effect.*

The dependence of particle shape on the bias difference V_s is rationalized as follows: At V_{sc} = 0V, the Ag^+ ions land on the alumina surface only with their thermal energy, as the neutral Ag atoms, and have no obvious effect on the growth of the Ag particles. At V_{sc} = -800V, the positive ions are accelerated towards the support and hit the sample with high energy. The impact of ions has two effects which lead to the formation of disk-like particles: (1) Local destruction of the alumina surface structure inducing new nucleation sites with a larger Ag–$Al_{10}O_{13}$ adhesion energy [113]; (2) creation of holes and structural damage in the already existing particles. During the restructuring process of the Ag deposit, the holes are filled with material from higher-lying particle regions causing a flattening of the particle.

II.2.3. Control of particle density

The second issue in this experiment is to vary the particle density while keep the particle size and shape constant. For this purpose, we controlled the particle density by tuning the Ag deposition temperature, modifying the density of nucleation sites, and in the support adjusting the evaporation flux of Ag. While samples with low particle densities are prepared at temperatures of up to 500K, the ones with high densities are obtained by cooling the sample to temperatures below 200K. Additionally, new nucleation sites were created via bombardment of the oxide surface with energetic Ar^+ ions (500eV) prior deposition. Suitable combinations of the different deposition parameters allowed a density variation in steps of around $1.0\times10^{11}cm^{-2}$.

Figure 3.5 shows a set of STM topographic images of Ag particle ensembles supported on an $Al_{10}O_{13}$/NiAl(110) film depicting samples with different particle densities. Whereas particles in figures 3.5a to 3.5f have dome-like shapes, those in figures 3.5g to 3.5i are rather disk-like. The particle density varies between $1.0\times10^{11}cm^{-2}$ and $8.0\times10^{11}cm^{-2}$ in the preparations (a) to (f), and between $3.5\times10^{11}cm^{-2}$ and $10.0\times10^{11}cm^{-2}$ in (g) to (i). Due to the presence of additional nucleation sites by Ag^+ ions during the preparation of disk-like particles, densities lower than $3.0\times10^{11}cm^{-2}$ could not be achieved.

From the STM topographic images taken for the different preparations, we made number of observations concerning arrangement, shape, and density of the particles. First of all, no ordered arrangement of particles is found on the surface. Disk-like particles exhibit large [111] top facets, which is the one with the lowest surface energy for Ag (fcc crystal) and the crystallographic plane is deduced from the hexagonal Wulff shape of particles (see figure 3.5g) [43,111,113,114].

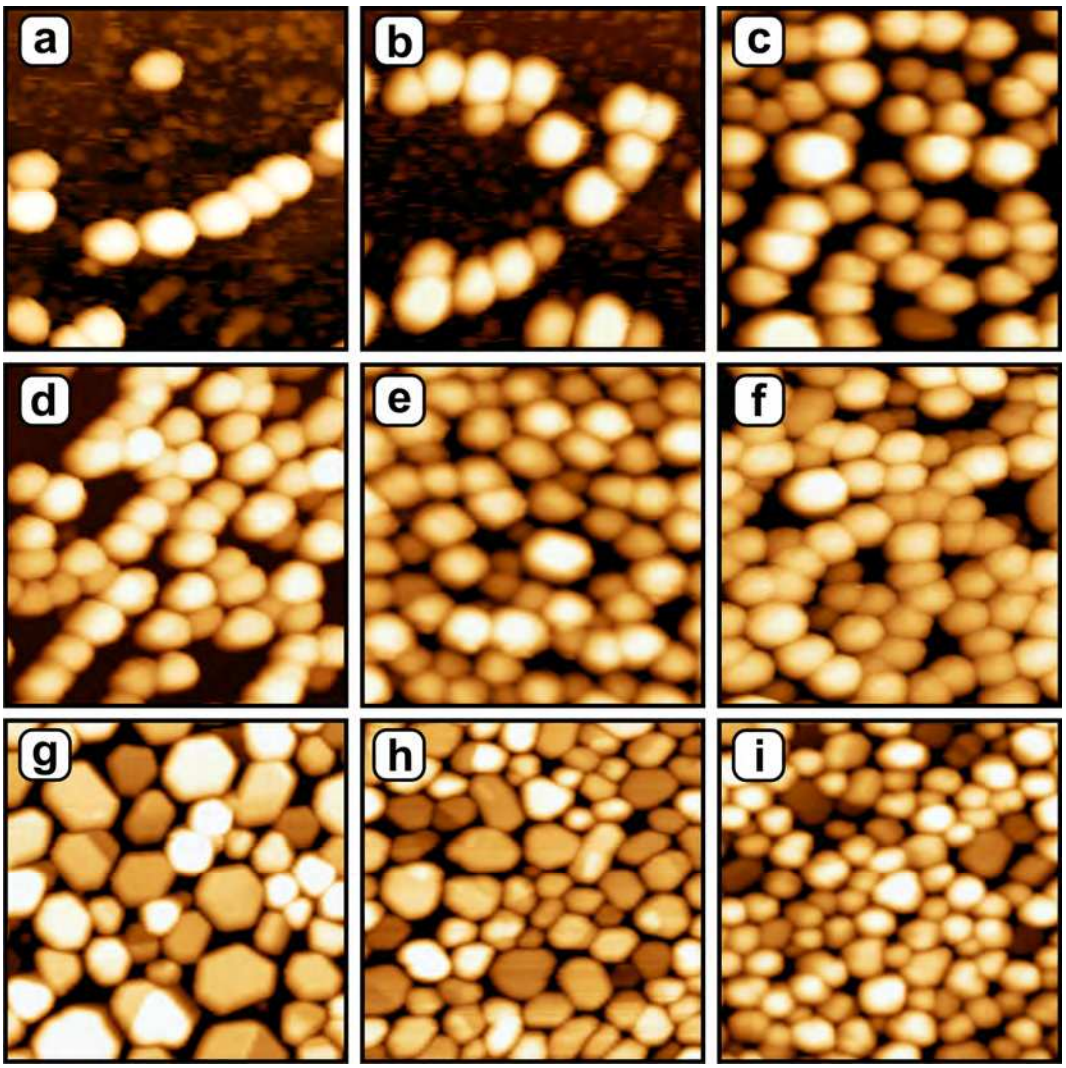

Figure 3.5: *$100\times100nm^2$ STM topographic images of dome-like (a–f) and disk-like (g–i) Ag particles on $Al_{10}O_{13}$ with increasing density. The densit y varies from 1.0×10^{11} to 8.0×10^{11} cm^{-2} and 3.5×10^{11} to 10.0×10^{11} cm^{-2} for (a) to (f) and (g) to (i) preparations, respectively.*
(Scanning conditions: U_{sample} = 1V, I = 0.05nA, PtIr tip)

The procedure, aiming to keep the density the only varying parameter in all different preparations, led to satisfactory results, especially for dome-like particle ensembles. In figure 3.6, a summary of measured heights and diameters of dome-like and disk-like particles in the different preparations is presented.

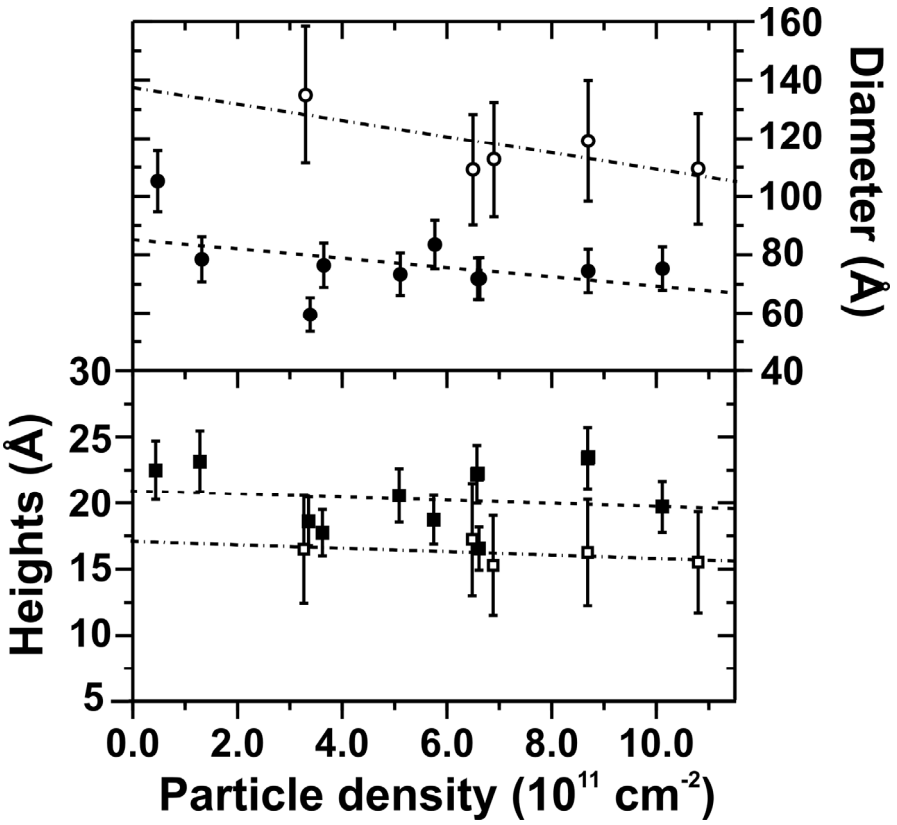

***Figure 3.6**: Average particle height and diameter for different particle densities. Closed and open symbols assign to dome-like and disk-like particle shapes, respectively. The solid lines are guides to the eye. Whereas the heights were directly measured from STM topographic images, the diameters were derived assuming ellipsoidal particle shape (see the text).*

Each data point in this figure is an average of approximately 25 single-particle height measurements. Since the height, the particle density, and the total Ag coverage are known, the diameter could be deduced by assuming an ellipsoidal particle shape. From figure 3.6, the dome-like particles have a rather regular size for the different densities, while for the disk-like ones, the size distribution is comparatively large. Nevertheless, the particle aspect ratio (height/radius) remains relatively constant for the two different shapes over the full density range. The dome-like and the disk-like particles are characterized by an aspect ratio of ~0.55 and ~0.3, respectively.

II.3. Optical properties

In order to analyze the effect of particle-particle interaction on the optical properties of dome-like and disk-like Ag particle ensembles, optical measurements were performed in the field-electron-emission regime of the STM (chap. 2, sect. III.2) with the tip bias and the field-emission current set to -240V and 1nA, respectively. At these conditions, the tip-sample distance is adjusted to ~300nm and the field-emitted electrons spread over a surface area of about 100.000nm^2, i.e., ~6×10^4 electrons/nm^2 impinge on the surface every second. Typical photon emission spectra recorded from ensembles of dome-like and disk-like particles with different densities are presented in figure 3.7. A pronounced emission line between 330nm and 350nm dominates the spectra. This photon emission is attributed to the radiative decay of Mie-plasmon in the Ag particles excited by the field-emitted electrons (chap. 1, sect. III.2.3).

Even though the radiative response has the same origin in dome-like and disk-like ensembles, the energy of emitted photons is different. Furthermore, with increasing the density of dome-like particles from 0.5×10^{11} to 10×10^{11}cm^{-2}, the Mie energy shifts from 3.50eV ± 0.02eV (354 ± 2nm) towards higher energies and reaches 3.66eV ± 0.02eV (338 ± 2nm) as depicted in figure 3.7a. For disk-like particles, the corresponding plasmon peak is around 3.75eV ± 0.02eV (330 ± 2nm), which is higher in energy compared to the dome-like ensembles. However, no apparent peak shift is revealed when increasing the particle density in this case (figure 3.7b).

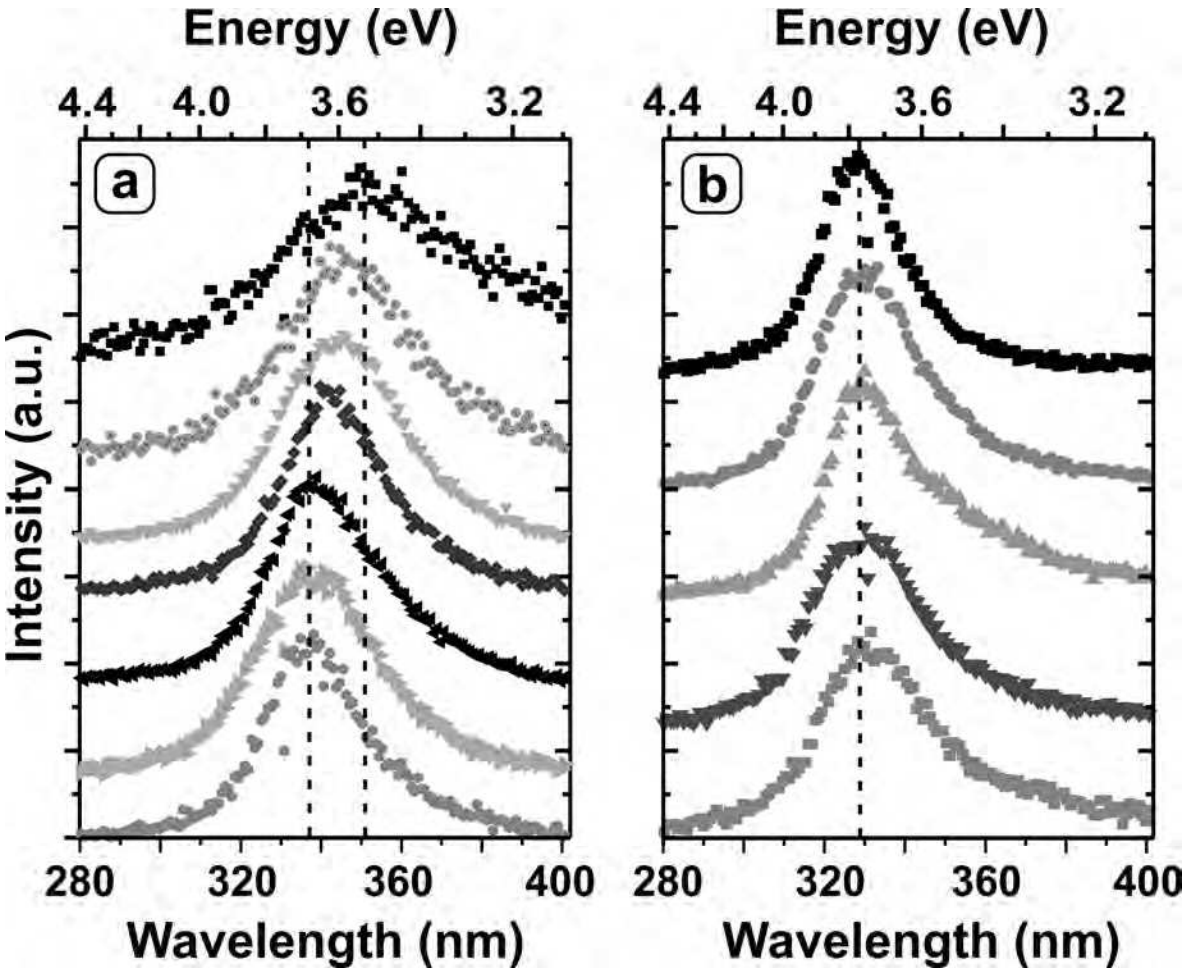

Figure 3.7: *Normalized optical spectra of Ag particles on $Al_{10}O_{13}$/NiAl(110). The spectra are presented as a function of increasing particle density from the top to the bottom,* ***(a)*** *from 0.5×10^{11} to 10×10^{11} cm^{-2} for dome-like particles and* ***(b)*** *from 3.5×10^{11} to 11×10^{11} cm^{-2} for disk-like particles. Increasing particle density leads to a blue shift of the characteristic emission line for dome-like ensembles, but does not affect the peak position in case of disk-like ensembles. The measurement conditions were U_{tip}= -240V, I= 1nA, accumulation time= 60s.*

The difference in the optical response for the different preparations is better seen in figure 3.8. The figure describes the evolution of the Mie resonance position for both particle shapes as a function of particle density. The indicated energy positions were determined by fitting the peak in the optical spectra with a Gaussian curve for all the different preparations.

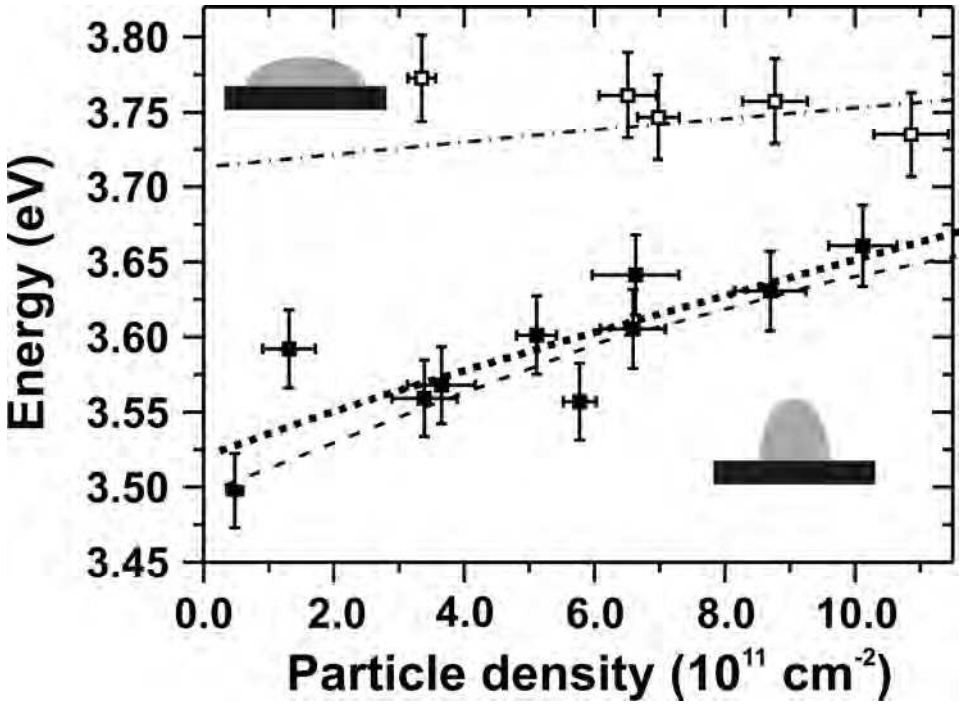

Figure 3.8: *Evolution of the energy of the (1,0) plasmon mode as a function of particle density for dome-like (closed squares) and disk-like (open squares) Ag particles. The dotted line represents a fit with a power low dependence between the energy shift and the interparticle distance d. The shift results from the dipole-dipole interaction and is found to be proportional to* $d^{-1.8}$ *(see text). The fit was performed after converting the measured densities to interparticle distances assuming a square network of particles. Dashed and dotted lines show the simulated behavior of the plasmon energy with density as calculated with the GranFilm program [115].*

II.4. Discussion

As the mean size and shape of Ag particles were kept approximately constant when increasing the particle density, the blue shift of the plasmon energy for dome-like preparations is mainly attributed to the electric dipole-dipole interactions, i.e., the coupling between the plasmon dipoles in the Ag particles.

Increasing the particle density is equivalent to a decrease of the inter-particle distance and hence a strengthening of the dipole-dipole coupling. The blue shift of the Mie resonance observed for dome-like particles results from a destructive dipole-dipole coupling that enhances when the dipoles approach each other. This behavior is typical for the interaction between the (1,0) Mie modes in neighboring particles (Chap. 1, sect. III.2.3), thus providing a clear indication that the measured photon emission in the spectra is due to the radiative decay of the (1,0) Mie mode. The latter conclusion is supported by the following observations as well: (i) The disk-like particles are characterized by a smaller aspect ratio than the dome-like ones. The energy of the (1,0) mode for flatter particles is expected to be higher than for round ones (Chap. 1, sect. III.2.3). This is in agreement with the observation in this experiment (figure 3.8). (ii) The field-emitted electrons from the tip impinge perpendicular to the substrate plane and thus preferentially excite the (1,0) mode. The in-plane oscillations are primarily excited by secondary processes, e.g., hot electron thermalization, and the excitation cross-section is much lower. (iii) The photon detection system in the experimental setup is more sensitive to light emitted from the (1,0) mode, as the corresponding radiative decay results in a photon emission parallel to the substrate plane. The decay of the (1,1) mode, on the other hand, results in a photon emission normal to the substrate surface and is therefore mainly blocked by the STM head.

The energy increase of the (1,0) mode for dome-like particles is caused by the additional energy due to the dipole-dipole interactions between the (1,0) plasmons as the interparticle distance decreases. In the general case, the interaction energy between two identical dipoles at a distance d from each other is proportional to $p^2.d^{-3}$, where p is the electric dipole moment. However, when assuming a square particle network, the fit of the measured increase of the plasmon energy reveals a dependence according to $d^{-1.8}$ for dome-like particles (figure 3.8, dotted line). Thus, in a 2D network of Ag particles, the dipole-dipole interaction energy increases slower than for two isolated dipoles as a function of distance d.

For disk-like particles, a blue shift of the (1,0) mode with increasing density is expected as well. However, no shift could be resolved most likely due to the weaker coupling. As the average height of disk-like particles is ~30% smaller than that of the dome-like ones, the

corresponding *p* of the (1,0) mode is, substantially, smaller too. Consequently, the energy of dipole-dipole interaction is almost two times smaller than for the round particles of comparable densities. In addition, the recorded Mie resonance is situated near 3.76eV, which corresponds to the surface plasmon resonance in a continuous Ag film, i.e., as *d* approaches zero. This energy marks therefore the upper limit of plasmon excitations in silver surfaces [12,116]. Besides, the absence of a shift could be related to the slightly increasing aspect ratio measured for increasing densities (figure 3.6), which lowers the Mie (1,0) energy and thus compensate the shift due to the dipole-dipole interaction.

The blue shift of the (1,0) and the red shift of (1,1) plasmon modes with increasing particle density have been observed before for lithographically fabricated particle ensembles [117,118,119]. Whereas the large particle sizes and the interparticle distances in those experiments needed an interpretation of the optical data within the framework of retardation and multipole effects [43,118], a treatment within the dipole approximation was sufficient in ref.[119]. In our experiment, the particles have smaller sizes compared to the emitted photon wavelengths. Therefore, the system is viewed in the quasi-static regime and only the dipolar effects have to be considered.

Our interpretation of the experimental results is supported by model calculations for the optical properties of dome-like and disk-like particle ensembles, as performed with the GranFilm program [115]. The code permits the determination of the polarizability of supported particles. The basic idea of the calculation method is to consider truncated spheres, oblate or prolate spheroids as geometries of the supported particles, and solve the Laplace equation for the electrostatic potential in the quasi-static regime. The mathematical form of the potential is described as a series expansion in a multipolar basis in either spherical or spheroidal coordinates to account for different particle shapes [115,120].

We computed the plasmon energies of Ag particle ensembles on a bulk Al_2O_3 substrate by calculating the absorption coefficient for varying densities using experimentally established bulk dielectric functions [121], and neglecting the NiAl substrate. As no specific lateral arrangement of the prepared particles was observed on the substrate, the mean field approach was chosen to describe their inhomogeneous lateral distribution. The particles were modeled as truncated spheroids determined by a perpendicular ($r_\perp$) and a parallel ($r_{||}$) radius corresponding to the experimental particle height and radius, respectively. Hence, the dome-like particles are characterized by $r_\perp > r_{||}$ and the disk-like particles by $r_\perp < r_{||}$.

Several combinations of radii were tested in order to reproduce the experimental results. However, optimum agreement was achieved only for a narrow range of radii. In figure 3.8, two curves are shown representing the calculated evolution of the plasmon energy with particle density for the dome-like (dashed line) and the disk-like (dash-dotted line) particles. The theoretical curves describe the measured data rather well, and thus, illustrating the

dominant role of the dipole-dipole interaction in the experiment. The experimental data point at a density of $1.31\times10^{11}cm^{-2}$ deviates to higher energies from the calculated evolution for round particles. This emphasizes the increased particle-particle coupling due to the high local density, as the Ag particles preferentially nucleate along the defect lines of the alumina surface (figures 3.2 and 3.5).

The optimal input values of particle radii were $r_\perp$ = 46Å, $r_\parallel$ = 32Å, and $r_\perp$ = 27Å, $r_\parallel$ = 40Å for round and flat particle shapes, respectively. The calculated values of $r_\perp$ overestimate the measured heights by almost a factor of two. This means larger dipolar moments are needed to reproduce the experimental energy positions of the (1,0) plasmon. This effect is attributed to the neglect of the NiAl support below the Al_2O_3 film in the calculations. Therefore, the induced image dipoles in the NiAl were not taken into account. As the image dipole couples constructively with the driving (1,0) dipole in the particle, it enhances the total polarizability of the system (Chap. 1, sect. III.2.3). To judge the importance of this effect, we simulated the case of Ag particles deposited directly on a NiAl support. Fitting this model to the experimental dependence of the plasmon energy on the density leads to a much better agreement between calculated und measured shapes. It results in an $r_\perp$ = 33Å for the round and $r_\perp$ = 20Å for the flat particles, which are comparable with the heights deduced from the measurements. However, computed line widths and energy positions of the Ag Mie plasmon deviate more strongly from the experimental results for a NiAl support compared to Al_2O_3 surface. This underlines the combined influence of the oxide film and the metal substrate on the optical properties of the supported Ag particles.

III. Effect of long-range order

III.1. Ag nanoparticle synthesis

The silver nanoparticles used to fabricate long-range ordered ensembles were prepared in the research group of Professor Pileni at the University of Paris. The nanoparticles were synthesized in a chemical approach using the reverse micelle technique. The reverse micelles are water droplets stabilized in oil by means of a surfactant. They are used as micro-reactors to realize the synthesis of silver nanoparticles via chemical reduction. The synthesis procedure is described in references [122,123]. It can be summarized as follows: Two micellar solutions of surfactants/isooctane (C_8H_{18}) and water having the same molar ratio W = [H_2O]/[surfactant] = 40 are mixed together. One solution contains 30% Silver-bis(2-ethylhexyl)sulfosuccinate (known as Ag(AOT) or $C_{20}H_{37}O_7S$-Ag) and 70% Sodium-bis(2-ethylhexyl)sulfosuccinate (known as Na(AOT) or $C_{20}H_{37}O_7S$-Na) as surfactants. The second solution contains 100% Na(AOT) and a sufficient amount of hydrazine (N_2H_4) solved in water. The role of hydrazine is to reduce the Ag^+ cations and break the bonding to the AOT. Silver reduction is achieved during the collisions between different micelles, which permit the exchange of their aqueous nuclei. The procedure results in the formation of Ag nanoparticles with an average diameter of 5nm and a size distribution of about 43%. To extract the particles, dodecanethiol ($C_{12}H_{25}SH$) is added just after the particle formation. Because of the strong affinity of their SH head-group to silver, the dodecanethiol chains attach to the particle and form a monolayer around it. The surfactant is afterwards removed by precipitation in ethanol. Repeated size-selective precipitation processes followed by centrifugation yield a size distribution about 8%. The particles are afterwards dispersed in hexane C_6H_{14} and a homogeneous colloidal solution is obtained.

III.2. Ag nanoparticle deposition

The deposition of the Ag nanoparticles was done in ambient conditions. A few micro-liters of low concentrated colloidal solutions were dropped onto the surface of HOPG (Highly Ordered Pyrolytic Graphite) surface. Prior to deposition, the HOPG was prepared by stripping off the upmost graphite layers with adhesive tape. In figure 3.9, a STM topographic image of a clean HOPG surface is presented.

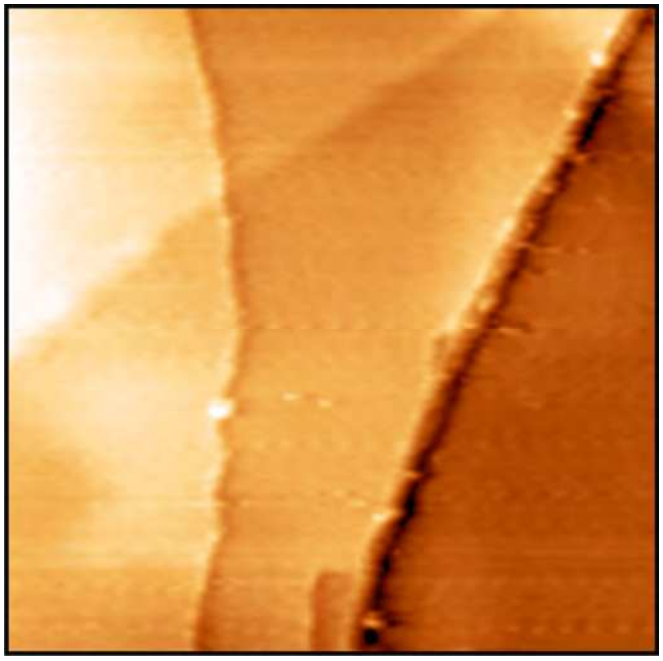

Figure 3.9: *100x100nm^2 STM topographic image of the HOPG surface prepared by peeling off the surface and introducing it into the UHV chamber. The image describes the morphological state of the HOPG surface after its preparation. The surface is characterized by flat and large terraces separated by randomly oriented step edges caused by surface peeling. U_S = 0.4V, I =0.35nA, PtIr tip.*

Two different colloidal solutions, extracted before and after the size-selective precipitation processes, were analyzed. The corresponding particle size distributions in the solutions are therefore 43% and 8%, respectively. The samples are introduced into the vacuum 1h after the deposition, so that the hexane evaporates outside the vacuum chamber. Figures 3.10a and 3.10b show TEM (Transmission Electron Microscopy) images of a monolayer of poly- and mono-dispersed Ag particles deposited on HOPG. Whereas no long-range order is observed in figure 3.10a, a hexagonal 2D superstructure is noticed in figure 3.10b. This self-organization of particles is induced by the small size distribution. The TEM observations are confirmed by STM measurements, as illustrated in figures 3.10c and 3.10d. The preparations shown in figures 3.10a and 3.10c are named *disordered ensembles* in the following, while the ones in figures 3.10b and 3.10d are termed *ordered ensembles.*

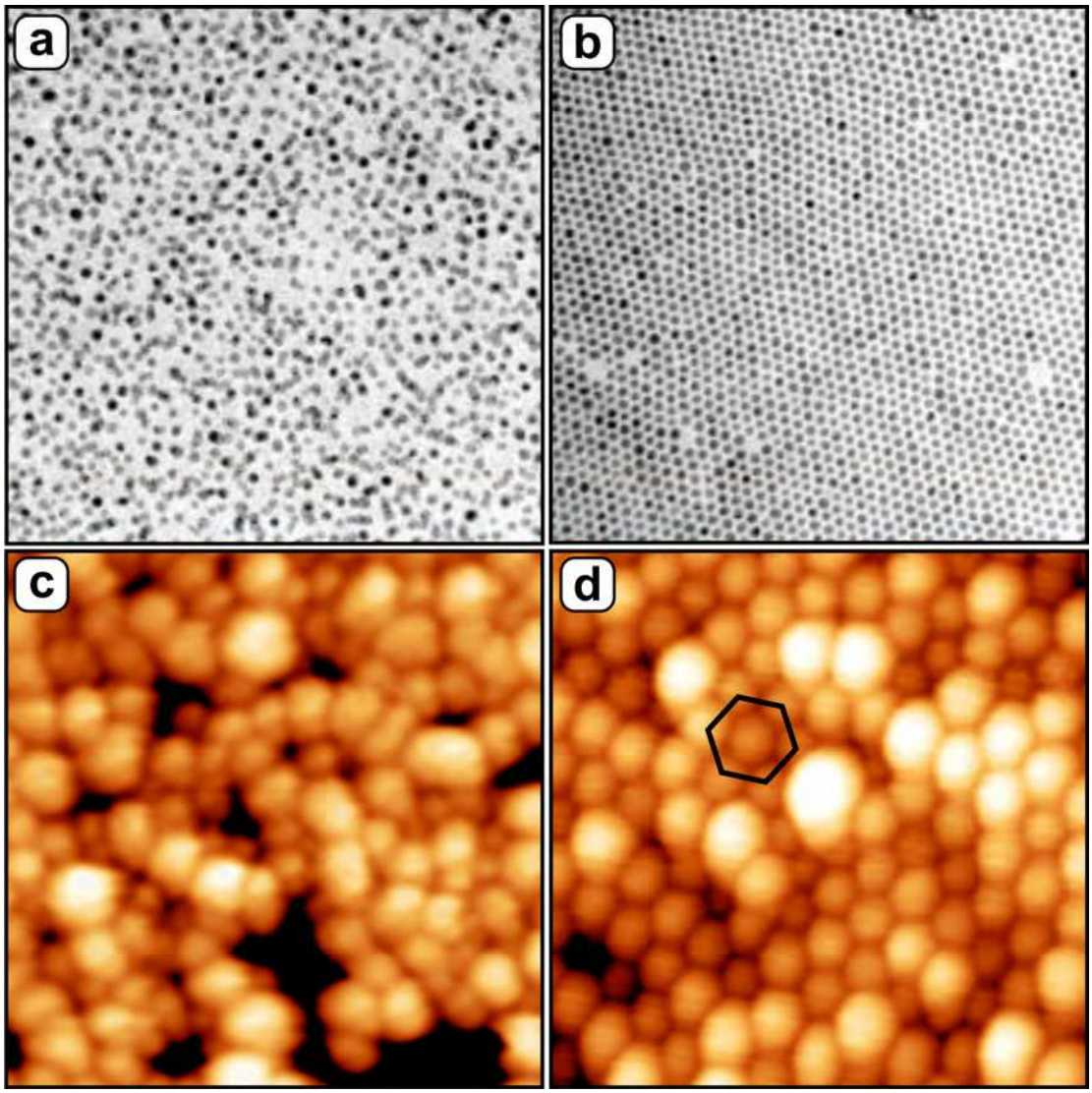

***Figure 3.10: (a** and **b)** 300x300nm^2 TEM images of a monolayer of Ag nanoparticles synthesized by the reverse micelle technique deposited on HOPG with (a) 43% and (b) 8% size distribution. **(c** and **d)** 75x75nm^2 STM topographic images of similar preparations as in (a) and (b), respectively. U_S =0.4V, I=0.5nA, PtIr tip. The drawn hexagon in (d) emphasizes the hexagonal network with a 7nm lattice in which the particles arrange themselves.*

The hexagonal organization of the particles in the ordered ensemble is characterized by a lattice constant of 7nm (figure 3.10d) and a mean particle density of about $23.5\times10^{11}\,\mathrm{cm}^{-2}$. This organization is induced by the presence of the dodecanethiol chains attached to the particles, as the surrounding hydrocarbon chains protect the particles from surface wetting and coalescence, and preserve their shape and size even at the highest density. Hence, as modeled in figure 3.11 [124], the Ag particles keep their spherical shape, which is important for their

optical properties. Furthermore, the dodecanethiol chains of adjacent particles imbricate and ensure a minimum separation between the particles of about 2nm. This value plus the particle diameter (5nm) fixes the lattice constant of the Ag particle network on the HOPG support to 7nm, and also determines the interparticle separation normal to the surface in case of a multilayer deposition. The rather big Ag particle-HOPG spacing leads to a weak coupling between the particles and the support. This effect is also experienced during the STM measurements where imaging was only possible for optimized tunneling conditions. Although, the ligand shell present an additional difficulty for tunneling, due to their insulating character and their swaying movement.

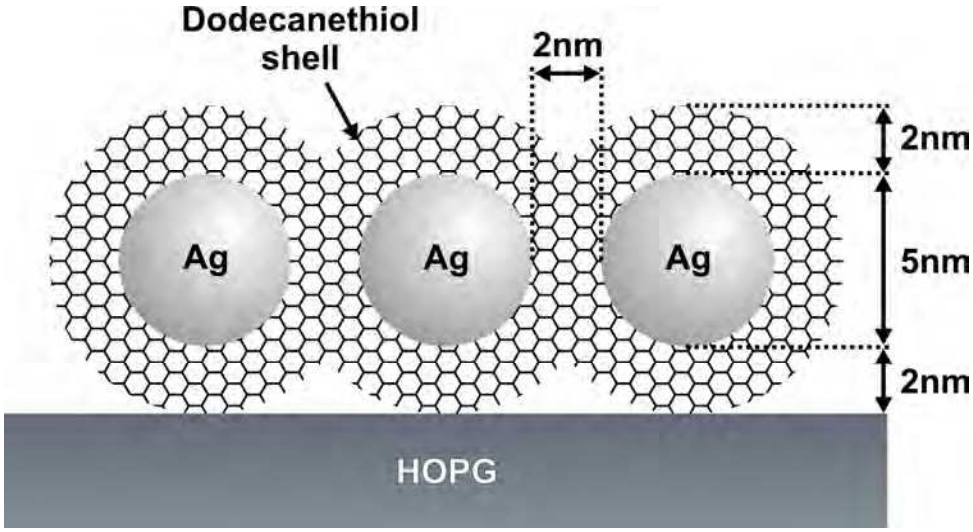

Figure 3.11: *Schematic model of Ag colloids on HOPG*

III.3. Optical properties

As in case of Ag particles prepared by vapor deposition on alumina (sect. II), the optical properties of ordered and disordered Ag nanoparticle ensembles on HOPG were analyzed by bombardment with field-emitted electrons from the STM tip. In order to investigate the effect of the lateral size of the excited ensemble on the optical response, the field-emission bias was varied from -90V to -160V for a current adjusted to 1nA. This is achieved by setting the STM tip-sample distance to values between ~100nm and ~250nm, so that the analyzed area varies roughly between ~10.000 nm^2 and ~70.000 nm^2. No electron-induced damage is noticed in STM images taken after each spectroscopic measurement. The recorded optical spectra are presented in figure 3.12. The spectra were fitted with two Gaussians to determine the respective peak positions and intensities. The emission spectra from the ordered ensemble are characterized by a maximum at 3.6eV ± 0.02eV (345nm ± 2nm) and a shoulder at around 2.47eV ± 0.02eV (500nm ± 2nm) (see figure 3.12a). The full-width-at-half-maximum (FWHM) of the high-energy peak is approximately three times smaller than the one at low energy. The total emission yield increases exponentially with electron energy, but no obvious change of the spectral shape and peak positions is observed. Thus, no effect related to the size of the ensemble is seen in the optical response within the analyzed area range. For the disordered particle ensembles, the optical measurements show a qualitatively similar behavior compared to the ordered ensemble (figure 3.12b). The most pronounced difference is the reduced intensity of the low energy shoulder. For the ordered ensembles, the intensity ratio between low energy and high-energy peaks is found to be 0.45. The equivalent ratio drops to 0.35 for the disordered ensemble. Furthermore, the high-energy peak for disordered ensembles is slightly blue shifted to 3.65eV ± 0.02eV (340nm ± 2nm) and slightly more intense.

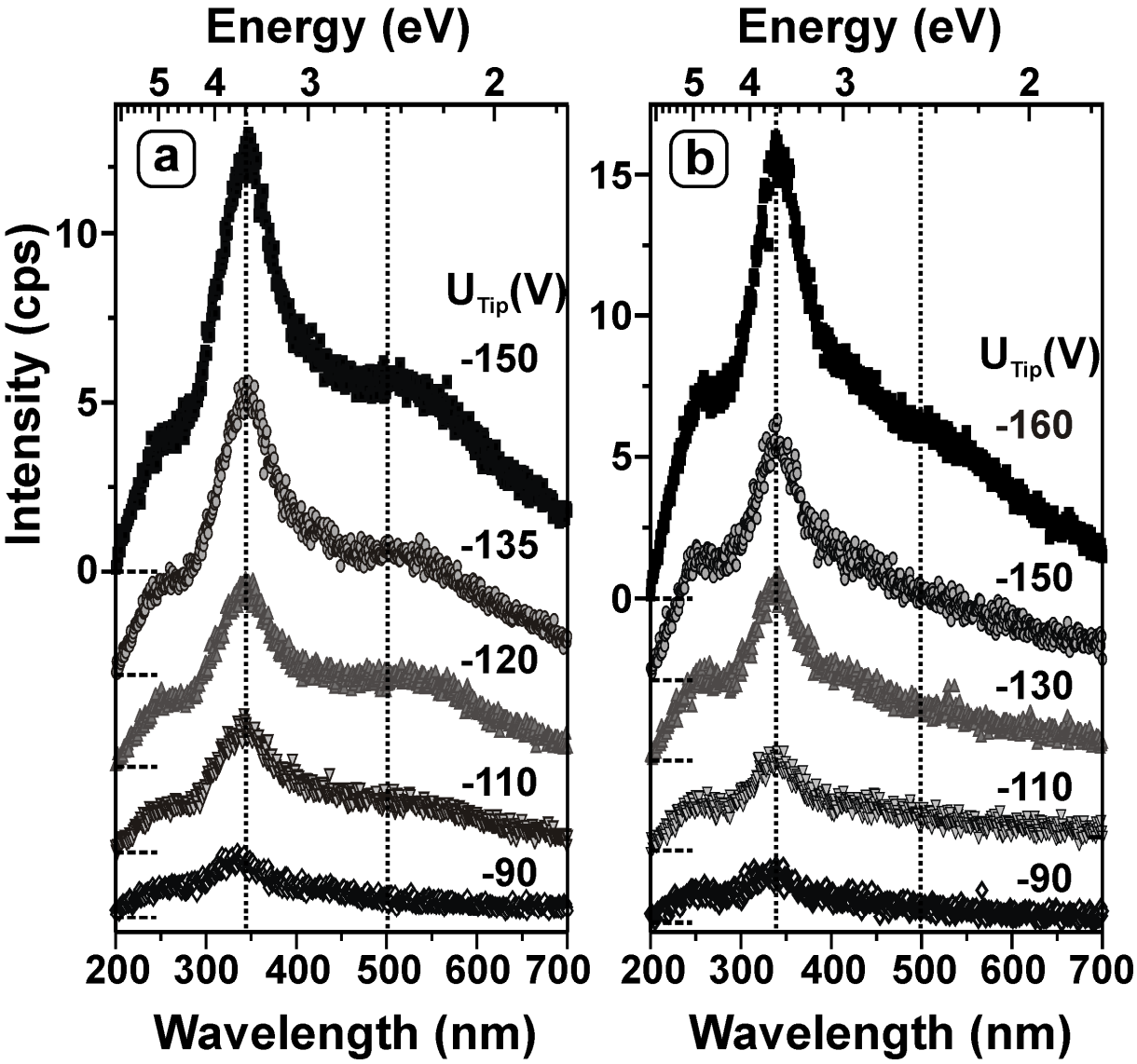

Figure 3.12: *Photon emission spectra of* ***(a)*** *an ordered and* ***(b)*** *a disordered 2D monolayer of Ag particles on HOPG. The particles were excited in the field-emission regime with different tip voltage. The current was adjusted to 1nA for 60 seconds recording time.*

III.4. Discussion

The photon emission from both ensembles is assigned to the radiative decay of the Mie plasmon in the metal particles[3]. The plasmons are excited by the field-emitted electrons injected into the sample surface with high kinetic energy (chap. 1, sect. III.2.3). Apparently, the plasmon is split into two modes separated by an energy gap of about 1.1eV. Using equation (1.24), the position of the Mie resonance in a single spherical silver particle can be estimated when taking into account the presence of dodecanethiol shell. Assuming a dielectric function of the surrounding medium of $\varepsilon_m = 2$ [124], the calculated fundamental Mie mode is found to be at 3.2eV. This position is red-shifted compared to the calculated Mie position for the same particle in vacuum (3.5eV), emphasizing the role of the dodecanethiol shell that increases the particle polarizability.

Since the Ag colloids do not wet the HOPG substrate and remain spherical, a splitting of the fundamental Mie mode into the (1,0) and (1,1) modes due to particle shape anisotropy can be neglected. In addition, the interaction of the Ag particles with the image dipoles (chap. 1, sect. III.2.3) in the HOPG substrate is weak and leads to a splitting of the Mie Mode of only some meV [125]. However, the close packing of the particles, especially for the ordered ensembles, is undoubtedly the origin of strong dipole-dipole interactions in the ensemble layer. This results in two Mie modes, namely the (1,0) and (1,1) modes, which are blue- and red-shifted with respect to the fundamental plasmon in an isolated sphere, respectively (see chap. 1, sect. III.2.3). Therefore, we assign the high-energy photon-emission peak observed here to the (1,0) mode, and the shoulder at low-energy to the (1,1) mode. This conclusion is supported by the high intensity of the out-of-plane (1,0) mode at 3.6eV, since it is preferentially excited in the experiment (sect. II.4).

The peak assignment to the different Mie modes can be verified experimentally by analyzing the polarization of the emitted light, as shown for the ordered ensembles in figure 3.13a. The experiment was done by placing a Glan-Thompson polarizer at the entrance slit of the spectrograph. The emission peak at 3.6eV shows the expected intensity variation for linear polarized light as a function of the polarization angle ϕ [126]: $I(\phi) = I_0 \sin^2\phi$ (figure 3.13b). The maximum intensity is found when the polarization angle is around 90°. According to the geometry of our optical setup, the only light able to pass the polarizer at 90° is *p*-polarized light resulting from an emission involving the (1,0) plasmon, which oscillates perpendicular to the surface. The small emission yield of the low-energy peak and background intensity in this energy range prevented similar investigations for the (1,1) mode.

[3] Except the Bremsstrahlung radiation observed around 250nm in the spectra.

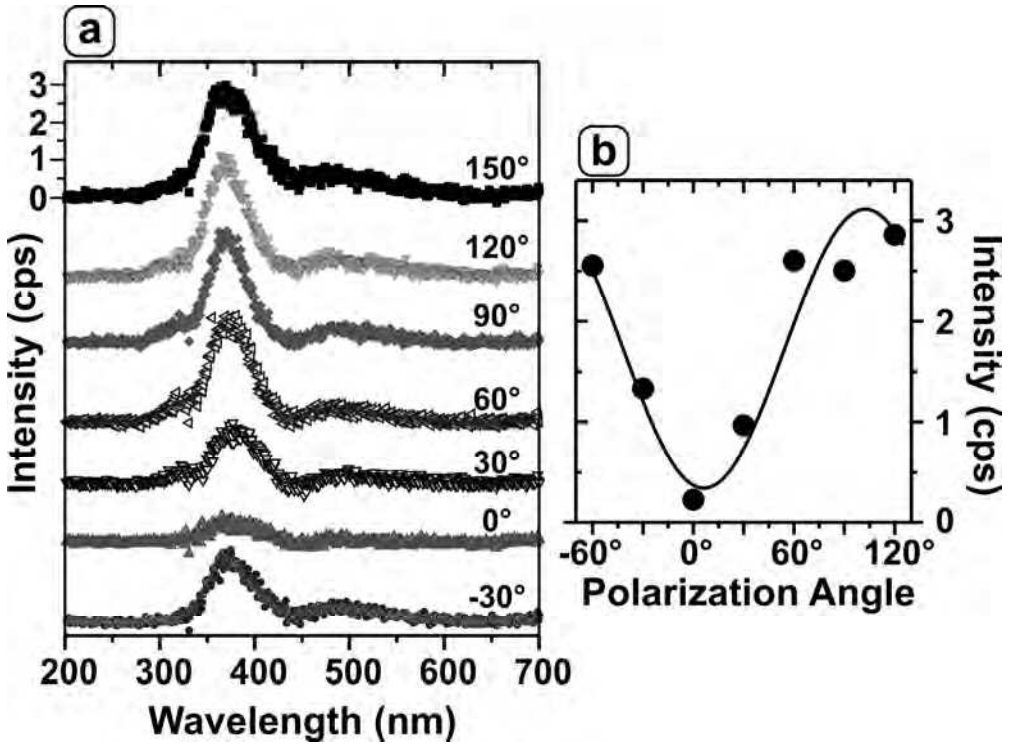

Figure 3.13: (a) *Polarization angle dependence of the light emission from an ordered monolayer of Ag colloids on HOPG excited by field-emitted electrons from the STM tip. Tip bias and electron current were set to -220V and 1nA. The background independent of the polarization is subtracted. Peak positions are slightly red-shifted due to a geometrical effect caused the presence of the polarizer at the spectrograph entrance.* ***(b)*** *Intensity variation of the main peak in (a) as a function of polarization angle.*

Experimental and calculated reflectivity spectra performed for an ordered network of Ag nanoparticles on HOPG, revealed observations comparable to ours [124,127]. Herby, the calculated positions for low- and high-energy peaks were found to be at 2.38eV and at 3.34eV, respectively, while the experimentally revealed peak positions are at 2.15eVand 3.50eV. The second peak appeared only when the incoming angle of the *p*-polarized excitation light is suitable to excite the perpendicular plasmon mode in the particles. The discrepancy between measured and calculated results in [124,127] is attributed to the inappropriate description of the polarizability of the single particle on the HOPG, which treats the environment as a homogeneous medium and neglects the real stacking of the dielectric layers. An additional deviation could arise from the use of simplified dielectric functions for the ligand shell.

No pronounced effect of the regular versus disordered arrangement of particles on the optical properties could be established from our experimental data. Apparently, the splitting of the fundamental Mie plasmon is a subtle indicator for changes in the particle density, but is

less sensitive to the long-range order in the particle ensemble. The average inter-particle distance was found to be comparable in ordered and disordered ensembles, which might explain the similar plasmon energies observed for both preparations. On the other hand, small variations in the plasmon position are likely to be covered by the large FWHM of the experimental peaks. The absence of long-range order in the disordered ensembles is, however, reflected in the intensity loss of the low-energy shoulder. In a perfect hexagonal network, the (1,1) mode gains intensity with respect to the (1,0) mode, because of the constructive coupling, and therefore the enhancement, of the in-plane oscillations. The out-of-plane modes, on the other hand, experience a destructive coupling. In assemblies with broader size distribution, this effect is partly suppressed due to a detuning of the plasmon energies and hence a reduced coupling efficiency between neighboring particle dipoles. Consequently, the energy splitting as well as the intensity ratio between the (1,1) and the (1,0) emission peaks decrease in ensembles without long-range order. This is in agreement with the experimental results (figure 3.12b).

The rather large FWHM of the emission peaks of the Ag nanoparticles on HOPG is mainly attributed the dodecanethiol environment, which decreases the plasmon lifetime by inducing an additional damping [6,12,124,128]. This fact becomes apparent when comparing a spectrum of an ordered ensemble of Ag colloids with a one of bare Ag particles vapor deposited on an alumina film (sect. II.2). Such a comparison is presented in figure 3.14, where a normalized spectrum from an ordered Ag colloidal ensemble with a particle density of $23.5\times10^{11}cm^{-2}$ is shown next to spectrum of a dense round Ag particles on alumina (density $10.12\times10^{11}cm^{-2}$) (sect. II.3). Regardless the differences in particle size, shape and density between the two samples, the FWHM of the (1,0) peak for the Ag colloids is found to be bigger by a factor of three with respect to the bare particles.

Another obvious difference in figure 3.14 resides in the absence of the (1,1) mode in the spectrum of $Ag/Al_{10}O_{13}/NiAl(110)$. This underlines again the strong influence of the dipole-dipole coupling in the dense well ordered Ag particle layer, which leads to a huge amplification of the photon emission yield from the (1,1) plasmons. The corresponding spectral peak becomes therefore visible in the spectra despite the unfavorable detection symmetry as well as the small excitation cross-section of the (1,1) mode in our optical system.

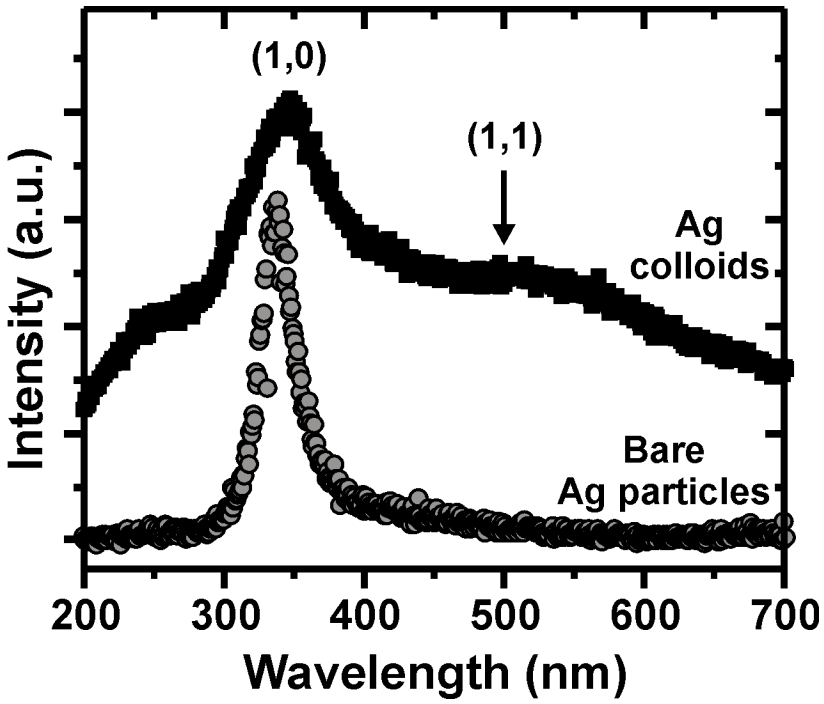

Figure 3.14: *Comparison between normalized emission spectra from a monolayer of ordered Ag colloids on HOPG and a dense Ag particle ensemble supported on alumina. The fitting of a Gaussian curve to the (1,0) peaks gives a FWHM of ~58nm for the colloids and ~20nm for the bare particles. The appearance of the (1,1) peak in the top spectrum emphasizes the strong interparticle dipole-dipole coupling in the ordered and close packed particle layer, which render its detection possible.*

In the light of the above results, we discuss the optical response from a single particle and a 3D structure consisting of a multilayer of Ag colloids on HOPG in the following paragraphs.

An optical spectrum of a single Ag particle within an ordered ensemble is presented in figure 3.15a. It was measured with a low excitation bias (15V) and a rather high current (5nA). The high current was required to increase the emitted-photon yield from the single emission center above the optical detection limit. At these conditions, structural damage cannot be excluded. The spectral characteristics are similar to the particle ensemble spectra obtained at higher electron energy. Here, the two peaks are at 3.18eV ± 0.02eV (390nm ± 2nm) and at 2.1eV ± 0.02eV (590nm ± 2nm). Whereas, the high-energy peak is attributed to the (1,0) mode, the origin of the low-energy feature is unclear although its position would correspond to the (1,1) mode. As discussed above, photon emission from the (1,1) of a single

particle is not expected to be detected. Therefore, the low-energy peak (2.1eV) is, more likely, the result of a coupled electromagnetic mode between the tip and the sample (tip-induced plasmon (TIP), see chap.1 sect. III.2.1) and does not represent an intrinsic excitation of the Ag particle. The position of (1,0) plasmon is red-shifted by 0.42eV with respect to the spectra obtained from the Ag ensemble, but it is similar to the calculated position for a single particle. Nevertheless, the particle cannot be considered as isolated, since it is within the ordered layer, and therefore it should undergo coupling-effects with the image dipoles induced by its (1,0) mode in the neighboring particles. However, the small change of the (1,0) peak position compared to an isolated particle reveals the weak coupling with the induced images diploes. This is in contrast with the simultaneous excitation of an ensemble of ordered particle, where the (1,0) mode of every particle experiences an efficient destructive coupling with the dipoles of the neighboring particles. On the other, also the presence of the metallic tip near the particle might influence the polarizability of the system [12,89].

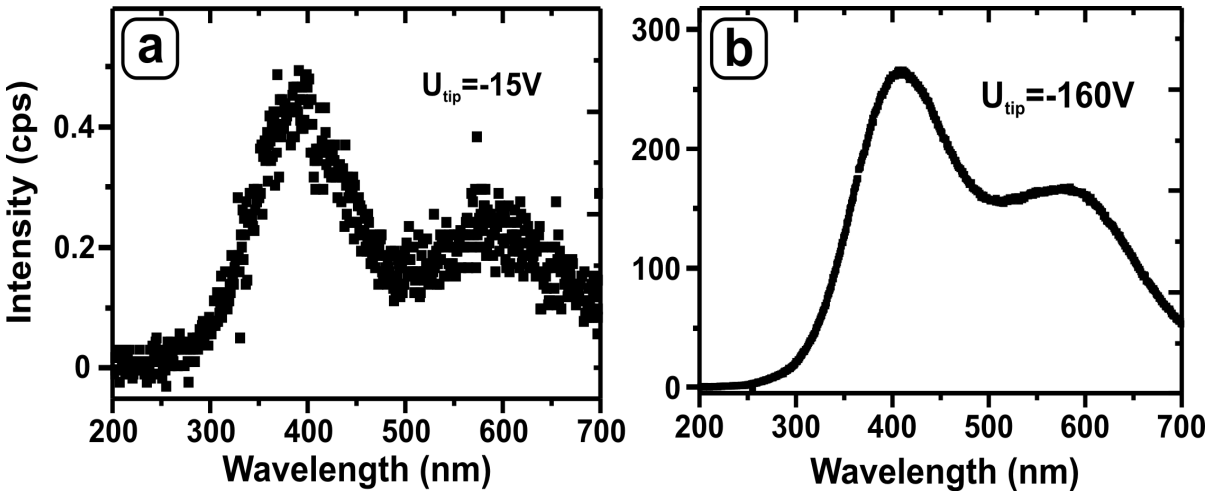

Figure 3.15: *Photon emission spectrum of* ***(a)*** *a single Ag particle within an ordered layer of Ag nanoparticles and* ***(b)*** *a multilayer of size-selected Ag nanoparticles, on HOPG. The spectra were obtained after particle excitation in (a) the tunneling regime (U_{tip}=15V, I=5nA), and (b) the field emission regime.*

Multilayer samples were prepared by dropping a highly-concentrated colloidal solution on the HOPG support. Based on the concentration required for the deposition of one monolayer, the thickness of the multilayer film was estimated to be between 5 to 10 layers. The insufficient conductance of the thicker film prevented the recording of STM topographic

images. However, as shown in figure 3.15b, optical measurements were possible due to the increased mean free path of the energetic field-emitted electrons. The optical response is characterized by a red shift of the two emission peaks as well as by an intensity increase by a factor of 25 compared to the monolayer films. The elevated intensity reflects the increased number of photon emission centers. The high- and the low- energy peaks in the multilayer sample are detected at 3.06eV ± 0.02eV (405nm ± 2nm) and at 2.21eV ± 0.02eV (560nm ± 2nm). The red shift of the (1,0) mode is found to be 0.55eV, which is more pronounced than the shift of the (1,1) mode (0.3eV). This effect is mainly attributed to the additional electromagnetic coupling induced by the particle over layers. Thereby, the (1,0) and (1,1) modes experience coupling effects that are opposite to the ones in the monolayer. Plasmon modes of particles in different layers couple constructively for the out-of-plane modes and destructively for in-plane modes. In other words, in an infinite 3D particle ensemble, the coupling effects should be compensated and therefore only one peak is expected to show up in the optical emission. Indeed, the energy separation between the two plasmon modes decreases from 1.1eV in the monolayer to 0.85eV in the film of 5-10 layers. Apparently, since for a 5 to 10 layers thick film an energy gap between (1,0) and the (1,1) modes still exists and much higher thickness are required to converge the two modes into a one single mode.

The plasmon energy of an infinite 3D particle agglomeration can be estimated using the following formula, deduced from Maxwell-Garnett's effective medium theory [12]:

$$\varepsilon_{eff}(\omega) = \varepsilon_m \frac{1 + 2f\Lambda(\omega)}{1 - f\Lambda(\omega)} \tag{3.2}$$

hereby f is the filling factor defined as $f = V_{particles}/V_{film}$ with V is the volume, and $\Lambda = \alpha(\omega)/3\varepsilon_0\varepsilon_m$. ε_m is the dielectric function of the surrounding medium, ε_{eff} is the effective dielectric function, and $\alpha(\omega)$ the polarizability of an isolated single particle. The Maxwell-Garnett's effective medium theory is only valid for small f.

For the given parameters f = 0.27 (only the metal part of the colloid is considered) and ε_m = 2, the calculated plasmon position for an infinite multilayer of Ag ordered nanoparticles is found to be 2.9eV which is 0.3eV lower than for an isolated particle.

IV. Conclusion

We have studied the influence of the geometrical configuration of supported silver nanoparticles on their optical behavior. The effect of aspect ratio, density, and lateral arrangement of the particles in the ensemble were investigated by the photon-STM technique. Hence, a direct correlation could be made between the imaged topography of the particle ensemble and its optical spectrum obtained via excitation with field-emitted electrons from the STM tip. Dome and disk shaped Ag particles on $Al_{10}O_{13}$/NiAl(110) with increasing particle density were prepared. The respective particle aspect ratios were in average ~0.55 and ~0.3. To account for lateral arrangement effects, Ag colloidal ensembles with a spherical particle shape were deposited on HOPG substrates. The size-selected Ag colloids self-assemble on the HOPG surface and form a close-packed hexagonal network.

The recorded optical spectra were dominated by the (1,0) Mie plasmon excitations. The resonance position of the observed Mie mode is found to be strongly dependent on the electromagnetic coupling between the plasmon dipoles in particles with high aspect ratio. The strength of the coupling turned out to be governed by the interparticle distance only in the dome-like particle ensemble. For the disk-like particles, no evident effect on the optical spectra is remarked when varying the particle density. This marks the reduced influence of the dipole-dipole interaction between extremely flat particles. On the other hand, the regular array of Ag nanoparticles is found to induce a high dipole-dipole coupling within the ensemble. This leads to the enhancement of the spectral intensity of the (1,1) Mie mode, due to the constructive in-plane coupling. However, ensembles with either well-ordered or disordered arrangements exhibit in general a similar optical spectral distribution and reveal no important difference, which reflects the weak influence of the long-range order of in particle ensembles.

Chapter 4

Morphological and Optical Properties of MgO Thin Films on Mo(001)

I. Introduction

Magnesium oxide is considered as a prototype material for wide band-gap insulators [129,130]. The reason is its simple atomic configuration consisting of two atoms in the unit cell of a cubic structure (figure 4.2). This quality makes it easier to be studied both experimentally and theoretically, and therefore, develop a good starting point to approach the more complex systems. In addition, magnesium oxide is gaining more and more attention in fields like heterogeneous catalysis as bare oxide [131,132,133] or as support for metal particles [134,135,136,137], and in the field of photocatalysis [138]. It is also considered to be a very good insulator barrier in the high-performance magnetic tunnel junctions used in spintronic devices [139,140,141,142].

The properties of MgO, such as optical performance and chemical reactivity, are mainly determined by the type of defects present in the surface [21,143]. The nature of these defect sites on MgO single crystal and film surfaces is already probed using different techniques, namely, electron-energy-loss spectroscopy (EELS) [144,130], infrared spectroscopy (IR) on adsorbed molecules [145,146], metastable impact electron spectroscopy (MIES) [147], scanning tunneling microscopy and spectroscopy (STM/STS) [156], electron paramagnetic resonance (EPR) [148], and by cathodoluminescence and photoluminescence spectroscopy [149,150,151].

The analysis of the MgO surface on thin MgO films deposited on metal substrates has the advantage of avoiding electrical charging encountered during the experiments on single MgO crystals [20]. The ideal preparation technique should produce films with a similar surface structure as for a single crystal. However, the preparation of such films is not an easy task, since many parameters have to be controlled [152]. The main issue is to use a metal substrate that is characterized at the same time by (i) a small lattice mismatch with the MgO film to avoid strain effects, (ii) a high melting temperature that allows high-temperature annealing to improve film quality, and (iii) a low affinity to oxygen.

MgO thin films were deposited mainly on Ag(001) [153,154,155,156], Fe(001) [140,157], and Mo(001) [158,159,160] substrates, resulting in lattice mismatches of 3.0%, 3.7% and 5.3%, respectively. Ag(001) seems to be the most suitable substrate. However, this is only the case for very thin MgO films (3ML to 8ML [161]). The low Ag melting point prevents from annealing thicker films and improving the film structure. The molybdenum substrate is in this case better suited.

Theoretical as well as experimental studies showed that MgO thin-films exhibit the same chemical features as single MgO crystals [162], but they differ in certain properties (like the CO binding energy on the surface), due to the high concentration of defects in the films [163]. However, despite the possibility to treat the MgO films at high temperatures on Mo substrates and reduce the number of defects, the properties of the MgO/Mo system have not been extensively studied in the past.

Our work represents the first investigation of the optical properties of extended- as well as local-areas of MgO thin films with different thicknesses deposited on Mo(001). Moreover, using the photon-STM, a correlation between the optical behavior and the morphology of thin MgO films could be made.

In this chapter, we first discuss the evolution of the MgO/Mo(001) film morphology as a function of thickness. Thereby, Low Energy Electron Diffraction (LEED) and Grazing Incidence X-ray Diffraction (GIXD) techniques are used to analyze the film crystallographic structure, while STM is employed to depict the local topography of the film surface. Afterwards, the optical characteristics of the MgO film is explored for various film thicknesses. The optical activity of MgO films is stimulated by electron injection from the STM tip in both the field emission and tunneling modes (chap.2, sect. III.2). By performing field-emission excitations, the sites responsible for the optical activity of MgO are identified using two complementary approaches: (i) A direct correlation of the optical response with the features visible in surface imaging. (ii) Analysis of the nucleation behavior of gold particles on MgO films and its effects on the intrinsic MgO light emission. The exploration of the Au nucleation behavior provides not only information about the optically active MgO center, but at the same time, enables to link these centers to the preferential nucleation sites of Au on MgO.

Besides, by performing STM measurements in the tunneling mode, we explore the possibility to locate the optically active centers in the MgO surface by simultaneous topographic and optical measurements.

In the following, a short introduction into the general MgO properties shall be given.

I.1. Magnesium oxide (MgO): Bulk vs. Surface

In the calculated phase diagram of the magnesium-oxygen system, shown in figure 4.1 [164], magnesium oxide with a stoichiometry of Mg_1O_1 (or MgO) is the only stable phase. Other phases with higher oxygen content exist, but are only stable in a tight temperature range (see Table 4.1) [165,166,167]. An experimentally determined phase diagram of the system is so far not established.

The magnesium oxide in its stable MgO phase is one of the most abundant oxides in earth's crust. It is known in mineralogy under the name *"Periclase"*. It is found to be structurally stable up to pressures as high as 227GPa [168], which makes it a model system for the research on materials at ultrahigh pressures, both experimentally and theoretically [169].

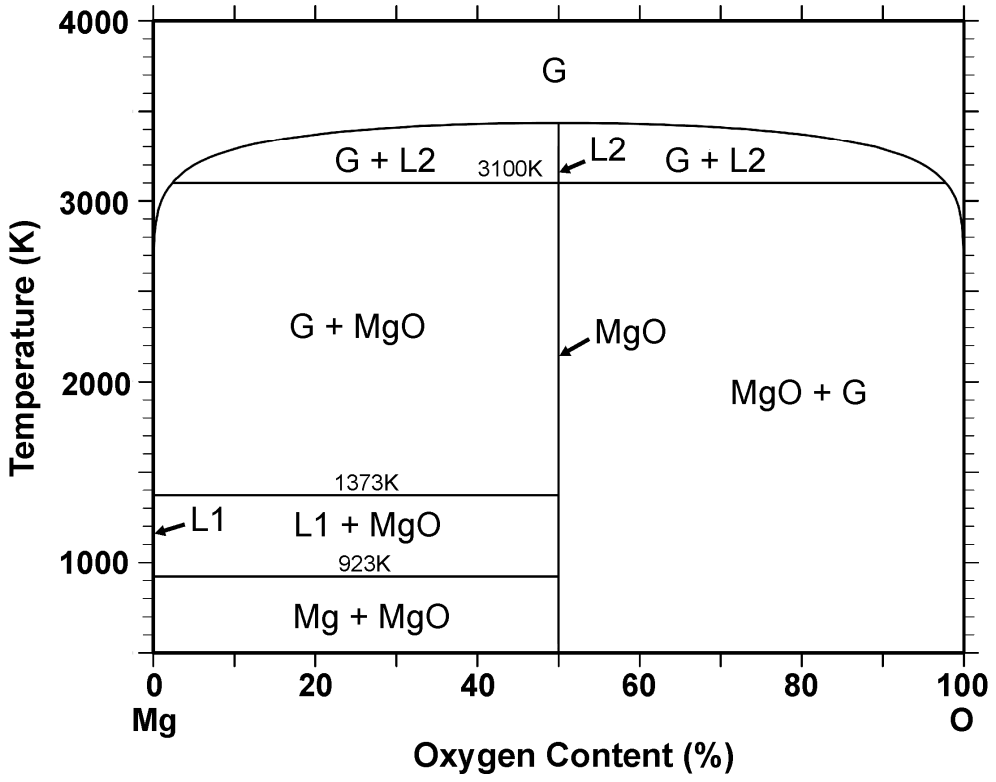

Figure 4.1: *Calculated phase diagram of the Mg-O system [164]. The pure magnesium has an hcp structure, a melting point at 923K, and a boiling point at 1373K. L1 assigns to liquid magnesium, L2 to liquid MgO, and G to the gas phase. The gas phase is assumed to consist of Mg, Mg_2, MgO, O, O_2 and O_3 species [166].*

Phase	Crystallographic Structure			Melting/Dissociation temperature (K)
	Type	a (Å)	c (Å)	
MgO	NaCl (B1)	4.213 ± 0.002	/	3100 melt.
MgO_2	FeS_2	4.844	/	373 dis.
MgO_4	hex	11.44	12.6	243 dis.

***Table 4.1**: The different magnesium oxide phases at atmospheric pressure [165,166,167,170]*

MgO is a highly ionic compound. The difference in electronegativity between the magnesium (1.32) and oxygen (3.44) atoms, as related to the electronic configurations of Mg($1s^2 2s^2 2p^6 3s^2$) and O($1s^2 2s^2 2p^4$), results in a strong ionic bound: The two electrons from the Mg 3s orbital are transfered to the O 2p one. The radii ratio between O^{2-} (1.26Å) and Mg^{2+} (0.86Å) ions favors the Mg^{2+} ions to be accommodated in an octahedral site between six O^{2-} ions, i.e., leading to their arrangement in a rocksalt (NaCl type) structure (figure 4.2). The rocksalt configuration allows an optimum interaction between the magnesium and oxygen ions, where every cation/anion is coordinated with six neighboring anions/cations.

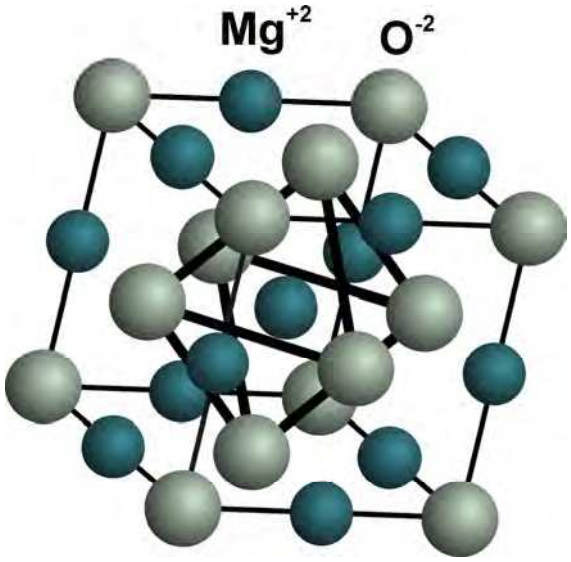

***Figure 4.2:** Crystallographic structure of bulk MgO. The interstitial octahedral sites of an fcc (face-centered cubic) network of O ions are occupied by Mg ions forming a rocksalt structure. The bold lines delimit the unit cell of the fcc structure. The center of the fcc unit cell constitutes an interstitial octahedral site.*

With a bulk bandgap of 7.9±0.7eV at 0K [171], the MgO is a very good insulator [21]. The low- and high-energy edges of the bandgap are dominated by the oxygen 2p and the magnesium 3s states, respectively. The analogue to the bandgap in electron excitation processes in MgO is the interatomic charge transfer energy, which locally transforms the bond Mg^{2+}–O^{2-} into Mg^{+}–O^{-} [21]. In figure 4.3, experimental as well as calculated energy diagrams of bulk MgO are presented.

As summarized in figure 4.3a, the MgO bandgap and the energy positions of the valence and the conduction band-edges can be derived from a simple ionic picture [172]. The model is mainly based on the calculation of the Madelung potential for each ion type with respect to the vacuum level. This calculation results in a bandgap of about 24eV, which is, however, far higher than the real value (7.9eV). The Madelung potential as defined in equation (4.1) describes the Coulomb force experienced by an Mg^{2+} or an O^{2-} ion due to the presence of all neighboring ions in a NaCl-type network.

$$E = -\frac{z^2 e^2 M}{4\pi\varepsilon_0 r_0} \tag{4.1}$$

where

$$M = \sum_i \pm \frac{r_0}{r_i} \tag{4.2}$$

thereby, z is the ion charge; e, the elementary charge; r_0, distance to the closest ion; M, the Madelung's constant; and r_i, distance to the i ion. For a NaCl-type structure $M \approx 1.74758$.

In the above estimation of the Madelung potential, the ions were taken as point charges, i.e., there is no spatial distribution of the charge within the ions. However, the charge distribution around each ion is delocalized and can be polarized with respect to a free ion, as a reaction to the electric fields of neighboring ions. This polarization of the charge cloud reduces the Coulomb forces compared to a point-charge field. As a result, the Madelung potential, and therefore the calculated bandgap, decreases. However, despite this correction, the experimental value of the MgO bandgap is still overestimated. A better approached is obtained when the effect of the overlap between the orbitals is taken into account (figure 4.3a) [172].

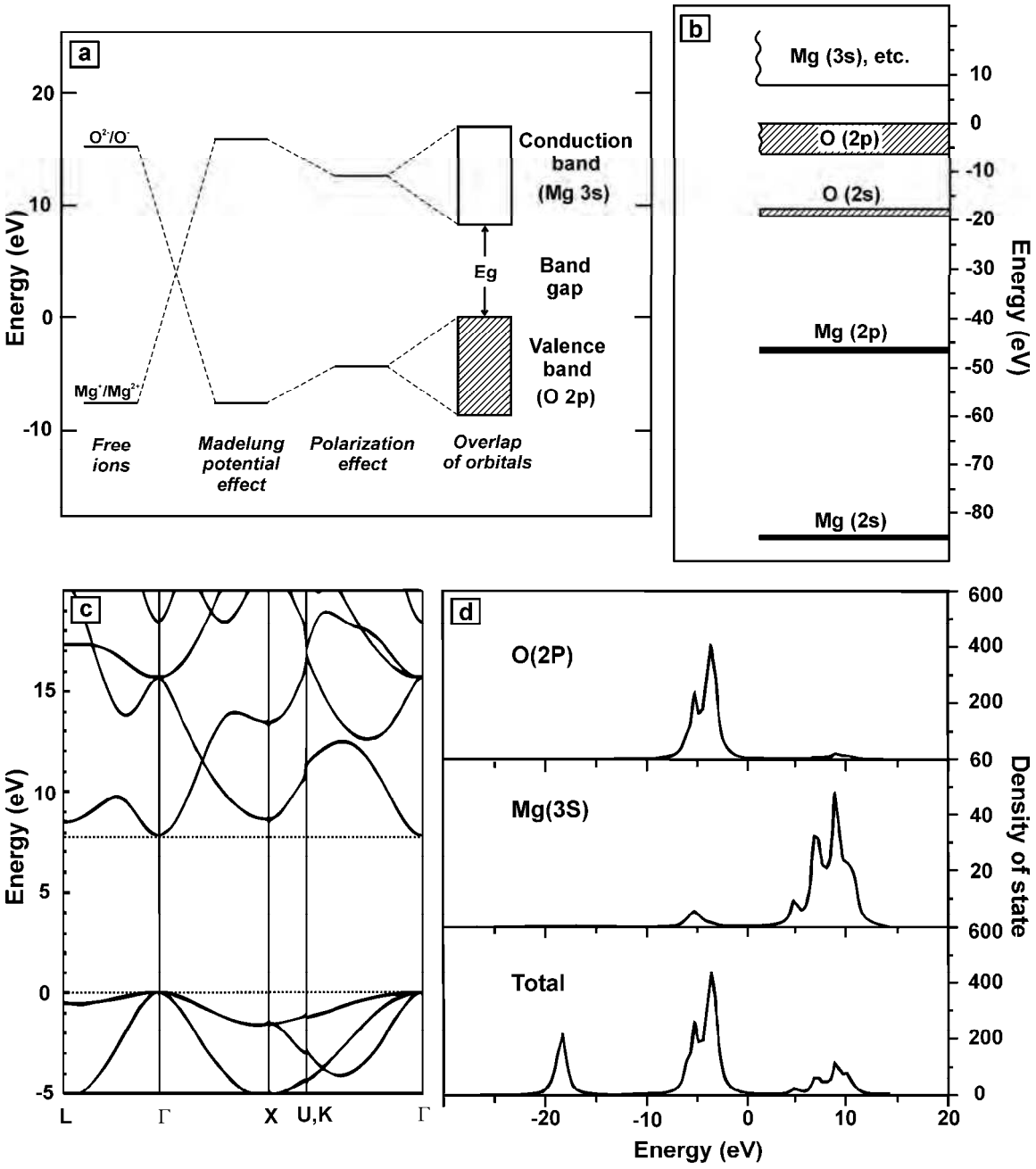

Figure 4.3: (a) *Derivation of the valence and conduction band energies in MgO [172]. In comparison with the original figure [172], the reference on the energy scale is shifted from the vacuum level to the valence band edge by about 7.8eV.* ***(b)*** *An approximate energy-level diagram of MgO based on XPS (X-ray Photoemission Spectroscopy) measurements [144].* ***(c)*** *Calculated band structure of bulk MgO along high symmetry lines in the Brillouin zone [173].* ***(d)*** *Calculated partial and total density of states of bulk MgO [174].*

Because of the high ionicity of MgO, there are strong Coulomb forces aiming to maintain local charge neutrality in the bulk and the surface. Therefore, the most stable surface is the non-polar surface, where each plane has zero net charge [60]. This is the case for the low index (001) surface. The (001) surface is charge neutral and has no net dipole moment in any direction, since it is atomically flat and contains an equal number of Mg and O ions. The ions of the (001) surface are fivefold coordinated (5C), which is lower than in the bulk (6C). Nevertheless, their oxidation state is found to be nearly the same as in the bulk, i.e., Mg^{2+} and O^{2-} [21,144]. However, the (001) surface is characterized by a decrease of the energy gap, which becomes 6.2eV [144,154]. This fact is attributed to a balance between a reduction of the Madelung potential near the surface, differences in the Mg^{2+}–O^{2-} charge transfer for surface and bulk ions, and the polarization of the wave functions of the surface ions towards the vacuum [144]. The (110) surface is charge neutral as well. It is constituted of alternating rows of magnesium and oxygen ions in the $[1\,\bar{1}\,0]$ direction. However, it is less stable than the (001) surface because the ions are only fourfold coordinated (4C) and because of existing dipole moment perpendicular to the atomic rows. The high stability of the (001) surface has been proven experimentally. Burning magnesium in air produces MgO smokes, which are small sized (<0.5μm) single-crystal cubes, exhibiting mainly {100} faces [175,176].

II. Morphology of MgO thin films on Mo(001)

II.1. MgO film preparation

Before MgO deposition, the Mo(001) single crystal is prepared by repeated cycles of annealing at 1300 K in an O_2 atmosphere and flashes to 2300K in UHV. This produces a sharp p(1x1) LEED pattern of the bcc Mo(001) and a surface with large terraces delimited by monatomic steps (figure 4.4). A clean Mo(001) surface can also be obtained by performing sputter – anneal cycles followed by flashes to 2300 K. However, while the first method of surface cleaning is found to be suitable when the Mo crystal is freshly introduced into the UHV, the second way is very efficient to take away deposited material and retrieve a clean Mo(001) surface. In the literature, epitaxial growth of MgO is realized over a wide range of oxygen pressures and substrate temperatures [177]. Epitaxial MgO films have been achieved using techniques such as pulsed-laser deposition [178], molecular beam epitaxy of evaporated MgO [179], and magnetron sputtering of MgO or Mg targets [180]. The growth from an Mg metal source is found to require low background pressure due to the strong affinity of Mg to oxygen [177].

In our experiment, MgO films with different thickness are grown at room temperature by reactive deposition of evaporated Mg in an O_2 partial pressure of 1×10^{-7}mbar. Magnesium is thereby evaporated from a crucible heated by electron bombardment (chap. 2, sect. III.2). After deposition, the sample is annealed for 10min at 1100K to improve the crystallinity of the film. The nominal thickness of the MgO film is defined as the product of the MgO deposition rate and exposure time. The deposition rate is determined from sub-monolayer film preparations, where the MgO coverage is directly deduced from STM images.

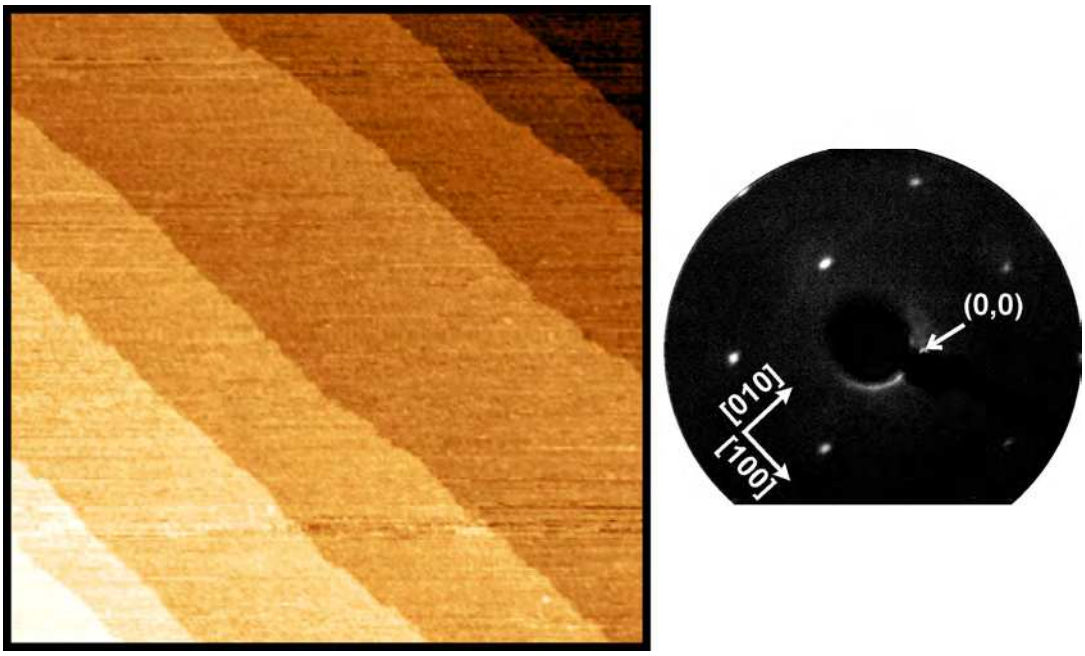

Figure 4.4: *250×250nm^2 STM topographic image of a clean Mo(001) surface and its corresponding LEED pattern (120eV) obtained after surface cleaning, as described in the text.*

II.2. Structural and topographical characterization

II.2.1. Results

Figure 4.5 shows a series of LEED patterns of MgO films with increasing thickness. In all cases, the patterns show broad spots having a square (1×1) structure, and a high spot intensity-to-background ratio. The (1×1) structure indicates the nearly-identical size of the primitive cells of the clean Mo substrate and the MgO film. This results from an epitaxial growth of MgO, where the MgO(001) plane grows parallel to the Mo(001) surface, and the MgO⟨110⟩

direction aligns with Mo⟨100⟩. Such an epitaxy is favoured by the small mismatch (5.3%) between the Mo-Mo (3.147 Å) and O-O (2.98 Å) distances in the (001) plane and along the Mo⟨100⟩ and MgO⟨110⟩ directions, respectively. For the sake of clarity, all crystallographic directions in the following paragraphs are given with respect to the MgO.

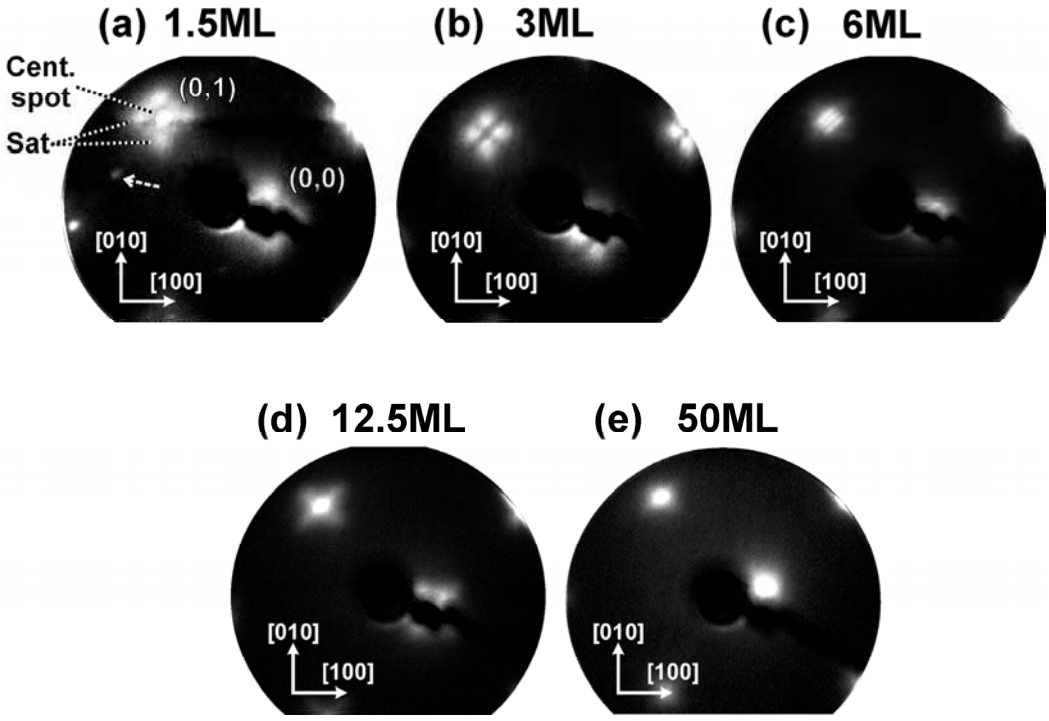

Figure 4.5: *LEED patterns of MgO films on Mo(001) for a primary electron energy E_p=55eV:* ***(a)*** *1.5ML,* ***(b)*** *3ML,****(c)*** *6ML,* ***(d)*** *12.5ML, and* ***(e)*** *50ML. The dotted white arrow in (a) marks a spot of a p(2x1) superstructure. The indicated crystallographic orientations are given with respect to the MgO.*

The structure change of the LEED spots as a function of the film thickness can be classified in three thickness regimes. The first range is between 0.85ML and 6ML. Here, the spots show an anisotropic broadening along the [100] direction due to the presence of satellites. The size of the fundamental spots decreases by almost a factor of three when increasing the film thickness from 1.5ML to 6ML. Besides, at low coverage (figure 4.5a) a p(2x1) superstructure is observed. This structure is tentatively attributed to the formation of an Mg-Mo interface-layer.

Additional observations are made on the spot characteristics when changing the electron beam energy (figure 4.6): (i) The distance of each satellite from the central spot stays unchanged on the LEED screen. (ii) The central spots of the reflexes appear or disappear depending on film thickness. (iii) When the film is around 3ML thick (figure 4.6a), distinct

additional satellites become visible along the ⟨110⟩ direction at high electron energy (140eV) that are inside the square formed by the ⟨100⟩ satellites. It has to be noticed that all the observed LEED spots follow the same described behavior, and the (0,1) spot, shown in figure 4.6, is only chosen for its clarity on the LEED images.

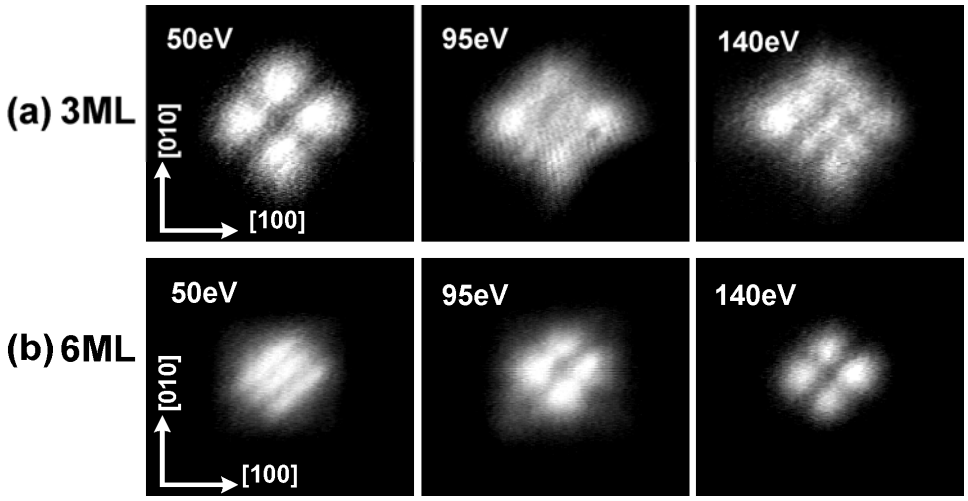

Figure 4.6: *Behavior of the (0,1) LEED spot as a function of electron primary energy from MgO films with* ***(a)*** *3ML and* ***(b)*** *6ML.*

A second category of the LEED spots starts to be observed when the film thickness reaches approximately 10ML. At this thickness, the size of the typical LEED spots seen for the thinner films becomes so small that the satellites become undistinguishable from the central spot. On the other hand, an anisotropic broadening of the spots start to appear along the ⟨110⟩ direction. The broadening evolves to clear shoulders for thicknesses around 12ML (figure 4.5d). With further increasing of the thickness, the shoulders move towards the central spot and finally disappear at around 23ML. Neither the shoulder to central spot distance, nor the structure of the reflexes –unlike for thinner films– is affected by the variation of the LEED electron energy. Finally, for films consisting of more than 23 layers a sharp (1x1) pattern appears in LEED, indicating a flat and defect-poor surface structure (figure 4.5e).

The STM analysis of the evolution of the MgO film morphology as a function of coverage revealed a rich behavior. This evolution is summarized in figure 4.7, where topographic STM images of six typical film morphologies are presented. Figure 4.7a shows that a film with a coverage of 0.85ML exhibit squared islands of different lateral sizes and shapes and with edges oriented along the ⟨100⟩ direction. With increasing the coverage by about a factor of two, the film morphology changes from an island-like configuration to a more or less closed film exhibiting few rectangular holes. The holes are confined by non-polar

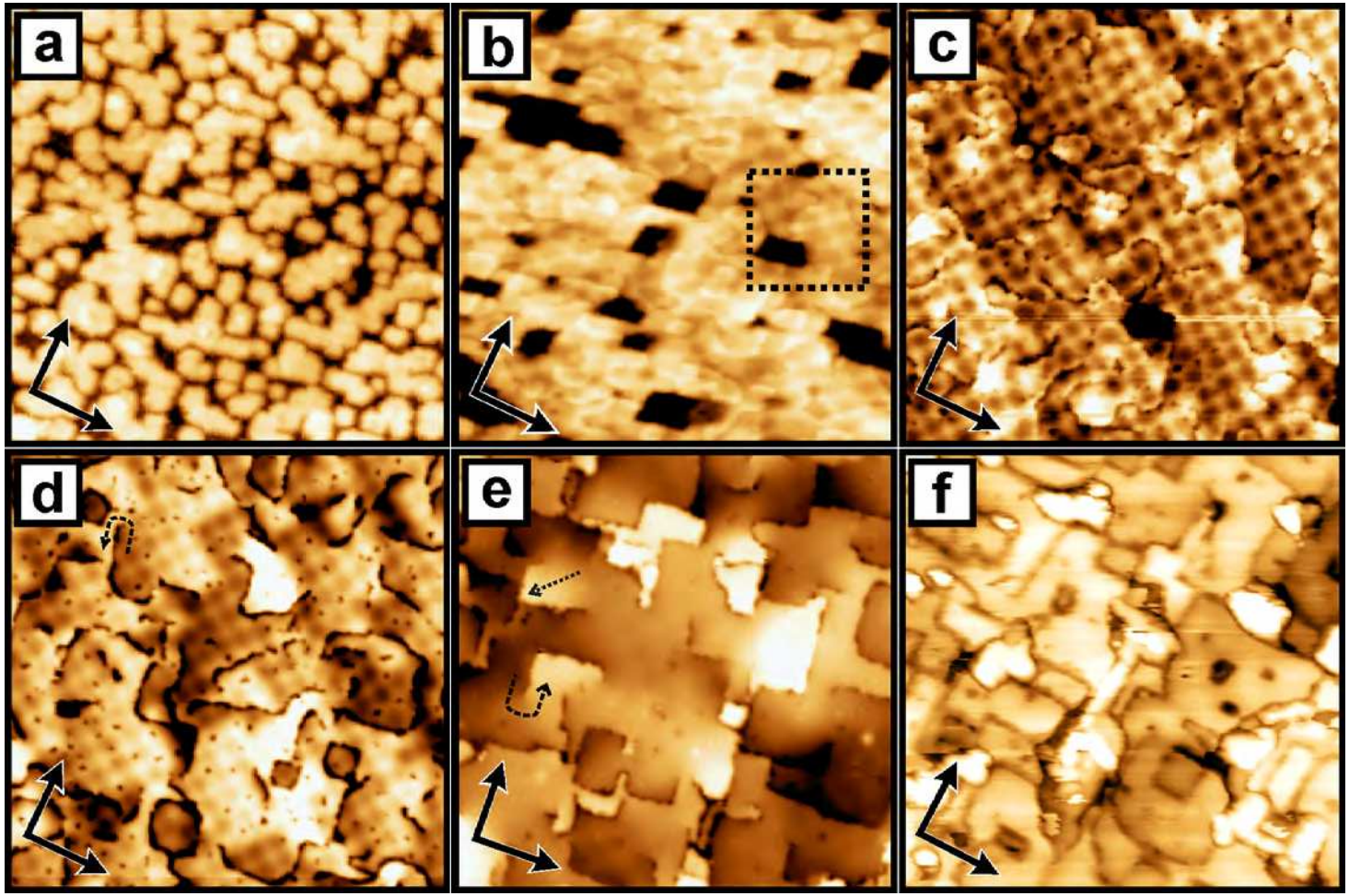

***Figure 4.7**: 100×100 nm^2 STM images elucidating the evolution of the morphology of deposited MgO thin films on Mo(001) as a function of coverage. **(a)** 0.85 ML (I = 0.05nA, U = 2.7V). **(b)** 1.75 ML MgO (I = 0.06 nA, U = 3.0V). A zoom of the dashed square is presented in figure 4.8 . **(c)** 3.75 ML MgO (I =1.26 nA, U = 3.5V). **(d)** 6 ML (I = 2.0nA, U = 3.6V. **(e)** 70×70 nm^2, 12.5ML (I = 0.6nA, U = 4.8V). **(f)** 30ML (I = 0.15nA, U = 12.5V). Annealing temperature: (a) 1000K, (b)– (f)1100K. The dashed and the dotted arrows indicate screw dislocations and a tilted region, respectively. The bold solid arrows indicate the MgO⟨100⟩ direction.*

⟨100⟩ edges (figure 4.7b). In addition, a checkerboard pattern formed of bright and dark rectangles with a periodicity of approximately 80Å along MgO⟨100⟩ (or 55Å along MgO⟨110⟩) is discernable on the film. The sides of the checkerboard pattern are oriented parallel to the ⟨100⟩ directions (figure 4.7b). For MgO coverage of around 4ML, a regular square pattern aligned with the ⟨110⟩ direction, and with the same size as the checkerboard structure, becomes visible on the almost closed film (figure 4.7c). Figure 4.8 illustrates a local transition from the checkerboard structure to the square pattern after an increase of the MgO thickness by 1ML. The visibility of the square structure is apparently enhanced by an electronic effect, as large topographic contrast is only obtained for sample voltages around 3.5V. The images of 4ML thick films also reveal the presence of irregularly oriented defect lines between large islands of the film (the dark lines in the image). These lines are named in the next paragraphs as domain boundaries. The 6ML film exhibit the same square network as observed at 4ML, however, here the contrast between the bright and the dark areas forming the network is less pronounced even at optimum scanning conditions (figure 4.7d). At this coverage, the film is completely closed and free of uncovered areas. Furthermore, unlike for the 4ML films, most of the present dislocation lines align along the ⟨100⟩ directions. In addition, screw dislocations are observed at some parts of the film (dashed arrow in figure 4.7d). The periodic structures seen from 1ML to 6ML thickness are found to be perturbed and discontinuous when going from an island to another across the domain boundaries.

The next typical morphology of the MgO film is observed for coverages around 12ML (figure 4.7e). Here, the square pattern is not distinguishable anymore, apart from few exceptions when it faintly appeared. The defect concentration decreases dramatically and the domain boundaries are now all oriented along the ⟨100⟩ directions. Particularly, screw dislocations are recognized at almost every starting point of a defect line (see dashed arrow in figure 4.7e). This is accompanied by a clear tilting of corner regions along the ⟨110⟩ directions. Above 12 ML film thickness, the oxide gradually starts to flatten and the global roughness starts to decrease. The STM image of a 30ML thick film (Figure 4.7f) shows rather flat area separated by trenches oriented along the ⟨100⟩ directions. However, due to the vanishing conductivity of the thick oxide films, STM experiments are rather difficult and are performed at high sample bias, where electrons are injected ballistically into the MgO conduction band and propagate in the tip-induced electric field towards the Mo support.

According to the STM observations, the growth of the MgO film undergoes the following steps: (1) Nucleation of MgO islands; (2) closing of the film and formation of a wetting layer; and (3) growth following a layer-by-layer-like fashion. It has to be noticed, however, that the layer by layer growth is not perfect. Some lower planes remain incomplete although the next layer starts to nucleate already (figure 4.9).

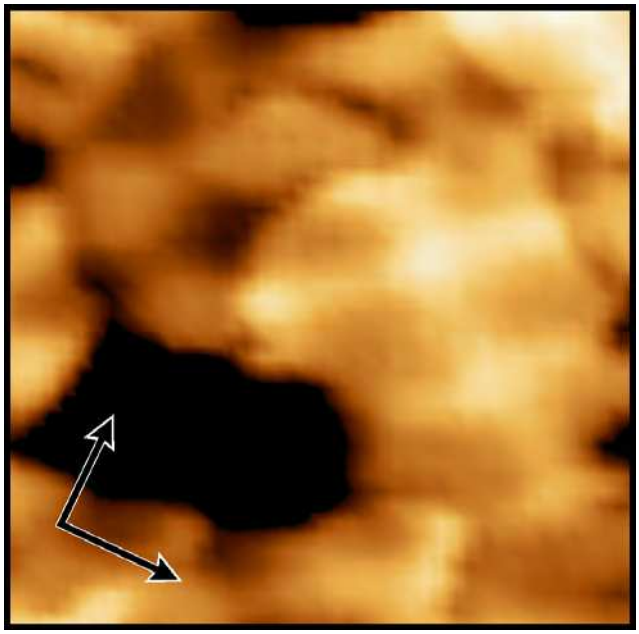

Figure 4.8: *19×19nm^2 zoom of the indicated area in figure 4.7. The figure shows a part of a 1.75ML MgO film. It illustrates the local transition from a checkerboard-like to a square network for an increase of the local thickness by 1ML. The perpendicular arrows indicate the MgO⟨100⟩ directions.*

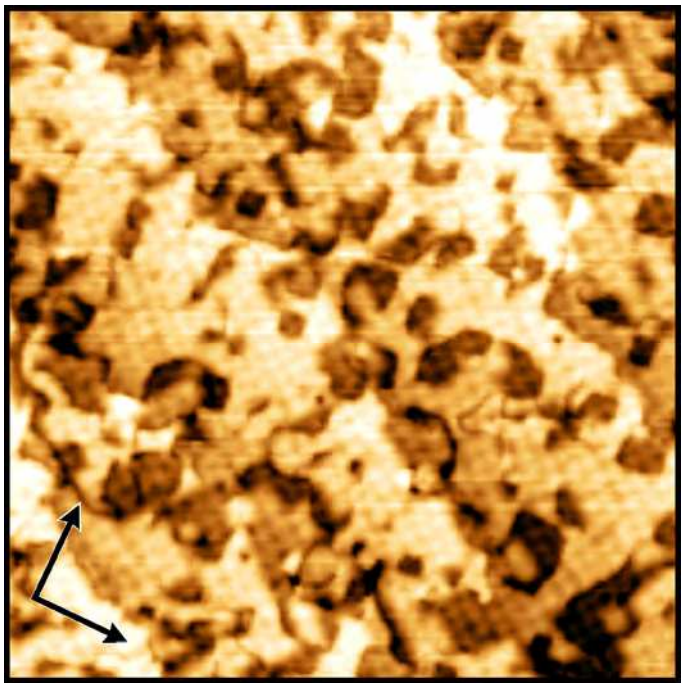

Figure 4.9: *180×180nm^2 STM topographic image of a Mo(001) substrate covered with 6ML of MgO, (I = 0.4nA, U = 3.7V).*

In order to obtain more details on the evolution of the MgO film structure as a function of thickness, we have performed Grazing Incidence X-ray Diffraction (GIXD) analysis[4] on the MgO/Mo(001) system. Figure 4.10 shows a series of GIXD curves recorded for several MgO films having different thickness. The GIXD measurements have been performed using a photon energy of 18keV. The incidence angle was 0.166° with respect to the sample surface. The GIXD data provide a quantitative description of the relaxation of the MgO lattice parameter with film thickness (figure 4.10b). Already at 1ML MgO, the lattice parameter is found to be larger only by ≈1.6% (smaller by ≈3.7%) than the bulk MgO (Mo) parameter. The lattice then relaxes rapidly towards the bulk MgO the lattice constant with increasing the thickness from 2ML to 7ML. Between 15ML and 25ML the relaxation proceeds slower. At 25ML the MgO lattice parameter is still not completely relaxed, since it remains around 0.5% larger than for bulk MgO (figure 4.10b). Furthermore, a satellite peak appears on the GIXD curves between the MgO and the Mo Bragg peaks (figure 4.10a), denoting the presence of a periodic structure of the same period as the Moiré structure of the MgO(001)/Mo(001) system.

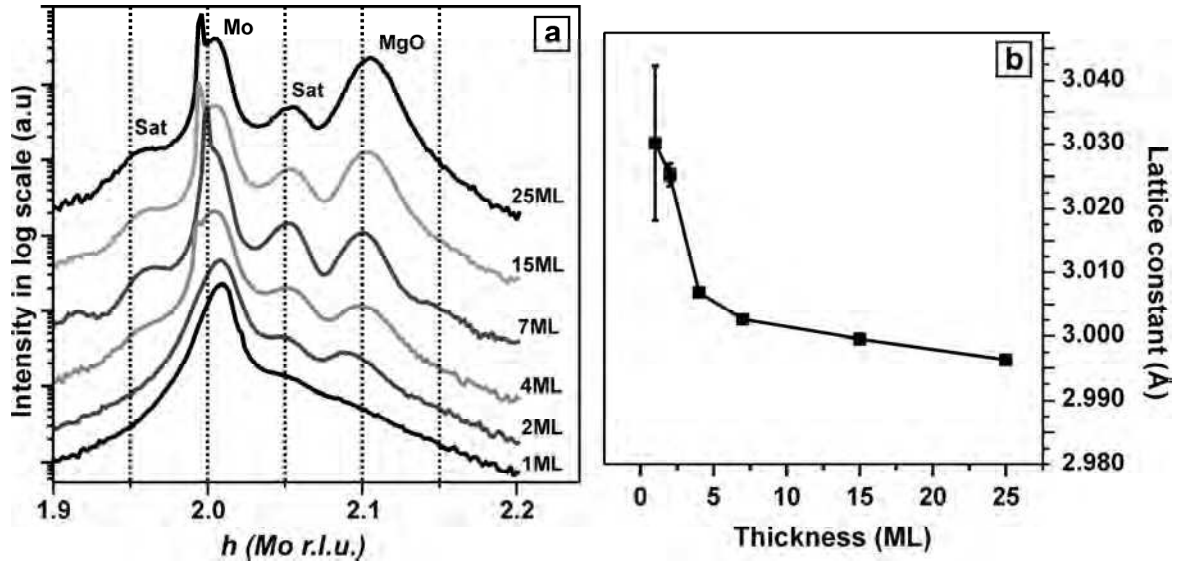

Figure 4.10: (a) *GIXD spectra of MgO/Mo(001) thin films with increasing thickness. The spectra represent radial scans along the (h,0,0.03) direction around the (200) molybdenum Bragg peak (r.l.u. states for reciprocal lattice units). The satellites indicate the presence of a periodic structure of the same size as the one observed with STM.* ***(b)*** *Evolution of the MgO lattice constant along the MgO⟨100⟩ direction with film thickness. The lattice constant is extracted by fittings of the Mo and the MgO peaks with Gaussian curve.*

[4] The GIXD experiments were done at the ESRF in Grenoble at the beamline BM32, in collaboration with the groups of Prof. S. Valeri (University of Modena-Italy) and Prof. G. Renaud (ESRF, Grenoble-France).

II.2.2. Discussion

Schematic superposition of a MgO(001) layer (a = 4.213Å) on top of a Mo(001) surface (a = 3.147Å) with MgO⟨100⟩//Mo⟨110⟩ results in a square coincidence structure, a so-called Moiré pattern. In this structure, the oxygen atoms of the MgO layer and the Mo atoms sit on top of each other every 19 oxygen or 18 Mo atoms according to the 5.3% lattice mismatch (figure 4.11). Thus, the Moiré pattern has a periodicity equal to 19×4.213Å = 18×4.45Å ≅ 80Å along the MgO⟨100⟩ direction or equal to 19×2.98Å = 18×3.147Å ≅ 56.6Å along MgO⟨110⟩.

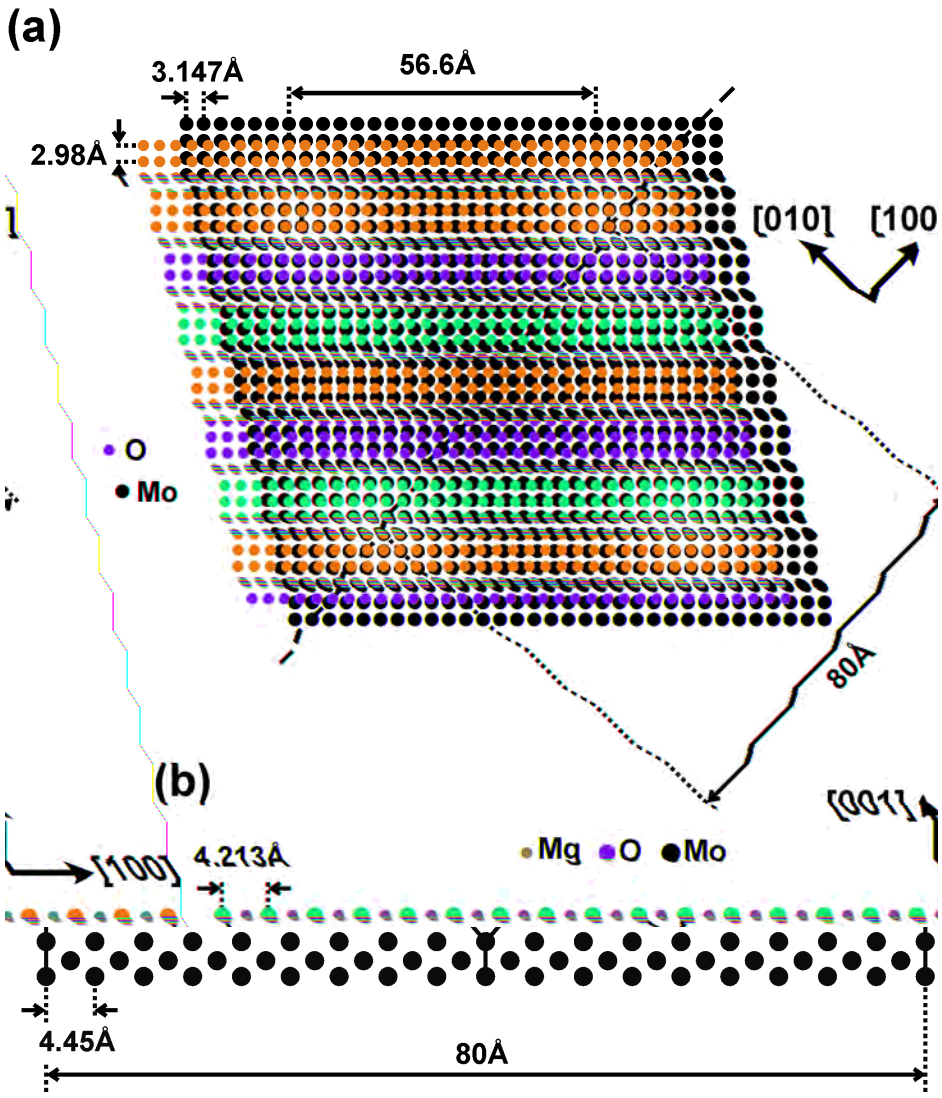

Figure 4.11: *Atomic representation of a MgO(001) layer with the bulk lattice parameter on top of a Mo(001) substrate.* ***(a)*** *A top view,* ***(b)*** *a cross section view along the (100) plane (dashed line in (a)). The atomic periodicity of the surface is modulated by a larger periodicity of 80Å along the ⟨100⟩ direction corresponding to the Moiré pattern. The Mg atoms are hidden in (a) in order to increase the contrast of the Moiré structure.*

In a LEED analysis, a Moiré pattern would result in additional diffraction spots, or satellites, around the main MgO and Mo reflexes [181]. The positions of these spots on the LEED screen follow the same energy-dependence as the main spots, whereby the distance ratio between the (0,0) to (0,1) and (0,0) to the Moiré spot remains constant with energy. In other words, the Moiré LEED spots have a constant position in the surface Brillouin zone as a function of the LEED primary energy. However, in our analysis, the LEED satellites of the MgO film in the thickness regime between 0.85ML to 23ML do not follow the expected behavior of a Moiré pattern. Indeed, the satellite positions move inside the Brillouin zone and depend linearly on the primary electron energy, as shown in figure 4.12. This behavior is typical when the film comprises tilted mosaics [182]. Thus, the prepared MgO films with coverages smaller than 23ML contain mosaics tilted along the ⟨100⟩ for 1ML to 10ML and along the ⟨110⟩ direction for 10ML to 23ML thickness (figure 4.12). The tilting angles are easily extracted from the variation of the satellite spot position in the Brillouin zone with respect to the corresponding LEED energy ($\Leftrightarrow tan\,\alpha = \Delta K_{//} / \Delta K_{\perp}$, α the tilting angle). The extracted tilting angles for the different film thicknesses are indicated on figure 4.12. The calculation of α is done by considering the Brillouin zone of the reciprocal lattice of the Mo(001) surface.

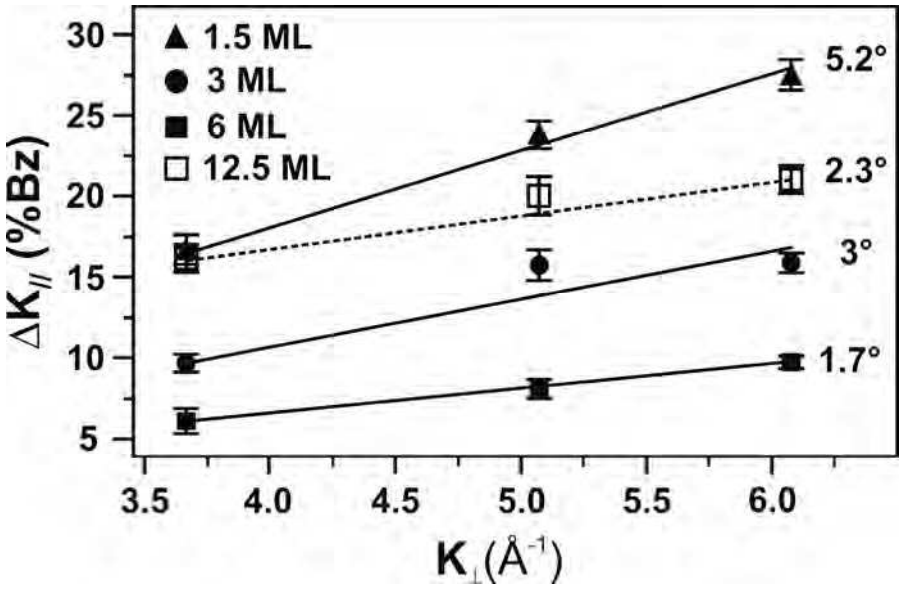

Figure 4.12: *Measured positions of the satellites of the (0,1) LEED spot with respect to the Brillouin zone shown as a function of the Ewald's sphere radius ($K_{\perp} = \sqrt{2mE}/\hbar$, E: LEED primary electron energy). The considered satellites are those along the ⟨100⟩ direction for a MgO coverage of 1.5ML, 3ML, and 6ML, and the ones along ⟨110⟩ for a 12.5ML film. The lines are linear fits to the data and yield the tilting angles with respect to a flat (001) surface.*

Similar LEED patterns were reported earlier for MgO/Ag(100) [183] and MgO/Fe(100) [184] and were assigned to the formation of tilted mosaics as well. The tilted mosaics form between a dislocation network in order to release the stress induced by the lattice mismatch. This mechanism to release the misfit-induced stress is not only observed for MgO thin films, but a general phenomenon of thin epitaxial films [185,186,187]. With the STM, the presence of tilted regions in the MgO films is verified only for coverages higher than 10ML (figure 4.7e). The measured tilting angles from STM images of a 12.5ML thick film range from 1.7° to 2.7°, which is in a good agreement with the results obtained by the LEED. For example, the tilted plane indicated in figure 4.7e is inclined by about 1.9°, since its corner is 0.4nm higher than the point where it starts to be flat being 12nm away. Besides, the tilting angle along the MgO⟨100⟩ and along the MgO⟨110⟩ is found to decrease with increasing MgO film thickness from 0.85ML to 6ML and from 10ML to 23ML, respectively (figure 4.12). This observation is also noticed in references [182-185]. The flattening of the tilted mosaics with increasing coverage is attributed to the weakening of the strain field with the distance from the interface where the strain is generated [184]. Hence, the MgO film on the Mo(001) gradually relaxes with thickness. This conclusion is validated by the obtained GIXD data (figure 4.10b).

STM imaging of a Moiré structure, as shown in figure 4.11, would result in alternating bright and dark areas having the same periodicity as the Moiré unit cell [77,71]. However, even if such a periodic structure is observed in the STM images (Figures 4.7b,c,d), it cannot be easily related to the simplified Moiré model. The Moiré presented in figure 4.11 results from a coincidence between a MgO layer having the bulk lattice parameter and the Mo substrate. Yet, it is found that the first MgO layers do not have a bulk lattice constant (figure 4.10b). The MgO bulk lattice parameter is reached only for coverages higher than 15ML. So, the observed periodic network in the thin MgO films has to be explained by a more refined model. It is rather interpreted as periodic domains induced by a regular distribution of the strain fields, which are generated by the lattice mismatch. To describe this distribution, a structure model is needed. We propose in figure 4.13 a model, which schematizes the relaxation of the MgO film for thicknesses between 1ML and 4ML. As a first approximation, the mismatch in the thermal expansion coefficients between the Mo and the MgO, and the elastic properties of the Mo are ignored. Also, it is supposed that the Mo structure at the interface stays unchanged and all deformations induced by the strain occur in the MgO film. The model is based on a strain balance, in every unit cell of the network, between: (i) A strain driven by the Mo affinity to oxygen which tends to induce a pseudomorphic growth of MgO (18 MgO over 18 Mo cells). (ii) A counter strain exerted by the intrinsic Mg-O bonds to have the bulk binding distance and construct 19 MgO over 18 Mo cells. By considering the scheme in figure 4.11, the one or the other strain type dominates, depending on the relative position of

the O atoms with respect to the Mo ones. Thus, when the O atoms are at the atop sites, the bonding to the Mo is high. This results in a reduced Mo-MgO separation distance and a stretched MgO lattice. In the opposite, at the hollow site regions, the bonding to the substrate is weaker. Therefore, the Mo-MgO separation is slightly bigger and the Mg-O bond length is shorter than at the atop sites. Such a dependence of the interfacial distance between an epitaxial film and the substrate on the registry between film and support atoms has been already discussed for NaCl/Ag(001) [71] and Pd/MgO(001) [188] systems.

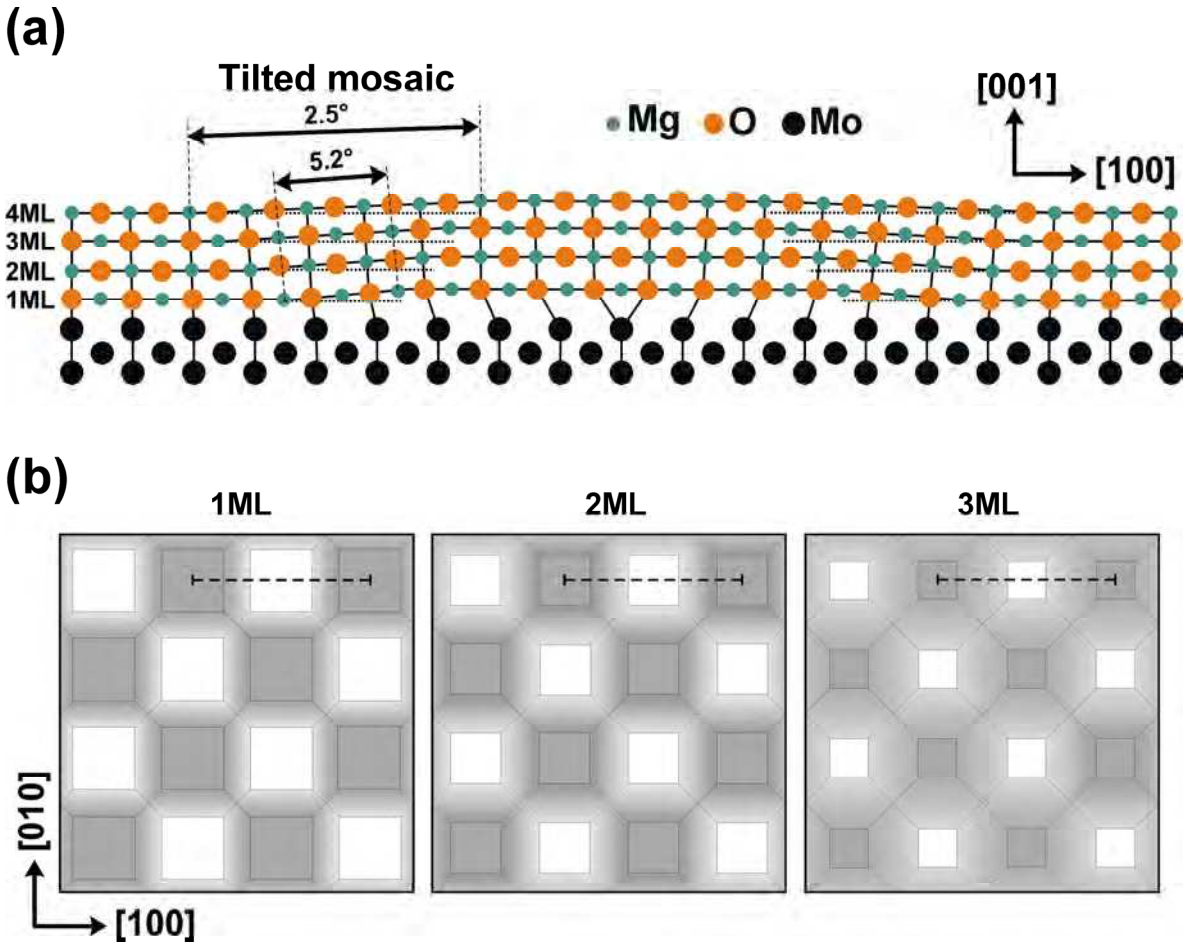

Figure 4.13: *Schematic description of the relaxation in MgO/Mo(001) thin films as a function of the thickness. The relaxed MgO films are formed of alternating high and low flat areas, with a periodicity of 80Å along the ⟨100⟩ directions, separated by tilted regions (mosaics). With increasing film thickness, the mosaics decrease in inclination and increase in size.* ***(a)*** *Atomic representation of the cross section view along the 80Å long dashed line in (b).* ***(b)*** *Top view depictions of an 160×160Å^2 area of 1ML, 2ML and 3ML films.*

The intermediate regions between the hollow and atop sites are now subject to tilting with respect to (001) plane as a result of the changed interface distance between atop and hollow sites. Also, these regions experience an in-plane strain caused by the enlarged Mg-O bond distance in the atop regions, which compresses the hollow areas. Thus, the tilting might increase to release this stress. This induces a further lengthening of the MgO-Mo separation in the hollow region. The weaker MgO adhesion to the Mo in the hollow regions with respect to the atop ones therefore results in high and low areas corresponding to hollow and atop regions, respectively. These areas are separated by tilted planes (figure 4.13).

The tilt is considered to be only along the ⟨100⟩ directions, as the LEED measurements imply it for thinner films (figure 4.12). Nevertheless, this preferential tilt orientation can have as origin the elastic anisotropy of the MgO. The Young's modulus[5] of bulk MgO along the ⟨100⟩ direction is 27% and 40% lower than along ⟨110⟩ and ⟨111⟩ directions, respectively [189]. Accordingly, an anisotropic stress relaxation is more likely to happen. The relaxation then occurs along the <100> directions where the MgO film has the smallest stiffness. Considering only tilted areas along the <100> directions leads to square shaping of the high and the low areas, as observed in STM and shown in figure 4.13b.

The experimentally observed decrease of the tilting angle with film thickness (0.85ML to 6ML) is also pointed out in the model (figure 4.13). We presume that the weakening of the strain with increasing film thickness induces the flattening of tilted mosaics, which is accompanied by an adaptation of the lattice parameter in atop and hollow regions [184]. This results in a continuous increase of the lateral size of the tilted mosaics while they flatten until a complete flattening of the whole film surface. The relaxation model presented above (figure 4.13a) is also in accordance with the measured tilt angles from LEED (figure 4.12). For 1ML thick films, the tilt of 5.2° involves a mosaic of 10.52Å (two and a half MgO unit cells). This results in a height difference of 0.95Å between the atop and the hollow areas. Besides, this height difference could also induce a variation of the work function between the two areas [71]. This could be responsible for the enhanced STM topographic contrast observed at a certain sample bias (sect. II.2.1). As the positions of the field emission resonances (FER) depend on the sample work function (chap. 1, sect. II.3), a resonant state on top of one of the two areas could be hit at this bias[6], which then provokes an increase of the STM-junction conductivity. In addition, the difference in the real topographic height, out of FER conditions, is possibly enhanced by the difference in the electronic distribution in the two areas.

[5] MgO Young's modulus is equal to 248.17GPa, 316.36GPa, and 348.92GPa along the <100>, <110>, and <111> directions, respectively [189]. GPa for Gigapascal.

[6] More likely, the resonance is reached in the high regions; otherwise, the topography contrast would have been compensated.

Figure 4.13b presents top views of the MgO film for thicknesses of 1ML, 2ML, and 3ML according to the relaxation model. It also aims to give a better understanding of the STM topographic images taken for approximately the same thicknesses. A simple simulation of the STM image of figure 4.8, using the 1ML and the 2ML top view images of figure 4.13b, is shown in figure 4.14. A better modeling of the MgO surface than in figure 4.14b would require the consideration of the electronic structure of the oxide surface and the bias dependence of the contrast.

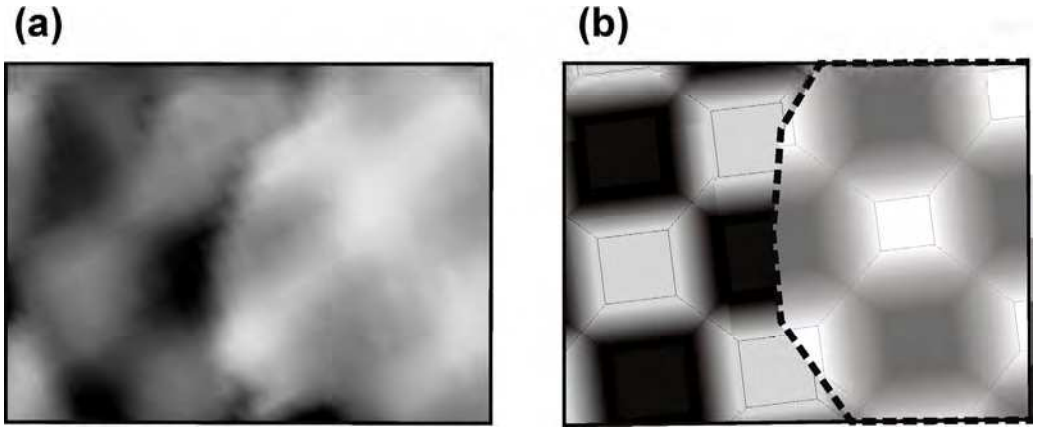

Figure 4.14: (a) *An enlarged area from the STM image in figure 4.8 presenting the coexistence of the checkerboard-like (left) and the square-like (right) structures.* ***(b)*** *Simulation of the structures in (a) by using the 1ML and the 2ML images of figure 4.13b.*

For the sub-monolayer films, the superstructure periodicity was not observed on the STM images (figure 4.7a), since the average terrace width of the formed MgO islands is smaller than the superstructure period. On the other hand, it is remarked that the maximum lateral size of the small square-shaped islands is around 40Å×40Å. Yet, this is the size of a square area of the checkerboard superstructure without tilted mosaics around it. Therefore, this size maximum reflects the size limit of MgO pseudomorphic growth on the Mo substrate. The ⟨100⟩ oriented edges of these islands reflect the dominance of non-polar step edges [21].

After the identification of the stress release in the MgO/Mo(001) films for low coverages (1ML to 6ML), the stress relaxation for a further increase of the thickness can be understood as follows. The top layers of thicker films are getting flatter and flatter and the stress-induced periodic structure will always be located at the first interface layers. This explains why the periodic structure remains visible in the GIXD analysis for all coverages (figure 4.10), thanks

to the large penetration depth of the X-ray radiation. With the STM, the periodic structure was barely seen at coverage of 12.5ML. In addition, the screw dislocations, which start to be observed at around 6ML coverage and became clear for the 12.5ML thick films (figure 4.7), are rather interpreted as being the result of the accommodation of phase-misfit between merging strain-relaxed MgO islands having different superstructure phases [190]. The accommodation of the phase-misfit takes also place in the thinner films (1ML to 6ML), but in a different manner. As they are characterized by a smaller stiffness than the thick ones [191], the merging thin islands are able to relieve the misfit from the border side into the volume. This may explain the observed perturbation of the periodic superstructure in the STM images across the domain boundaries (figures 4.7c and d). As the stiffness increases, the relaxation of the misfit between the islands is more and more concentrated around the domain boundaries, and the screw dislocations are more probable to appear. The stiffness behavior is also reflected by the random alignment of the domain boundaries along non-polar and polar directions in the thinner films (1ML to 4ML). The existence of polar edges can also be favored by a stabilization role played by the metal support [192]. The stiffness increase and the decoupling from the metal substrate, which become more efficient with the film thickness, force the edges of the domain boundaries to orient along the non-polar directions, which are the ⟨100⟩ (figures 4.7d and 4.7e).

The above interpretation of the strain relaxation behavior of the MgO/Mo(001) films should be, in the future, checked by an experimental investigation of the elastic properties of the films and by a suitable theoretical treatment.

In the next paragraph, the LEED pattern behavior shown in figure 4.6 is discussed in the light of the relaxation model presented above.

Figure 4.15 shows a two-dimensional fast Fourier transformation (2D-FFT) of an ordered network of points on the top of which a checkerboard pattern is superimposed. The orientation and the periodicity of the model structures in figure 4.15a correspond to the atomic configuration of an MgO monolayer and the strain-induced periodic superstructure, as presented in figure 4.13. The 2D-FFT picture (figure 4.15b) simulates the LEED pattern from the proposed relaxation model, without taking into account the 3D character of the surface.

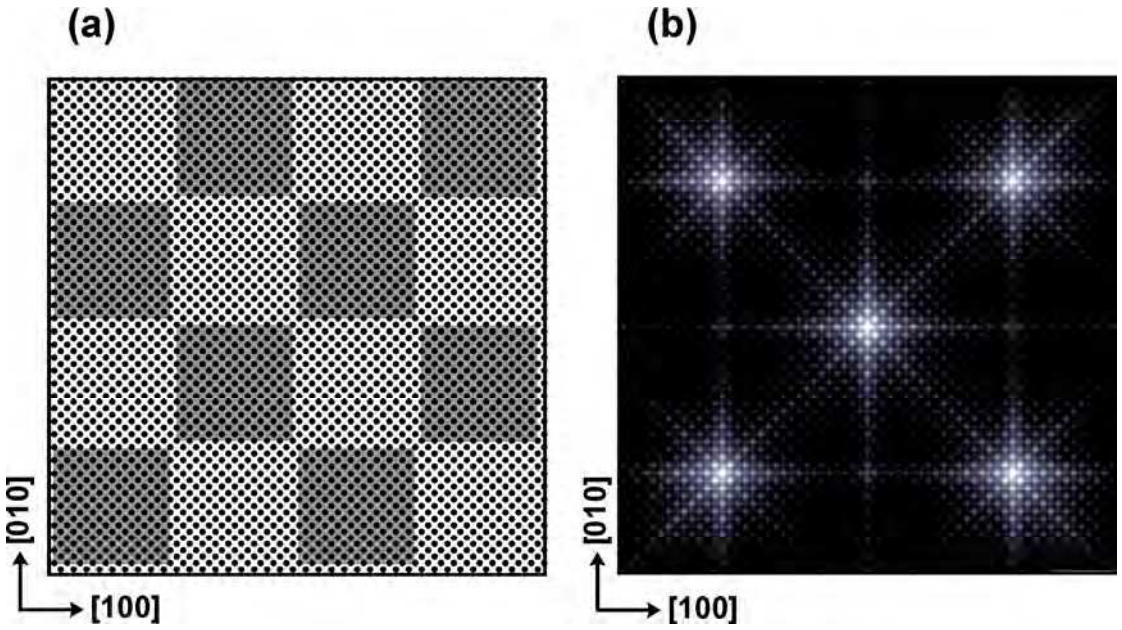

Figure 4.15: (a) *Outline representation of the atomic and strain-induced structures in a 1ML thick MgO film according to the relaxation model.* ***(b)*** *2D-FFT of image (a). Figure (b) represents a LEED simulation of (a).*

At the first glance, the superstructure periodicity present on the FFT image seems to do not exist on the recorded LEED patterns of figure 4.6. This would mean that the periodic network observed on the STM images at low coverages, as well as from GIXD measurements, does not produce any structure in LEED. However, a careful examination of the LEED patterns challenges this statement. A superposition of a point array corresponding to the superstructure periodicity on the experimental LEED pattern reveals that every LEED reflex might be formed by a number of superstructure spots (figure 4.16). The remark is valid for the LEED patterns with different primary energies and from different MgO thicknesses (figure 4.16). So, the periodic network observed on the STM images at low coverage contributes to the LEED pattern. Nevertheless, despite the concordance of the last conclusion, two phenomena, which depend on the film thickness and LEED energy, still need to be clarified: (i) The unexpected presence of superstructure spots with high diffraction-order (up to the 3rd order with respect to the main reflexes), figure 4.16c. Generally, the convolution between the diffraction intensity due to an atomic arrangement and a superstructure (like in figure 4.15a) makes only the two first orders of the superstructure appearing on the LEED screen [193]. (ii) The absence/presence of some superstructure spots along the ⟨110⟩ directions.

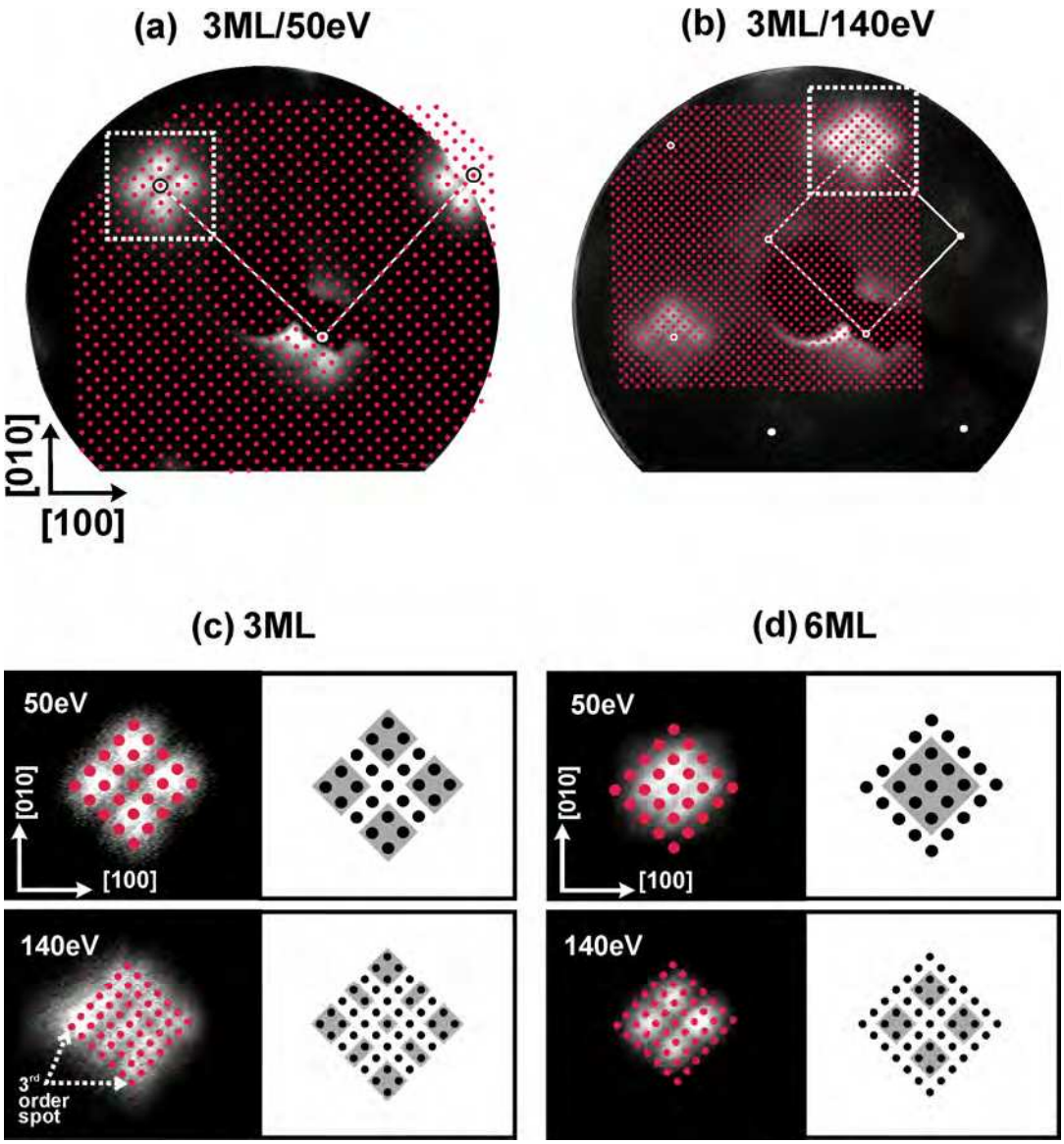

Figure 4.16: (a) *and* ***(b)****, superposition of a periodic structure on top of the LEED patterns of a 3ML thick MgO/Mo(001) film taken at (a) 50eV and (b) 140eV electron energy. The superposed structure has the same periodicity and the orientation of the strain-induced checkerboard-like structure (figure 4.13). The white straight lines delimit the surface Brillouin zone.* ***(c)*** *On the left side, zooms into the areas framed with white dotted lines in (a) and (b). For the sake of clarity, schematic reproductions of the zoom-figures are presented on the right side. The gray regions represent the illuminated areas in LEED.* ***(d)*** *Similar treatment of (c) made on the LEED patterns of a 6ML MgO/Mo(001) film. The identical shape of the spot profiles of the 3ML film at 50eV and of the 6ML film at 140eV indicates alike scattering conditions. The maximum order of diffraction spots due to the superstructure increases with LEED energy and decreases with film thickness.*

The first fact can be understood by considering the presence of tilted mosaics. As discussed above, these mosaics generate diffraction satellites at fix positions on the LEED screen for different LEED energies (figures 4.6 and 4.12). Thus, more high-order LEED spots of the superstructure might be fed by the intensity of the satellites with increasing energy. Furthermore, since the satellite positions move towards the fundamental spots with increasing film thickness (figure 4.12), the maximum order of the observed diffraction spots becomes lower for thicker films.

The second phenomenon is rather complex and is still under investigation. However, it may be understood as follows: The appearance and disappearance of LEED spots with varying the primary energy could be due to the known variation of the LEED spot intensities versus incident electron energy (so-called $I(V)$ curve), as induced by single and multiple electronic scattering in the film [194]. In this case, the $I(V)$ curve of an MgO film modulated by the strain-induced superstructure has to be calculated and compared to the experience. On the other hand, when only the single scattering of the electrons is considered, the presence of a regular height variation on the surface induces in-phase and out-of-phase interferences of the scattered electrons at different energies [193]. In the out-of-phase conditions, every fundamental spot splits into two spots along each direction of height variation (figure 4.17). Hence, according to the relaxation model (figure 4.13), the periodic distribution of high and low areas along the ⟨100⟩ directions in the MgO thin films would lead to the splitting of every fundamental LEED spot into four spots (two spots along the [100] and two others along the [010]) at the out-of-phase condition. So, if we consider the (0,1) spot of the LEED pattern from a 3ML MgO film (figure 4.16), then the missing central intensity at 50eV might be related to an out-of-phase scattering of the electrons. The in-phase condition could now be reached at 140eV, when the central intensity appears. The in-phase and the out-of-phase conditions correspond to scattering phases[7] $S = n$ and $S = n \pm 1/2$ (n: integer), respectively. Taking $S = 1/2$ for 50eV and $S = 1$ for 140eV results in a height difference of about 1Å. In other words, the average height difference between the low and the high areas in the 3ML MgO film is 1Å. Performing the same height calculation for the 6ML film, and taking $S = 1/2$ for 140eV, gives an average height difference of about 0.5Å. Theses heights are in a good agreement with the proposed relaxation model (figure 4.13).

[7] $S = d \cdot K_{\perp}/2\pi$, d regular distance between the atomic planes, $K_{\perp}$ perpendicular momentum of the electrons. In the actual case, d represents the step height.

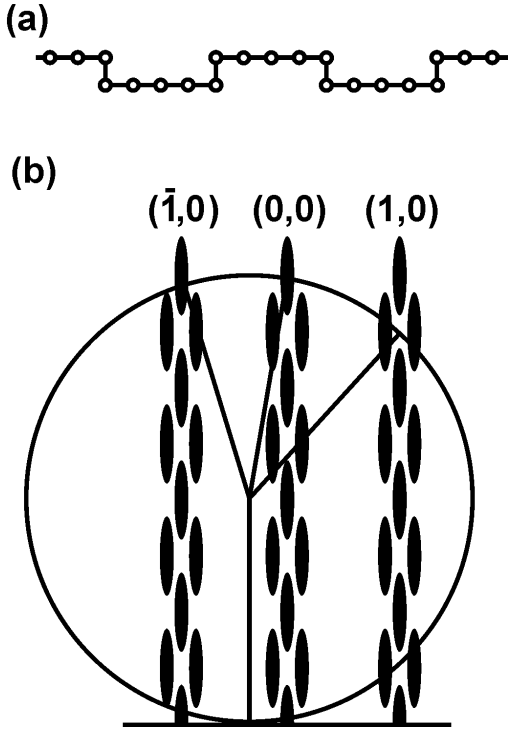

Figure 4.17: (a) *A cross section of a surface consisting of a regular step array, and* ***(b)*** *the corresponding 2D reciprocal lattice with the Ewald sphere. With the shown position of the Ewald sphere, the (0,0) reflects the in-phase condition, and the (1,0) the out-of-phase condition between adjacent terraces. Figure reproduced from [193].*

III. Optical properties of MgO/Mo(001) thin films

III.1. Electroluminescence of MgO films

III.1.1. Results

Electroluminescence measurements are performed on thin MgO films grown on Mo(001). The photon emission is excited via electron injection from the STM tip into the MgO surface in the field-emission regime (chap.2, sect. III.2). Emission spectra are acquired for electron energies ranging between 40eV and 200eV. Hereby, current and acquisition time are limited to 1nA and 60s, respectively, to reduce electron-induced damage of the film [195]. With increasing electron energy, an exponential increase of the photon yield is observed. However, the spectral characteristic of the emission remains unchanged. Figure 4.18a presents a series of photon emission spectra taken at –200V tip bias for MgO films with increasing thickness. Spectra excited with lower electron energies (40eV) are qualitatively similar, but show reasonable signal to noise ratios only for extended accumulation times (figure 4.18b). In almost all spectra, two emission bands are identified, located around 280nm (4.4eV) and 400nm (3.1eV), respectively. With increasing film thickness, both bands gain intensity, whereby the low-energy band at 3.1eV is more affected. Saturation of the total emission yield as a function of film thickness is observed for films thicker than 40ML.

As geometric and electronic tip properties slightly vary from one experimental run to another, the set-up does not allow for a quantitative comparison of the emitted light intensity. This means, identical bias/current conditions might yield different emission cross-sections.

Besides, the Bremsstrahlung created by the injection of high-energy electrons into the sample has to be taken into account as additional source of high-energy photon emission. The cut-off of the optical system (chap.2, sect. IV) creates an artificial maximum between 250nm and 270nm that might contribute to the 280nm band. The effect is strongest for thin MgO layers, because the Bremsstrahlung is more effectively produced by electron injection into the underlying metal support.

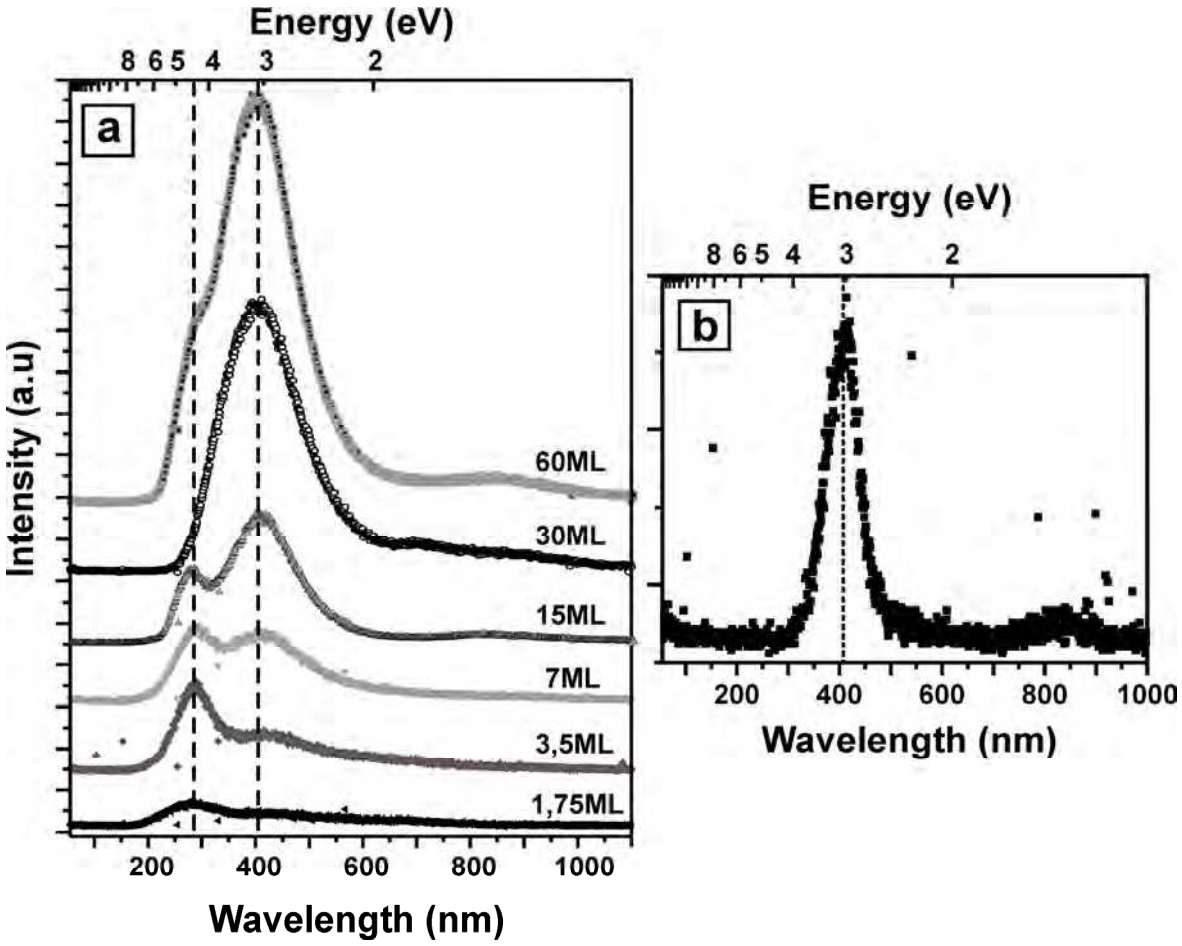

Figure 4.18: *Photon emission spectra collected from* ***(a)*** *MgO films with increasing thickness for a constant excitation bias (U_{tip}= -200V),* ***(b)*** *a 100ML thick MgO film (U_{tip}= -40V). All the spectra were taken for a field emission current of 1nA and an accumulation time of 60s.*

III.1.2. Discussion

Optical measurements of a freshly cleaved MgO(001) single crystal reveals no photon absorption and low reflection in the visible and the near ultraviolet range, and the optical activity starts only when the energy of the exciting photons/electrons is close to the MgO bandgap, where excitonic processes start to take place [196]. However, measurements from high-surface-area MgO samples, such as powders [22] and smokes (nanocubes) [176], reveal a luminescent spectrum, when excited by UV light with energies, much lower than the bandgap of the bulk solid. These new luminescence bands are traced back to local surface states induced by the presence of surface point defects, which locally modify the electronic

charge distribution. The most important point defects on an MgO(001) surface can be classified into three types [143]: (i) Ions with reduced coordination, (ii) ion vacancies, and (iii) adsorbed species (e.g. hydroxyl groups, impurity atoms).

The first category concerns the sites where the ions are no longer fivefold coordinated (5C) but in low coordination. These sites are encountered along edges (4C), steps (4C), at corners (3C), and kinks (3C) (figure 4.19). The typical steps on MgO(001) surface align most of the time with the ⟨100⟩ direction, which is the most stable direction, since the ion coordination is reduced as little as possible, and the stoichiometry of the crystal is maintained along it, resulting in a zero dipole moment [21].

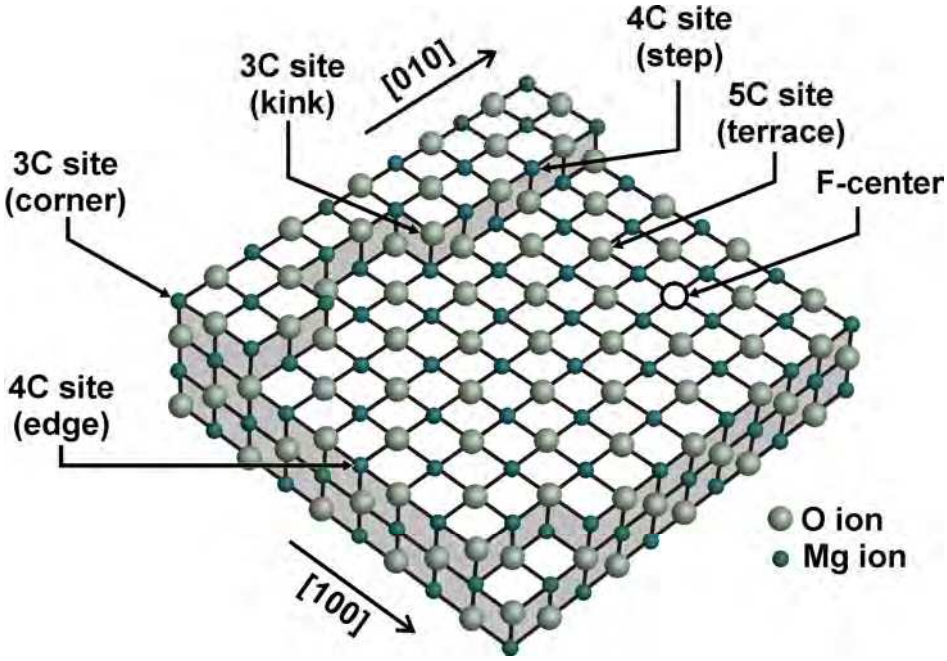

Figure 4.19: *Model surface showing the different low-coordinated ion sites and a neutral F center on an MgO(001) surface.*

The second category of defects refers mainly to single oxygen vacancies, which are usually called *color centers* or *F centers* (F assigns to *Farbe*, a German word meaning *color*). The F center can exist as neutral one, where two electrons reside at the defect site, or as charged center having one or zero electrons. In the last two cases, the defect has a net charge of +1 or +2, [21], and is denoted F^+ or F^{2+} center, respectively.

The creation of an F center in the MgO lattice is accompanied by a relaxation of the lattice aiming to maintain local charge neutrality [21,143]. An F center can be created at different oxygen sites in the MgO; therefore, it can be 6C, 5C, 4C, or 3C coordinated as well. The local alteration of the surface electronic structure as induced by the presence of the defect generates new energy states inside the bandgap. Figure 4.20 shows calculated energy states of F and F^+ centers as well as of excitonic states located at terraces and corners of the MgO surface [197].

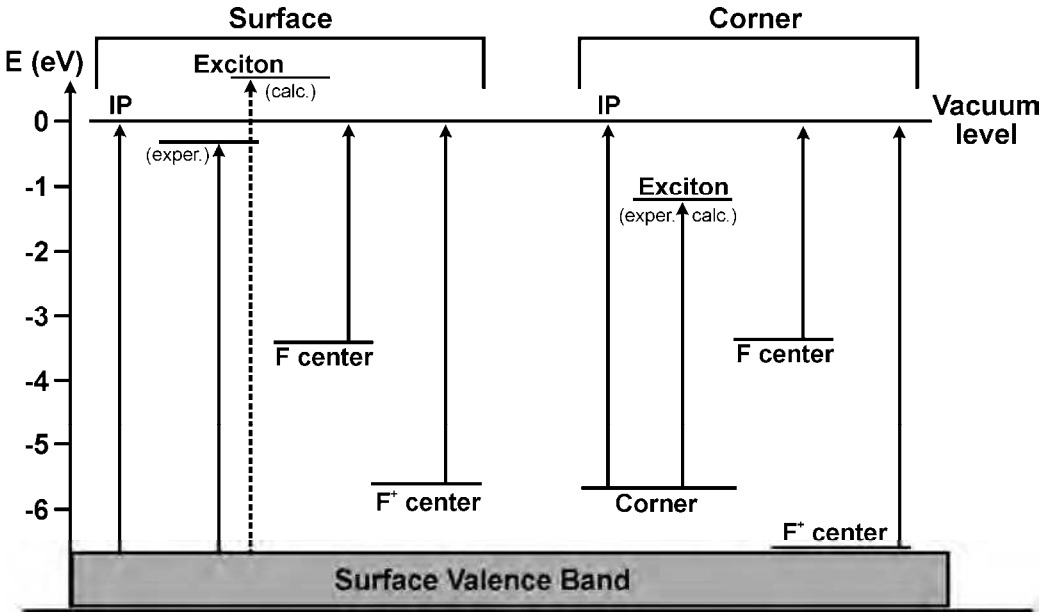

Figure 4.20: *Diagram showing ab-initio calculated energy positions of different defect states in the MgO surface. IP (Ionization Potential). Figure reproduced from [197]*

Based on this theoretical modeling, the recorded photon emission (figure 4.18) can be attributed to two processes, which involve either low coordinated sites or F centers. The first step in both processes is the formation of surface excitons created from the interaction of O^{2-} ions with the impinging electrons. Thereby, electron transition from the O^{2-} ions (Valence band) to the neighboring Mg^{2+} ions (Conduction band) takes place. The excitons are dominantly excited at terrace sites (5C sites), which represent the most abundant surface sites. The created excitons on the MgO surface are mobile and can diffuse away from their excitation points in a random-walk type of motion [25]. The diffusion stops when the electron-hole pair is trapped at a defect site. The trapping occurs because of the locally

reduced bandgap and the resulting enlarged exciton binding energy at the defect [25]. The defect sites are therefore preferential recombination centers for surface excitons and dominate the emission characteristics of MgO. In some photoluminescence measurements on defect-poor MgO nanocubes, two emission bands have been identified at 3.84eV and 3.2eV and assigned to the radiative recombination of excitons at 4C edge and 3C corner sites, respectively [25,23]. This interpretation is in accordance to previous data on MgO smokes [150] and theoretical calculations [25,197]. Slightly different results were reported by other groups, with emission bands somewhat red-shifted to 3.2eV for the 4C and 2.7eV for the 3C emission centers [22,133]. On the other hand, an emission band at 3.2eV detected for MgO single crystals was claimed to originate from an emission mechanism involving F^+ centers [198,199].

During our spectral acquisition, an area of around $1\mu m^2$ is exposed to 1nA flux of field emitted electrons. It results in an electron exposure of about 500 electrons per surface oxygen atom every second. For a tip bias at -200V, oxygen atoms are highly probable to desorb from the MgO surface, creating color centers in an Auger-like process [200]. Yet, if the observed photon emission (figure 4.18) involves F and F^+ centers, the emission intensities should increase rapidly during the acquisition time. However, none of the MgO recorded electroluminescence spectra shows such a behavior. The photon yields as well as the spectral characteristics of the MgO emission were found to be constant over the acquisition time. Moreover, at low tip bias (e.g.: -40V), the cross section for F center creation is small [200], and in spite of this, clear characteristic spectra could be obtained (figure 4.18b). Furthermore, the intentional creation or annihilation of F centers in the whole surface does not produce any change which could relate exciton decay at those centers. Indeed, as presented in figure 4.21, color centers have been intentionally created into the MgO surface by exposing the film during 10 minutes to a flux of energetic electrons (1mA/300eV). Compared to the spectrum taken before electron bombardment, the emission intensity from the bombarded film is found to be smaller. This points to a minor role of surface color centers in the emission process detected here. The reverse approach, namely the removal of potential colour centers by healing MgO films in $1x10^{-7}$ mbar oxygen, led to a similar conclusion, as the emission yield was not completely quenched even after prolonged O_2 exposure (figure 4.18b). All these observations suggest that F centers formed during spectral acquisition are not the main cause of the light emission, and thus, they are ruled out as the dominant source for light emission observed in this experiment from the MgO surface.

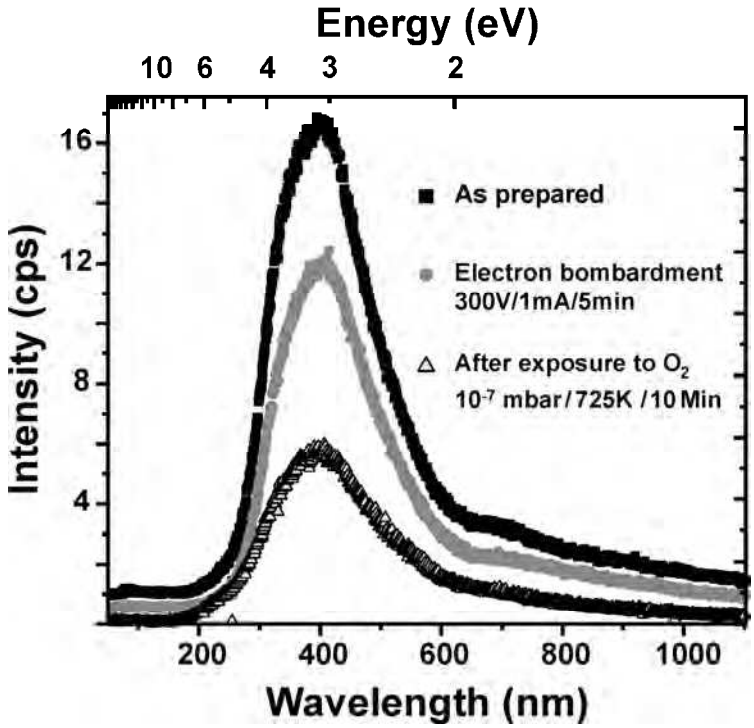

Figure 4.21: *Photon emission spectra from a 30ML thick MgO film (U_{tip}= -240V, I =1nA). The experiment is performed to check the role of color centers in the electroluminescence of MgO films. Upper curve: As prepared film, central curve: After electron bombardment (1mA/300eV/10min) to create color centers, and lower curve: After exposure to 45 Langmuir O_2 to annihilate the color centers. Neither the changes in the spectral shape nor the intensity variation correspond to an electroluminescence mechanism that involves color centers.*

The two bands in the optical emission spectra are therefore interpreted as signature of radiative exciton decays at low-coordinated MgO sites. The emission peak at 3.1eV agrees well with the main feature detected in previous photoluminescence experiments on cube-shaped MgO nano-crystals [133,25,201]. Based on model calculations, this band has been assigned to emission centers located at 3C corner sites in the MgO surface [25]. The second peak measured at 4.4eV in this experiment is interpreted as an emission pathway involving higher coordinated sites. Similar bands in photoluminescence spectra have been attributed to emission from 4C anion sites located at MgO step edges before [25,201]. An unambiguous assignment of the optical pathway is not possible here due to the less-regular film morphology compared to the well-defined MgO nanocubes.

MgO luminescence peaks observed in our experiment are generally red-shifted with respect to earlier photoluminescence data. A number of reasons might be responsible for this discrepancy. The limited thickness of the MgO film supported by Mo(001) crystal might

enable interactions between electron-hole pairs in the oxide and their image in the highly polarizable metal support, which could lead to reduced excitation energies.

Finally, the observed dependence of the emission yield on the film thickness is connected to the probability for a surface exciton to reach a low-coordinated step or corner after activation on a distant terrace site. This probability depends on the lifetime of the electron-hole pair and the surface morphology. In the case of ultra-thin MgO films on Mo(001), the exciton lifetime is governed by the presence of non-radiative decay channels provided by the metal support (Landau damping). The exciton lifetime, and therefore its probability to undergo radiative recombination, increases when the MgO surface is spatially decoupled from the Mo substrate via a thick oxide spacer. This behavior is reflected in our observation where the emission yield initially increases with film thickness but saturates for higher MgO coverage. The influence of the metal support apparently vanishes for films containing more than 40 layers, which enables a rough estimation of the interaction length between MgO surface excitons and electronic excitations in the Mo support.

III.2. Au deposition and MgO optical behavior

III.2.1. Au particle deposition

The Au particles are prepared via vapor deposition from the gas phase onto MgO films held at room temperature. To identify the nucleation sites of the Au particles, two deposition schemes are employed: (i) Au evaporation with a negative potential of –800eV applied between sample and gold doser (referred to as 'sputtered sample') and (ii) deposition with doser and sample hold at the same potential (referred to as 'non-sputtered sample'). In the first procedure, a small amount of Au^+ ions formed in the evaporation process (≈0.5%) is accelerated towards the MgO surface and creates additional defects, acting as potential Au nucleation sites (chap.3, sect. II.2.2). In the second case, nucleation takes place exclusively on the pre-existing adsorption sites of the oxide film. The amount of deposited Au on MgO was varied between 0.06ML and 2.50ML. The Au coverage is calibrated via Au deposition onto clean NiAl(110), where gold grows in a layer-by-layer fashion. The coverage is then directly determined from STM images via the size of the 2D Au islands. To explore the influence of the MgO thickness on the Au nucleation behavior, Au deposition is investigated on 12.5ML and 25ML thick MgO films.

Figure 4.22 shows a series of STM topographic images of MgO films after deposition of Au with increasing coverage. The figure reveals that already a deposition of small amounts of Au onto the MgO surface (0.06ML) leads to the formation of aggregates. The Au particle density is rather similar for sputtered and non-sputtered samples in this growth stage. However, the particle arrangement distinctively differs for the two Au deposition procedures: the Au particles are nearly homogeneously distributed on the steps, corners, and terraces of the MgO surface when Au is sputter-deposited. On the non-sputtered samples, Au exclusively nucleates along step edges and at corner sites, while almost no particles nucleate on the terraces. The difference can be attributed to the presence of artificial surface defects that are created by the impact of energetic Au^+ ions during sputter-deposition of Au. On non-sputtered samples, heterogeneous nucleation takes place at the low-coordinated sites that exist on the as-prepared MgO surface (sect. II.2). The absence of Au particles on the MgO terraces suggests that point defects are either not available or unimportant for the Au nucleation at room temperature. Besides, no obvious effects of the MgO thickness on the nucleation of Au particles are noticed on these non-sputtered films.

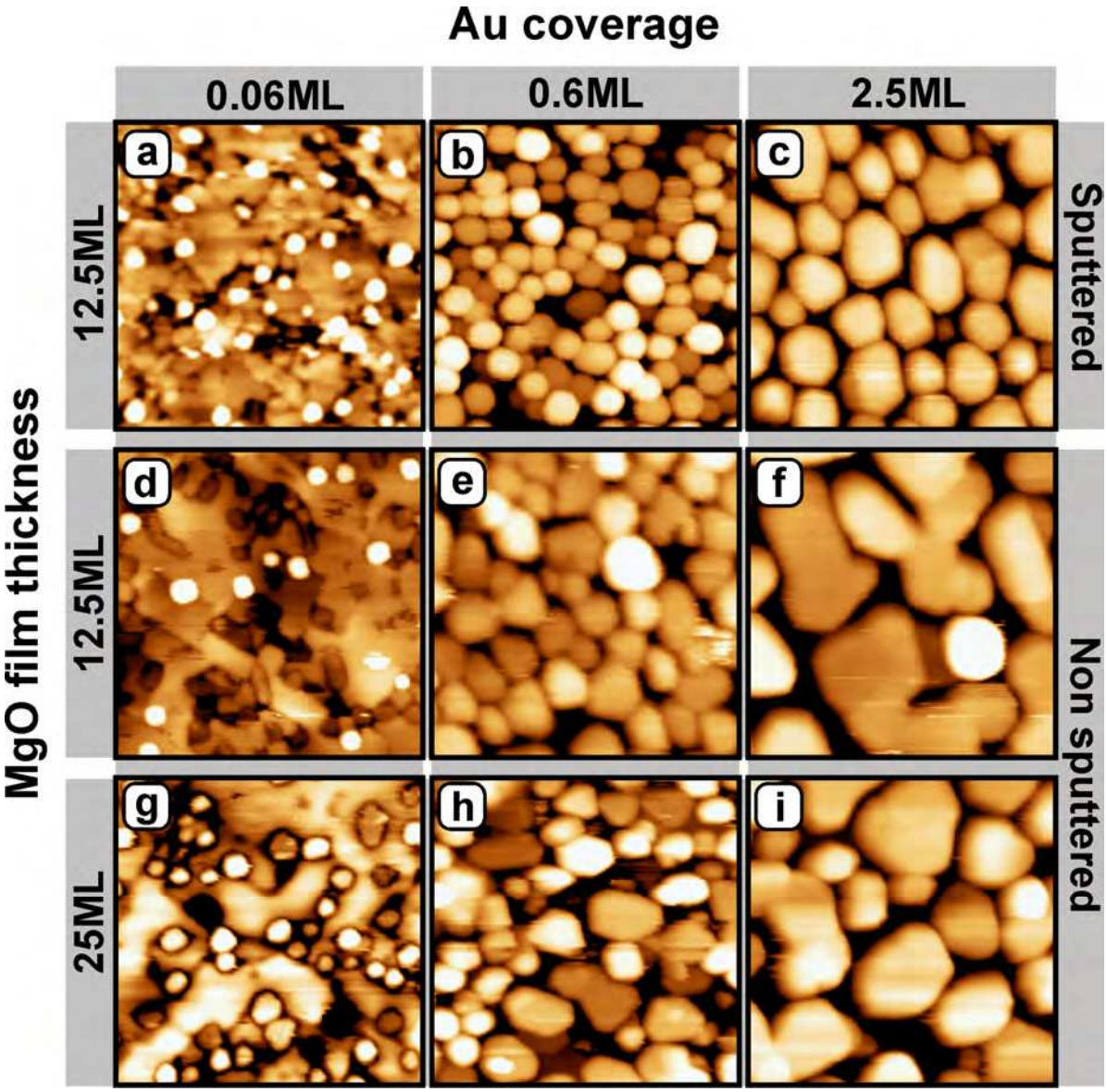

Figure 4.22: *23×23nm^2 STM topographic images of MgO films grown on Mo(001) after deposition of Au with a coverage, from left to right, of 0.06ML, 0.6ML and 2.5ML (U_S = +3.0 V, I = 0.05nA). The MgO films are 12.5ML thick in (a-f), and have a thickness of 25ML in (g-i). While particles in (a-c) are prepared by a sputter deposition of Au, they are grown in thermodynamic equilibrium in (d-i).*

From the STM measurements, the density, shape, and size of the deposited Au particles are found to be dependent on the Au coverage, on the deposition procedure, and on the MgO thickness. The evolution of the structural properties of the differently deposited Au particles is reported on figure 4.23. The figure shows that at low Au coverage (around 0.06ML), the Au atoms assemble into small, flat islands, indicating enhanced metal-oxide adhesion as induced by the Mo support below the oxide [202]. Extended 2D islands, as in case of Au on a 3ML thick MgO film on Ag(001) [161], are not detected here. This deviation is attributed to the larger thickness of our MgO films with respect to the cited experiment, which reduces the influence of the metal support.

When 0.5ML to 1.0ML Au is deposited, the aggregates quickly thicken to compact three-dimensional particles. These particles are characterized by a height to radius ratio of around 0.5 and 0.7 for non-sputtered and sputtered samples, respectively (figure 4.23c). Following the Wulff construction principle, the aspect ratio decreases with increasing adhesion at the metal-oxide interface [111,114]. Therefore, the lower aspect ratio observed on non-sputtered samples indicates relatively strong Au-MgO interactions at steps and corners, while the binding of particles to artificial defects is comparatively weak. The more prominent difference between sputtered and non-sputtered samples is the drastic change in particle density (figure 4.23a). For the sputtered samples, the density sharply increases with metal exposure and peaks at approximately $65x10^{11}cm^{2}$. For non-sputtered samples, the nucleation density rises only slowly and levels out at a value of $15x10^{11}cm^{-2}$, which is four times smaller than for sputtered samples.

For an Au coverage larger than 1ML, a third growth regime becomes noticeable. The particles develop into large crystallites with hexagonal or polygonal shapes, indicating the formation of (111) oriented facets. In addition, the particle density starts to decline again as a result of coalescence between neighboring aggregates on the surface (figure 4.23a). The coalescence is also responsible for a gradual reduction of the particle's aspect ratios (figure 4.23c). Due to intergrowth, the lateral particle dimension drastically increases while their height stays approximately constant. The difference between sputtered and non-sputtered samples is less apparent in the high-coverage regime, which indicated that the morphology is not influenced by details of the nucleation behavior anymore.

The effect of MgO thickness for non-sputtered sample on Au particle geometry can be rationalized as follows: Au particles on thick layers (25ML) exhibit larger aspect ratios (more 3D-like), than those grown on thinner films (12.5ML) (figure 4.23c). This observation is attributed to a slight increase of the Au-MgO binding strength on thinner films due to a residual influence of the Mo support which induces a flattening of the particles according to

Wulff's principle [111,114]. With increasing oxide thickness, the Mo contribution vanishes and Au particles grow with 3D shapes as expected for Au on bulk MgO [111].

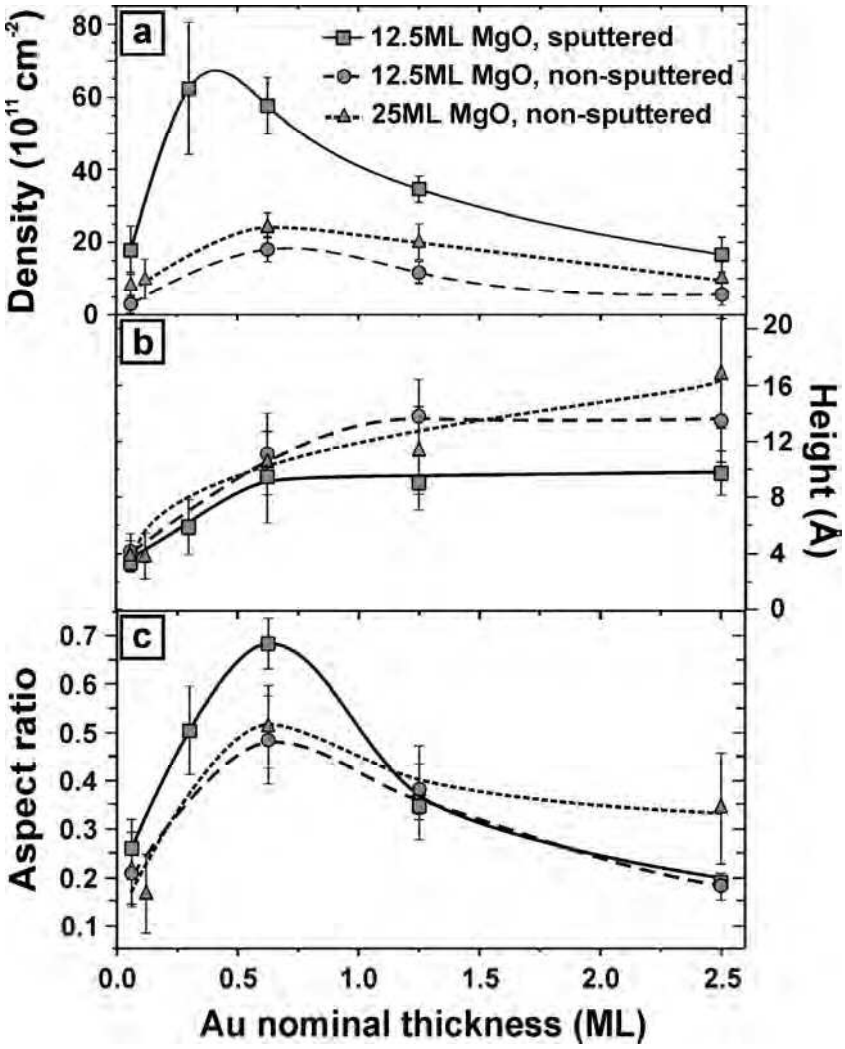

Figure 4.23: (a) *Particle density,* ***(b)*** *averaged particle height, and* ***(c)*** *aspect ratio of Au particles on 12.5ML and 25ML thick MgO films. The particles are either prepared by sputter- or non-sputter deposition of Au. These data are derived from STM measurements as shown in figure 4.22. The lines are guides to the eye.*

III.2.2. Au-dependent evolution of MgO optical behavior

Figure 4.24 presents typical optical spectra of MgO thin films after exposure to increasing amount of Au following the two different manners discussed before. The optical emission from MgO films was stimulated by injection of field-emitted electrons from the STM tip. The spectra were recorded using a grating spectrograph blazed at 500nm, unlike the data shown in figure 4.18 and 4.21, where a blazing of 300nm was used (chap.2, sect. III.2). As the optical sensitivity of the 500nm grating is highest between 500nm and 700nm and declines around 400nm (chap.2, sect. III.2), the spectrum of bare MgO exhibits an asymmetric emission line with a weak shoulder around 550nm. Also, the position of the intrinsic MgO emission from the corner sites is systematically shifted from 400nm (3.1eV) to about 420nm (2.95eV), and the typical luminescence at 280nm (4.4eV) from edge sites is almost completely suppressed. The use of the 500nm blazed grating is motivated by its high optical sensitivity between 600nm and 650nm range, where the position of the optical response of the Au particles is expected; while the sensitivity of the 300nm blazed grating is comparatively small in this range (chap.2, sect. III.2).

It becomes clear from figure 4.24, that the emission spectrum of MgO is considerably altered upon gold deposition. Already in the low-coverage regime, a new emission line emerges in the wavelength region between 600nm and 650nm (2.0eV to 1.9eV). With increasing Au exposure, this peak gains intensity with respect to the MgO related feature and finally dominates the optical spectra for 2.5ML nominal Au thickness. The new emission line is attributed to the radiative decay of Mie plasmons, excited in the Au particles by the electron injection (chap.1, sect. III.2.3). The emission here corresponds to the (1,0) Mie plasmon mode, because electron injection from the tip exclusively excites this mode. The plasmon energy of a spherical Au particle can be estimated for a given dielectric surrounding using formula (1.24). Assuming an Au particle environment composed from 30% MgO ($\varepsilon_{MgO} = 3.2$) and 70% vacuum, the plasmon energy computes to 2.2eV, which is in reasonable agreement with the peak position observed in the optical spectra. The assignment of the new emission line to Mie-plasmon excitations in Au particles is corroborate by the observation of similar features in the optical response of Au particle ensembles on various dielectric supports [203,204]. In this section of this chapter, the focus is mainly on the influence of nucleation and growth of Au particles on the optical activity of MgO films. It is not aimed to discuss the evolution of the Mie energy position of the Au particles as the function of their aspect ratio and density for the different preparations (figure 4.23c). The effects of the morphology of the particle ensemble on the Mie plasmon energy have already been discussed in details for similar systems in the previous chapter (chap.3).

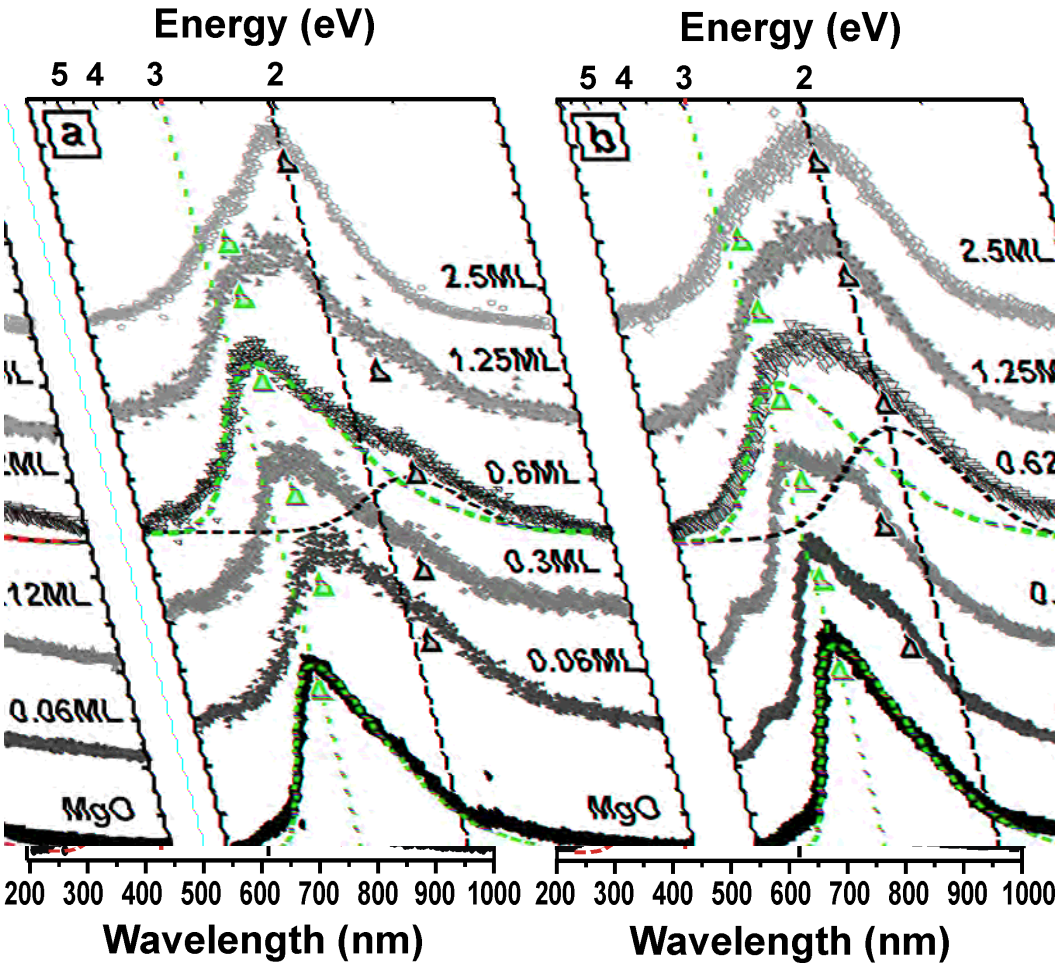

Figure 4.24: *Normalized photon emission spectra recorded for MgO thin films covered by an increasing amount of Au.* ***(a)*** *Sputter-deposition of Au onto a 12.5ML thick MgO film.* ***(b)*** *Non-sputter deposition of Au onto a 25ML thick film. The spectra were taken for a field emission current of 1nA and tip bias of U_{tip} = -200V with an accumulation time of 60s. The spectra are fitted with an asymmetric and a symmetric Gaussian to account for the MgO and the Au contribution, respectively (as shown for the central spectrum). The large triangles mark the maximum position of the respective fits in all spectra.*

The general evolution of the MgO luminescence with increasing Au exposure, where the Au Mie plasmon radiation gains intensity with the detriment of MgO emission line, is rather similar for sputtered and non-sputtered samples. Nevertheless, a more careful evaluation of the spectra provides valuable insights into the growth characteristics of gold in both cases. The analysis is performed by the deconvolution of the emission spectra into intensity stemming from low-coordinated MgO sites and intensity related to Au Mie plasmon resonance. To model the MgO contribution, the photon emission of the bare oxide is

described by an asymmetric Gaussian peaking at 420nm. This spectral shape is kept constant during the following fitting procedure, modifying only position and intensity of the peak as a function of Au load. A Gaussian curve with adjustable height, width and energy position (confined to a range between 500nm and 700nm) is used to account for the Au spectral contribution. The sum of both components reproduces the experimental spectra and allows a separation of the total photon response into a MgO and an Au portion. The fitting procedure of the optical spectra revealed a red shift of the MgO emission line from 420nm for bare MgO to 455nm for films covered with 2.5ML of Au. The shift indicates changes in the dielectric environment and the local electronic structure of the MgO emission centers during Au exposure. This provides a first evidence for the strong interaction between the optically active MgO sites and the Au deposits. Also, the Mie-plasmon energies change considerably with increasing Au coverage. For non-sputtered samples, the plasmon shifts from 2.0eV to 1.85eV with increasing Au coverage, due to the initial increase and then the relative stabilization of particle aspect ratio as seen in figure 4.23c. For sputtered samples, the Mie energy is around 2.0eV at low and high Au coverage, but runs through a minimum of 1.8eV at approximately 0.5ML Au thickness. The decrease of the plasmon energy is connected to the formation of Au particles with large aspect ratios (~0.7) in this intermediate growth stage (figure 4.23c).

To quantify the evolution change of the MgO emission intensity as a function of Au coverage, the relative intensities of the fitted Au and MgO peak areas (A_{Au}, A_{MgO}) are plotted in figure 4.25. The relative intensity I^{rel} is defined as the ratio between A_{Au} or A_{MgO} and the integral intensity $(A_{MgO}+A_{Au})$, i.e., $I_{Au}^{rel} = A_{Au} / (A_{MgO}+A_{Au})$ and $I_{MgO}^{rel} = A_{MgO} / (A_{MgO}+A_{Au})$. Since the sum of I_{Au}^{rel} and I_{MgO}^{rel} is equal to 1, the plots in figure 4.25 follow a mirror-like fashion.

Figure 4.25 shows that the MgO intensity follows the same general trend for sputtered and non-sputtered samples as well as for thin and thick MgO films: The MgO-related signal is reduced more or less rapidly from 1.0 for bare MgO to ~0.4 for an Au coverage of 2.5ML. The non-zero MgO signal even at high coverage indicates that a fraction of optically active centers survives between the particles. The quenching rate of the MgO signal is, however, rather different for the various preparation procedures. The fastest decay is observed for thick MgO films and a non-sputter deposition of gold, where the intensity decreases roughly exponentially with Au coverage (figure 4.25, dotted line). For thin films and sputtered samples, the intensity declines more gradually and follows a nearly linear dependence on the Au load (figure 4.25, dashed and solid lines). This difference is easily understood on a qualitative base: For Au deposition in thermodynamic equilibrium (non-sputtered sample), the particles nucleate at intrinsic MgO binding sites (heterogeneous nucleation) (sect. III.2.1). These nucleation sites are apparently identical to the optically active centers in the oxide surface, as manifested by the rapid decay of the MgO emission intensity during Au

deposition. So obviously, the characteristic MgO emission centers are located at edge, corner, and kink sites, and seem to play an important role in the Au nucleation process on the MgO surface.

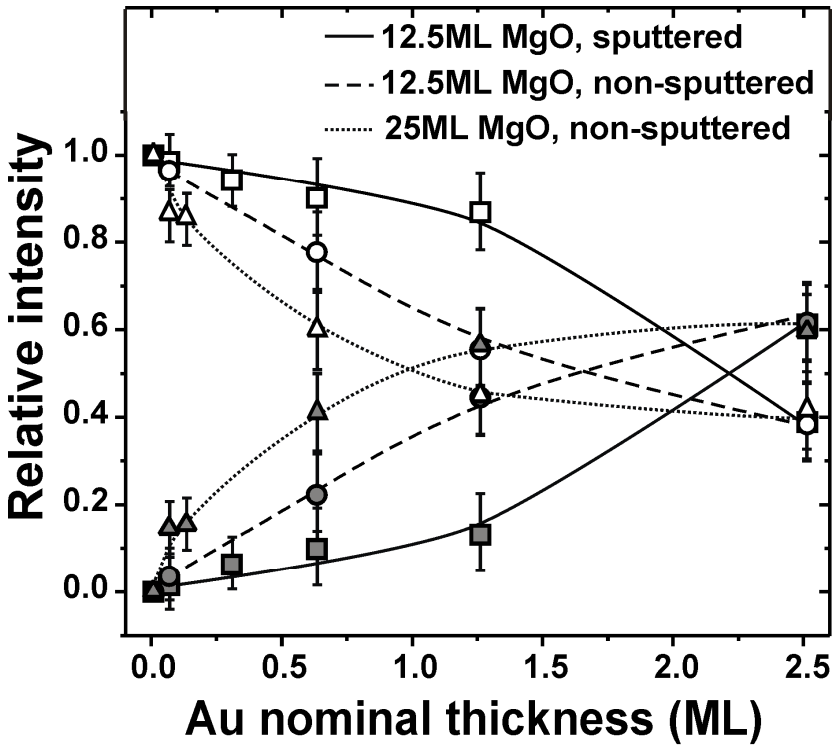

Figure 4.25: *Relative contributions of the MgO and Au-derived photon signals to the integral emission intensity as a function of Au coverage. The open symbols depict the relative MgO intensity and the closed symbols are for the Au values. The lines are guides to the eye. As the Au coverage increases, the MgO emission is quenched. The light emitted from MgO reduces most rapidly for thick MgO films, where Au particles nucleate exclusively at edge, corner, and kink sites. This behavior confirms the location of the optically active centers on these low-coordinated sites.*

For thinner MgO films, the Au nucleation characteristic is altered by the influence of the Mo support and the resulting increase of the Au-MgO adhesion. As a consequence, the nucleation process is not exclusively governed by low-coordinated sites any more, but also takes place at MgO terraces [202]. As five-fold coordinated terrace sites are not relevant for the emission properties of MgO, the optical response declines less rapidly with increasing Au load than on thick films. This trend is further amplified for a sputter-deposition of Au onto the MgO films. The impact of high-energy Au^+ ions creates new binding sites in the oxide surface, which compete with the intrinsic nucleation centers and diminish their importance in the particle formation process. Consequently, low-coordinated MgO sites remain empty even for higher Au loads and continue to contribute to the optical signal, thus leading to the slower decline of the MgO emission signal.

The reason for quenching the MgO photon emission for increasing Au coverage might be related to (i) an opening of non-radiative decay channels for trapped excitons involving the Au particles, or to (ii) a change in the electronic configuration of low-coordinated MgO sites covered by the Au preventing trapping of excitons. Exciton decays involving the Au particles is the more plausible process and could even explain the relatively strong Mie-plasmon emission detected from rather small particles. In this scenario, excitonic modes trapped at particle binding sites could enhance the excitation cross-section of the Mie plasmon. A possible influence of Au deposits already in the creation process of excitons is excluded here, because MgO terrace sites governing the exciton formation are only sparsely covered with particles. The second possibility would infer that the excitons created at the terraces should decay with energies that are higher than from the 3C and 4C sites. In this case, a blue-shifted of MgO emission line should be observed. As the blue-shifted emission is in disagreement with the obtained results (figure 4.24), the possibility (ii) is discarded.

The Au nucleation behavior on MgO/Mo(001) deduced from the present experiments is in general agreement with earlier experimental and theoretical studies. Heterogeneous nucleation was observed for various metals on the MgO surface, indicating the dominant influence of oxide defects in the initial adsorption process [111,205]. For thin MgO films on Ag(001), the defect-assisted nucleation of Au was directly derived from the quenching of the paramagnetic F^+ defect signal in MgO with increasing Au load [206]. The importance of oxygen vacancies and low-coordinated edge and corner sites for the adsorption of metal atoms has also been predicted by theory and traced back to a strong increase of metal-oxide interactions at surface defects [136,207].

III.3. Photon mapping and local spectroscopy with the STM

In order to localize the light emission-centers on the MgO surface, we have performed spatial-resolved optical analysis while imaging the surface topography of a 12.5ML thick MgO film using the photon-STM. In the next two sections, we have carried out this measurement by using two different STM tip materials, Au and Ag. The study includes photon mapping as well as optical spectroscopy of the MgO surface. The STM tips were obtained by electrochemical etching of Au and Ag wires. All the data presented below were obtained at liquid nitrogen temperature.

III.3.1. Au tip–MgO junction

Optical maps of the MgO film taken with a gold tip for increasing sample bias are presented in figure 4.26 together with their corresponding topographic images. Intensive light emission starts to be detected when the sample bias reaches about 4.5V and stays detectable until 7V. The spatial distribution of the emitted light on the MgO surface strictly depends on the bias, i.e., the optical activity of a defined area is controlled by the sample bias. In the low-bias regime, the emission is spatially confined to the center of large oxide terraces. The optically active area increases with sample bias until the whole top-most MgO layer appears bright at around 5V. Further increase of the voltage causes a rapid decrease in the emission intensity at the upper oxide terraces, while areas around the dislocation step regions become bright. These dislocation steps are induced by the formation of screw dislocations at MgO grain boundaries that are typical for MgO/Mo(001) films with thicknesses around 12ML (see sect. II.2). Around 6V, light emission is restricted only to the edge lines. The spectral distribution of the emitted light is found to be independent of the STM tip location on the MgO surface and of the sample bias. The emitted light is not compatible with the intrinsic emission properties of the MgO surface, as illustrated by figure 4.27. The emission spectra obtained at 5V to 7V sample bias peak at around 750nm-800nm (~1.6eV), which is strongly red-shifted compared to exciton decay at corner (3.1eV) and step sites (4.4eV) (see sect. III.1.2).

In addition to the light emission contrast, the MgO surface topography is found to exhibit strong bias dependency (figure 4.26). Whereby, at the light emission onset in the photon maps an artificial increase of the topographic height is observed in STM imaging. The same observation is made when light intensity drops-off.

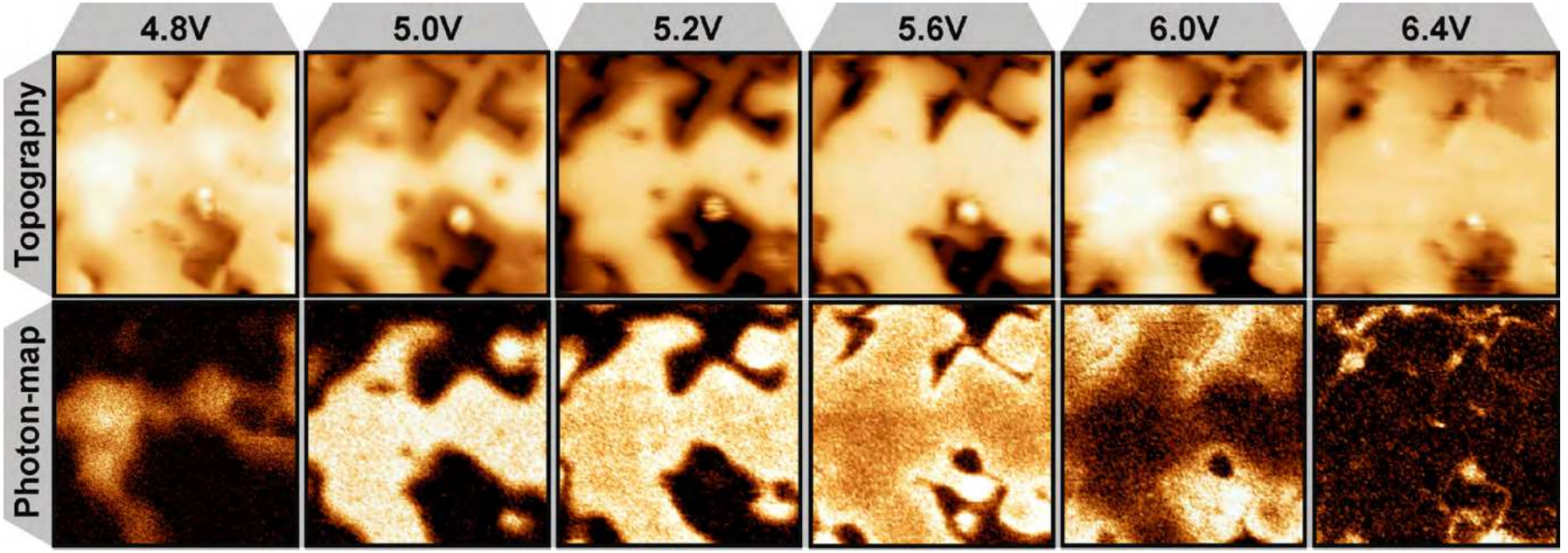

Figure 4.26: *40×40nm^2 topographic images and corresponding photon maps of a 12.5ML thick MgO film for different sample bias taken with Au STM tip. The tunneling current was set to 2nA*

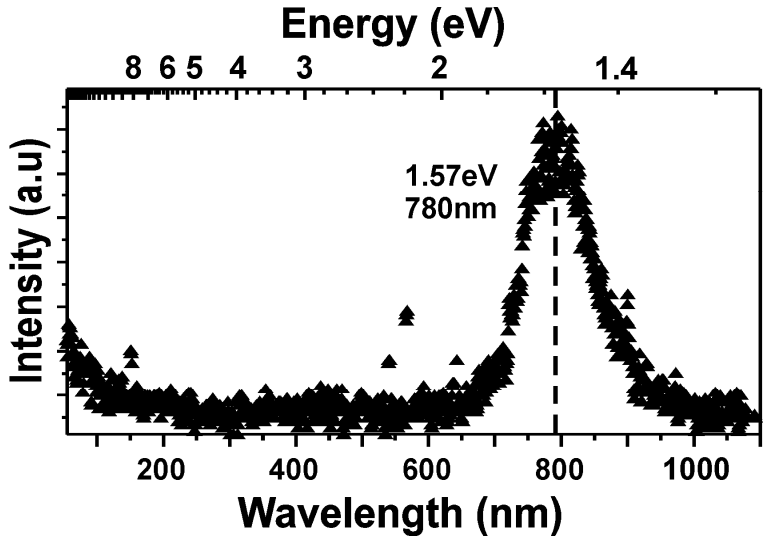

Figure 4.27: *Typical photon emission spectrum from Au tip-MgO/M0(001) junction measured while tunneling with 5V sample bias and 2nA current. The MgO thickness amounts to 12.5ML.*

The contrast variation in the MgO surface topography as a function of sample bias and at different place on the MgO surface (figure 4.26) is attributed to spatial variation of the conductivity of the STM junction. Furthermore, after depositing more than 2ML of MgO on the Mo(001) surface, the work function of the Mo reduces from 4.53eV to 2.5eV [208]. Thus, the used sample bias to excite light emission is higher than the MgO/Mo(001) work function. At this condition, the electron transport from the STM tip to the sample most likely involves field-emission resonance states (FER) (see chap.1, sect. II.3). Such resonances are characterized by a high electron transmission probability and carry a large portion of the electron current at elevated voltages. The bias position of FERs can be determined from distance-versus-voltage spectra (dz/dU_S) taken with enabled feedback loop. Thereby, sharp augmentations in the conductance induce sudden changes in the tip-sample separation (z), which cause then pronounced maxima in the dz/dU_S spectra. Figure 4.28a shows typical dz/dU_S curves measured on flat MgO terraces and on dislocation step regions. The FERs on the different places of the MgO surface are clearly revealed by the oscillatory behavior of the conductance. The spectra obtained from both places are similar; however, the FER positions are shifted against each other by ~0.5eV in the presented spectra. As FER energies are sensitive to the work function (see equation 1.16), these shifts indicate a spatial modulation of the work function on the MgO surface. When going from a terrace to a dislocation step region, the work function seems to higher by ~0.5eV.

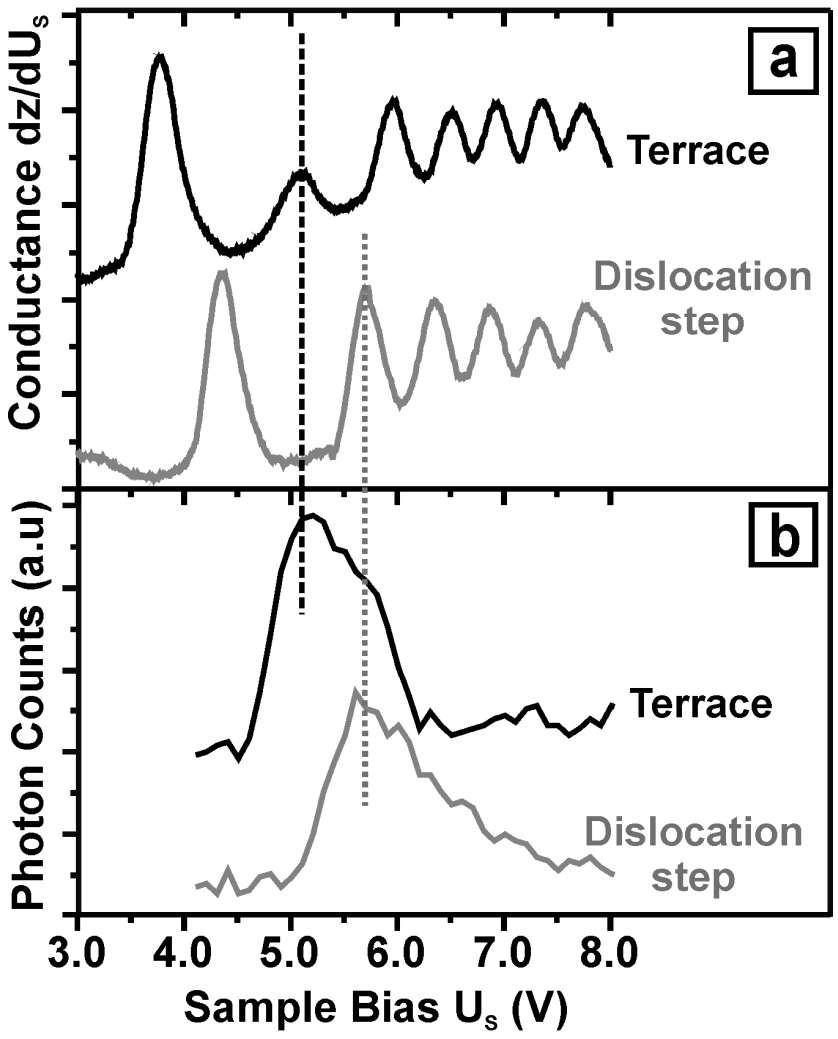

Figure 4.28: (a) *Conductance of the Au–MgO tunneling junction (dz/dU_s) as a function of the sample bias measured at a terrace and in a dislocation step region on the surface of a 12.5ML thick MgO film. z is tip–sample distance in the STM. A current of 20pA was stabilized by the feedback loop during spectral acquisition. The height signal was numerically differentiated. Maxima in the dz/dU_s spectra correspond to field emission resonances.* ***(b)*** *Photon intensity versus bias plot acquired with a photomultiplier tube. Light emission maximum at each probed position occurs around the energy of the second FER level.*

In general, the work function is found to decrease at steps, as observed for metal surfaces [209]. This variation is attributed to the smoothing of the charge distribution around the step, inducing a dipole moment directed inwards the surface which reduces the work function (Smoluchowski smoothing [210]). However, the variation in the local work function at defect regions might have different origins. On *n*- and *p*-doped semiconductor surfaces, work function changes are traced back to the appearance of surface states within the bandgap that

are localized exclusively at the step edges [211,212,213]. Whereas for *n*-type semiconductors the charges in these states induce band bending towards higher energies which results in an increase of the work function, for the *p*-types the work function decreases, as the band bending occurs towards lower energies [211,212,213]. The increase of the work function at steps on *n*-GaAs surface is found to be 0.45eV with Kelvin probe spectroscopy [213], which is in agreement with the measurements on the MgO surface (figure 4.28a). However, filled surface states have not been detected on the MgO surface so far.

Alternatively, the presence of negative charges on MgO dislocation step regions would also provide a conclusive explanation of the local work function increase. Such excess charges induce a local dipole moment that hampers electron extraction from the film. These charges could exist as non-compensated charges related to oxygen excess either in the screw dislocation cores or along the grain-boundary steps (see figure 4.29). Such a non-stoichiometry at defect regions have been observed for oxide crystals having a strong ionic character, like the α-Alumina [109,110,214,215,216]. The existence of such localized charges on the MgO dislocation step regions is, however, not verified; therefore, the precise reason for the local work function increase at the MgO/Mo(001) surface is not clear yet.

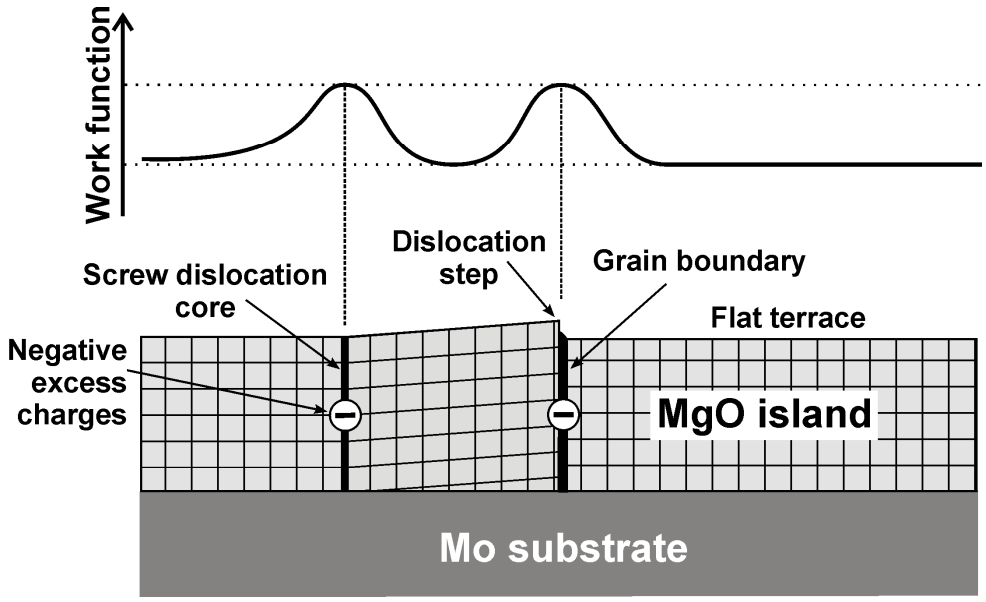

Figure 4.29: *Illustration of the work function increase at screw dislocation cores and dislocation steps at a grain boundary of the MgO surface. The sketch is made in the (100) plane, which corresponds to the slip plane of the screw dislocations for a 12.5ML thick MgO film on Mo(001). The represented negative excess charges are related to a local non-stoichiometry characterized by magnesium deficiency.*

When correlating the bias-dependence of the Au tip-MgO conductance and the observed light emission intensity, as shown in figure 4.28, it appears that the maximum of emitted photon yield is obtained when the bias is around the second FER level. Furthermore, the separation between the first and the second FER levels is found to fairly correspond to the energy of emitted photons. Therefore, the detected light emission is attributed to radiative electron transitions from the second to the first FER level. The MgO film gives rise to FERs with long electron lifetimes, due to the small penetration probability of electrons from the FERs into states of the insulating oxide and the limited number of alternative propagation channels. As a result, radiative transitions of electrons between FER levels become possible and contribute to the photon response from the MgO surface. This mechanism is comparable to the light emission observed from quantum well states in a Na overlayer on Cu(111) [87], but it is rather untypical for metal junctions, due to the presence of efficient non-radiative recombination channels. In a strictly 1D picture, this radiative transitions between FERs are dipole forbidden. The dipole selection rules are however softened by the influence of the tip and the resulting 3D character of FER levels in front of the sample. Neverthess, as it is performed in case of Na thin film on Cu(111) [217], these radiative transitions and the resulting emission yield need to be verified by quantitative calculations in the future.

The exact position of FERs depends on tip shape and tunneling current and can vary by several tens of an electron-volt in different experimental runs (chap.1, sect. II.5). Therefore, the photon energy from transitions between FERs in figure 4.28 does not exactly correspond to the level separation deduced from dz/dU_s spectroscopy.

The spatial dependence of the light emission from the MgO surface in the photon maps (figure 4.26) can now be traced back to the dependence of the FERs on the work function variation across dislocation step regions. With increasing sample bias, radiative electron transitions initially occur in the center of MgO terraces, characterized by a small work function and low-lying FER levels. Then the second FER is reached for the whole MgO terrace, which brightly contrasts against dislocation step regions in the photon maps. A further voltage increase shifts the resonance condition gradually to the dislocation step regions, which subsequently appear brighter in the optical measurements.

On the other hand, the detected light could follow another process. The process consists of the opening of inelastic tunneling channels involving radiative tip-induced plasmons (TIP) (chap.1, sect. III.2.1). High photon yields are expected whenever the final state of the inelastic tunneling process matches a FER (see figure 1.11). The Au tip and Mo surface would play the active parts in supporting TIPs, while the MgO layer acts as dielectric spacer in addition to the vacuum gap between tip and sample. The tip dominates the spectral characteristics of emitted light, because the small imaginary part of the Au dielectric function drastically reduces the plasmon damping in the gold electrode (chap1. sect. III.2.1). The detected light emission is in

general agreement with earlier experiments, where optical emission peaks at approximately 800nm were observed from tunneling contacts containing a Au electrode [33,218,219].

In summary, the emission light from the Au tip–MgO surface detected in our experiment is related either to radiative transitions between field-emission resonances (FERs), to tip-induced plasmons (TIPs) in the tip-sample cavity, or to the two processes at the same time, where the radiative electron transition could be enhanced by the TIP due the energy matching of the two phenomena. To check these assumptions, a second set of experiment has been performed with Ag tips (sect.III.3.2).

III.3.2. Ag tip–MgO junction

The use of silver as STM tip extends the field-enhancement in the tip-sample cavity to higher energies (up to 3.5eV, see figure 1.10) compared to a gold tip [10]. This might facilitate the detection of high frequency optical modes like MgO excitons, which were not seen for Au tips.

As summarized in figure 4.30, the topographic images and the photon maps obtained with an Ag tip shows similar behavior as the one for an Au tip. However, light emission is detected in the bias range from 4.5V to 14V, in contrast to the Au tip (from 4.5V to 7V). For bias voltages higher than 8V, the STM spatial resolution decreases, while photons are still emitted. In figure 4.30, the photon map taken at 8.5V shows that light is still detected whereas the spatial contrast has vanished. For biases higher than 14V, scanning becomes unstable and the tip can only be positioned at selected points above the surface.

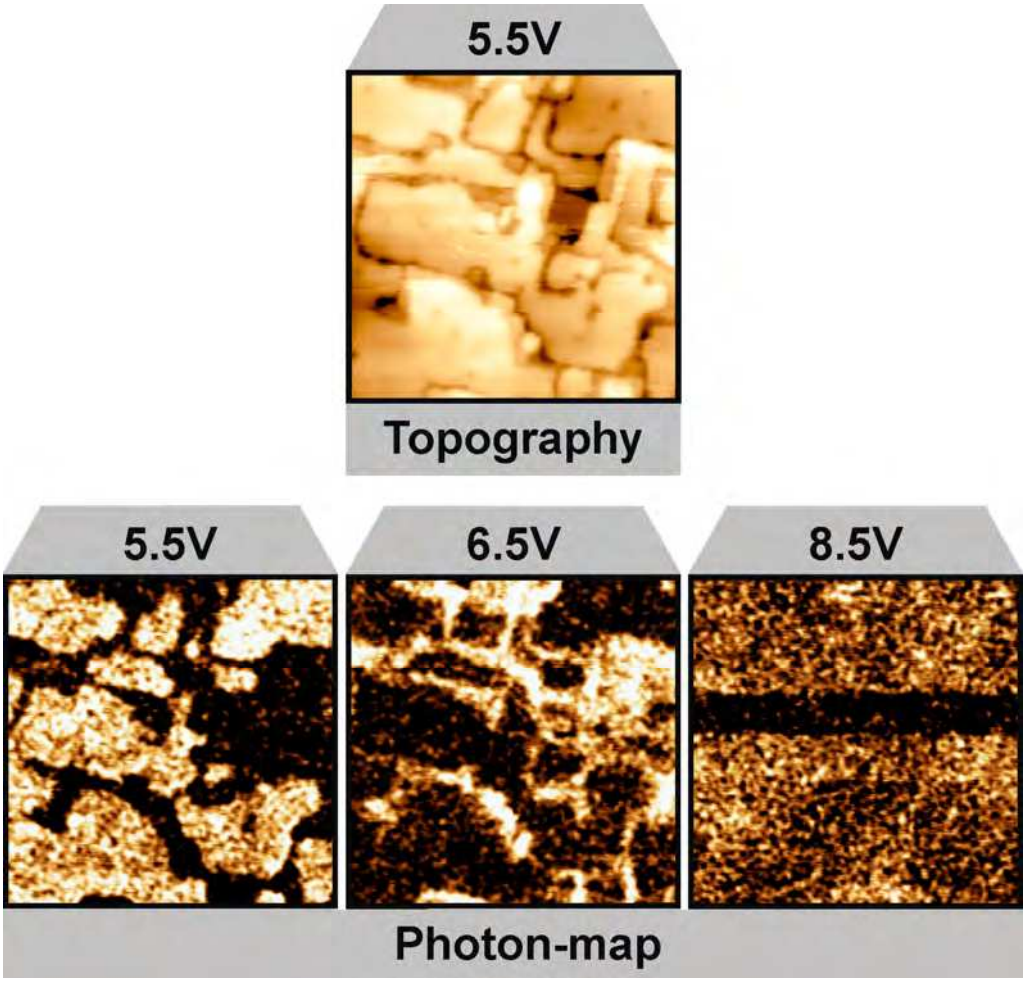

Figure 4.30: *50×50 nm^2 topographic image and corresponding photon maps taken at different sample bias from a 12.5ML thick MgO film using a Ag tip. A current of 2.0nA was used in all measurements. In the upper half of the photon map at 8.5V a smaller current of 0.2nA was used for some lines to define the dark level of the photon signal.*

The spectral distribution of the emitted light for different sample bias is presented in figure 4.31. Compared to the Au–MgO junction, the use of Ag as tip material results in a rich spectral behavior exhibiting a strong dependence on the excitation bias. At the emission onset around 4.5V, a single peak appears in the spectrum at 920nm (1.35eV) that gradually shifts to lower wavelengths with increasing voltage.

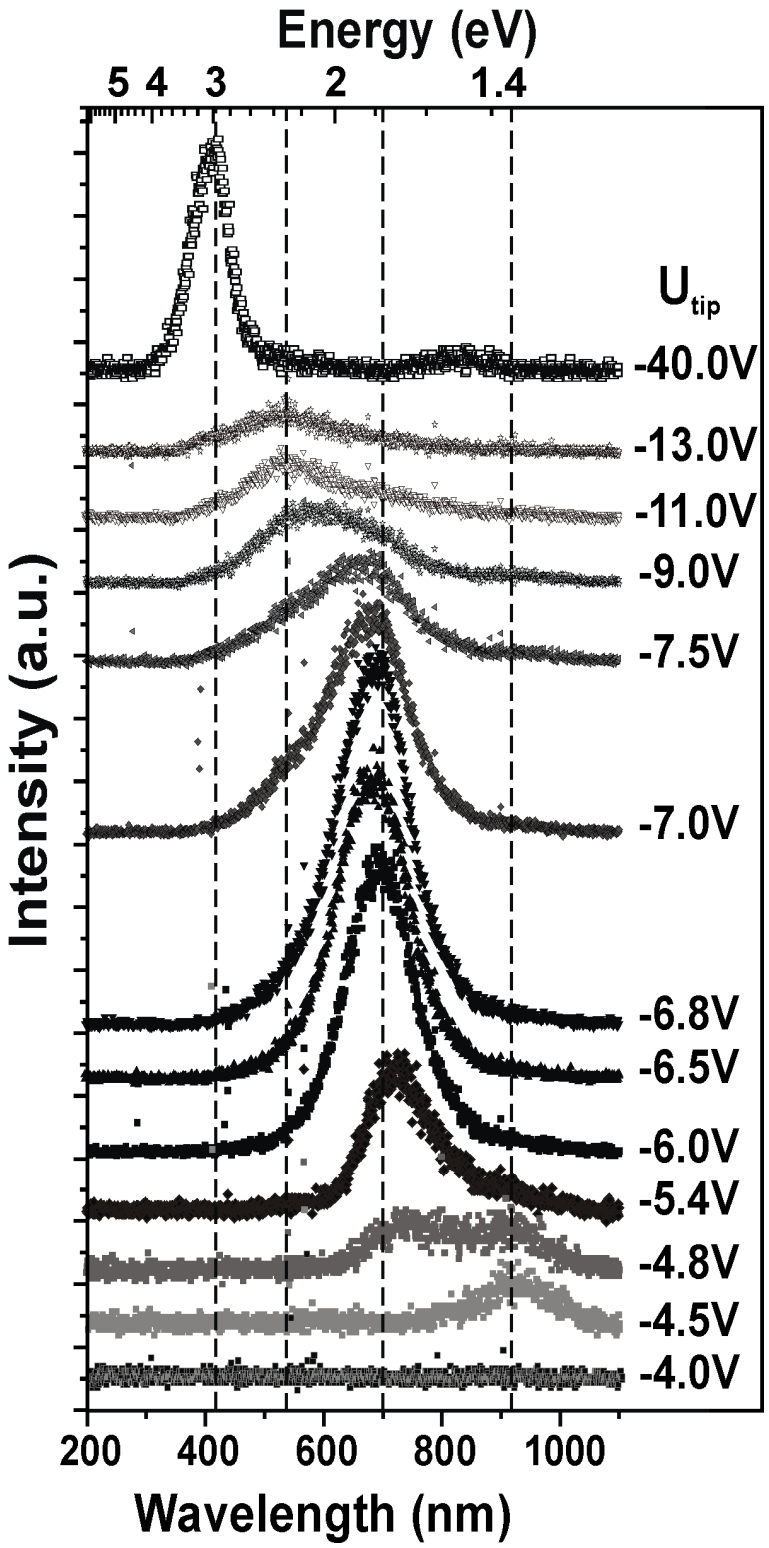

Figure 4.31: (a) *Electro-luminescence spectra as a function of excitation bias from a 12.5ML thick MgO film deposited on Mo(001). The electron current was set to 2nA, the accumulation time per spectrum was 120s.*

This trend is interrupted around 5V, when a second peak emerges at 700nm (1.8eV) in the spectra and quickly develops into the dominant feature. The peak runs through a pronounced intensity maximum between 6.5V and 6.8V excitation bias without changing its wavelength position and decrease again with further bias increase. At 7V, a faint shoulder around 500nm (2.5eV) becomes visible, which then develops into a broad peak visible over a large bias range (7.5V to 13V). Additional photon intensity is observed between 400nm and 450nm (~3eV) for excitation voltages above 10V, however, only with small emission yield. In the far field-emission regime (25V < U_s <100V), the later emission peak becomes very intense and slightly blue-shifts to 400nm (3.1eV).

To illustrate the evolution of different spectral components as a function of excitation bias, the emission spectra were deconvoluted into a set of Gaussian curves. To account for the different spectral lines in the spectra, four Gaussians were necessary to reproduce the intensity distribution for all bias voltages. The evolution of theses emission lines as a function of sample bias, as derived from the fitting procedure, is summarized in figure 4.32.

In the following, the origin of the different spectral components is discussed.

The long-wavelength emission (850nm-920nm) detected for low excitation bias is neither compatible with the intrinsic MgO emission nor with optical modes excited in the silver tip. Based on its distinct blue-shift and intensity decrease with increasing sample bias, the emission is assigned to tip-induced plasmons (TIPs). The Ag tip and the Mo sample are actively involved in TIP excitations, while the MgO film only acts as dielectric spacer in addition to the vacuum gap between tip and sample.

A distinct influence of the dielectric MgO layer on the TIP emission characteristic is revealed, however, from the spectra. The onset bias of 4.5V is unusually high for TIP-mediated emission, which starts at much lower voltages in pure metal-metal junctions [33,218]. Taking only energy conservation arguments into account, the onset is expected to be at 1.3V, when electrons have formally enough energy to excite the 900nm photons. The high onset bias in the present case is attributed to the absence of final states for inelastically tunneling electrons inside the MgO band gap. The excitation probability for TIP modes becomes relevant only when the inelastically tunneling electrons have enough energy to reach the MgO conduction band after an energy transfer to the TIP. From this consideration, the position of the conduction band edge can be determined from the difference between the onset bias and the TIP energy to be at 3.2eV. This value is verified by elastic tunneling spectroscopy, where a pronounced peak at 3.1eV marks the onset for electron transport into the MgO conduction band (figure 4.33a, dashed line). Assuming E_F to be in the midgap position, a total band gap of 6.4eV is deduced for the 12.5ML thick MgO film, which is smaller than the bulk value of 7.9eV [154,144].

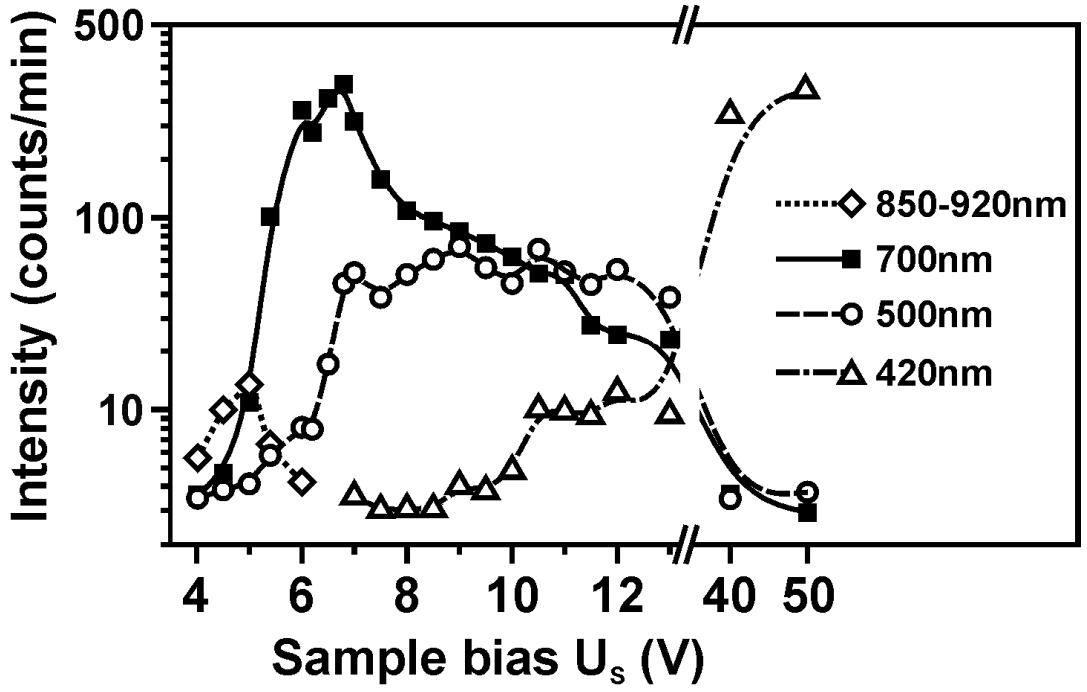

Figure 4.32: *Evolution of the emission intensity with excitation bias for selected wavelengths, derived from the deconvolution of the spectral series shown in figure 4.31.*

The emission peak at 700nm is not compatible with a TIP-mediated process, because neither its sharp intensity variation with sample bias, nor its constant peak position fit into the general picture of coupled plasmon modes. Its appearance falls into the bias regime, where field-emission resonances (FERs) start to control the electron transport between tip and sample. Typical conductance measurements of the Ag tip–MgO junction taken on an MgO terrace position are presented in figure 4.33a. As observed for the Au tip-MgO junction (sect. III.3.1), the conductance is characterized by oscillations due to transport via the FERs. Similar to the results for the Au tip, a shift of the FERs to higher energies is observed when measurements are done on a dislocation step region (data not shown here).

In contrast to the Au tip-MgO junction (sect. III.3.1), here the characteristic 700nm photon peak is clearly related to radiative electron transition from the 2nd to the 1st FER level. This conclusion is based on the following reasons: (i) According to dz/dU_s spectra, electron population of the 2nd FER and transition to the 1st level becomes possible at 5.5V-6.0V, in good agreement with the visibility onset of the 700nm peak. (ii) The energy separation between the 2nd and 1st FER amounts to approximately 1.6eV, which closely matches the

energy of the photon peak (1.7eV). (iii) The tip material affects only slightly the emission behavior, in contrast to the expectation of a TIP-mediated process. A pronounced emission peak of comparable wavelength (~750nm) was also detected for the Au–MgO junction (sect. III.3.1). (iv) The photon energy stays nearly constant when increasing the bias from 5.5V to more than 7.0V and moving the resonance conditions from the MgO terraces to dislocation step regions. It should be emphasized that the bias range for exciting the 700nm emission peak is mainly determined by variations in the FER energy position at different surface locations, such as terraces, steps, and dislocations. The intrinsic width of the FERs plays only a negligible role for the excitation bias range.

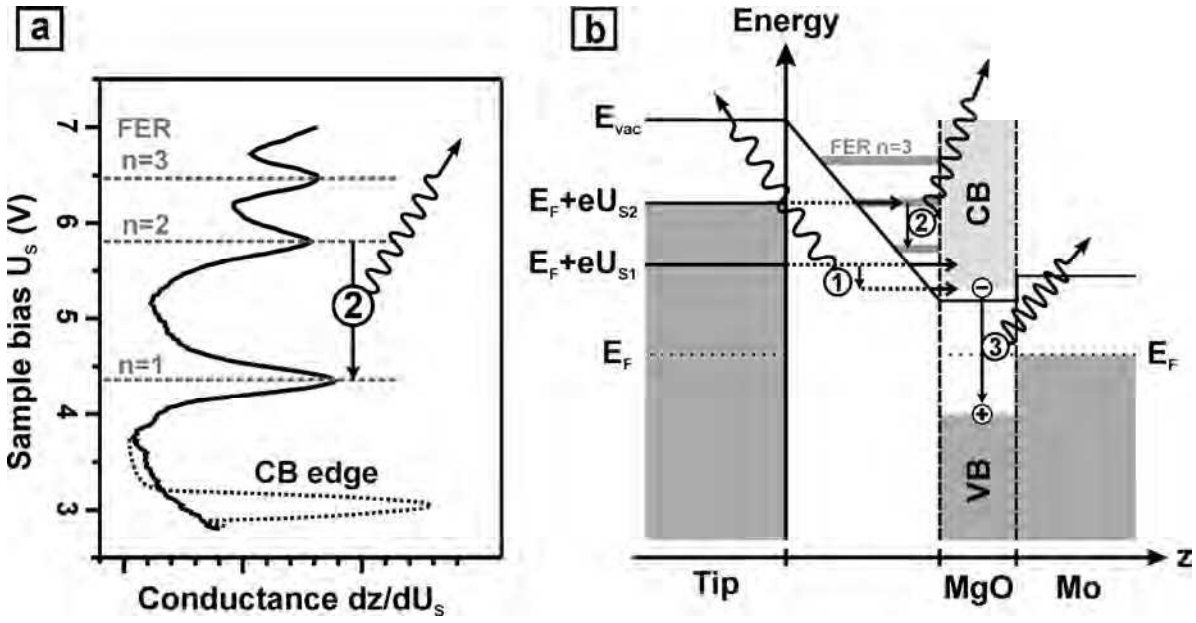

Figure 4.33: (a) *dz/dU_s spectra taken on top of a MgO terrace on Mo(001) (I = 50pA). While the maximum in the dashed curve marks the onset of the MgO conduction band, the solid line covers the range of the lower field-emission resonances.* ***(b)*** *Energy diagram of the Ag tip–MgO/Mo(001) junction. Different emission channels that might contribute to the photon signal from the junction are indicated for different sample bias U_s. Channel **1** corresponds to a TIP-mediated process involving inelastic electron tunneling. Channel **2** marks radiative transition between two field-emission resonances. Only transition from the 2nd to the 1st FER level is shown here. Channel **3** illustrates the radiative decay of an electron-hole pair. The change in tip-sample distance with bias voltage is omitted for clarity.*

The 700nm peak decreases sharply in intensity at bias voltages above 7V, when electrons from the tip cannot populate the 2nd FER any more. On the other hand, a step-like increase of the emission yield of 500nm photons is observed at 7V. This emission might be explained by

radiative transitions from the 3rd to the 1st FER level, which gives rise to an emission of 500nm (~2.47eV) photons, according to the level energies deduced from the dz/dU_s spectra. Besides, radiative transitions from the 3rd to the 2nd FER level leads to a photon emission at roughly 1500nm (~0.82eV). Since the spectral window of the optical system limit is at around 1000nm (chap. 2, sect. III.2), radiative transitions between 3rd and 2nd FER states cannot be detected. So, the 500nm emission line is at least partly assigned to the onset of radiative transitions from the 3rd to the 1st level. A distinct spectral signature, as revealed for the 2nd to 1st FER transition, is not observed in this bias range. The large width and small intensity of the 500nm peak might be owed to the short electron lifetime in the 3rd FER level. This is due, for instance, to easier electron penetration into the MgO film. The effect could be amplified due to the existence of competing decay channels like transitions to the 2nd FER level, coupling to TIP modes of similar energy, or enhanced scattering with electron-hole pairs in the Mo support. Only occasionally, transitions between the 3rd and 1st FER give rise to a pronounced emission peak as shown in figure 4.34. The morphological peculiarity of the MgO region that favors this particular recombination channel is not known.

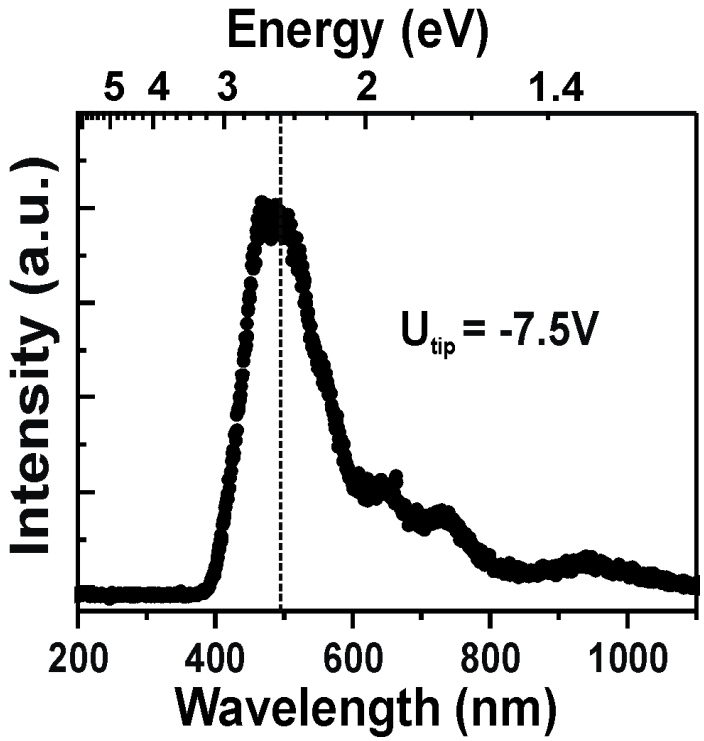

Figure 4.34: *Photon spectrum showing a high contribution of radiative electron transitions from the 3rd to 1st FER levels in the emission process from Ag tip–MgO junction. The electron current was set to 2nA, the accumulation time per spectrum to 120s.*

The 500nm emission peak could also be compatible with radiative TIP modes. Using the model described in chapter 1-section III.2.1, the TIP position for an Ag-Mo junction without MgO film is computed to be 355nm (3.5eV). The emission at 500nm (~2.47eV) peak would therefore be red-shifted by 1eV compared to the theoretical value. Such deviation is, however, expected from the influence of the MgO film on the plasmon position. The MgO dielectric layer formed by the MgO film increases the polarizability of the tip-sample cavity with respect to a vacuum gap (ε_{MgO}=10 versus ε_{Vac}=1) and shifts the TIP mode to lower energies. A similar behavior is well known for plasmon polaritons in metal particles that are embedded in a matrix with a high dielectric constant [12].

The emission line at around 420nm becomes only distinguishable at excitation voltages beyond 10V. It gradually shifts towards 400nm while developing into the dominant feature for excitation energies above 25eV, where the tip influence on the emission process can be excluded due to the macroscopic tip-sample separation. The position of the 400nm peak points to the intrinsic optical emission of the MgO film that has been assigned before to the radiative decay of excitons trapped at three-fold coordinated oxygen ions located at corners and kinks of the MgO surface (III.1.2). The visibility of the 400nm photon peak only for excitation energies above 10eV is not in conflict with an exciton-mediated light emission channel. The excitons are stimulated by impact ionization of valence-band states via the injected electrons, which require a minimum excitation energy of approximately 1.5 times the energy of the MgO surface bandgap, i.e., 1.5×6.2eV = 9.3eV (see chap.1, sect. III.3). High excitation cross-sections are only achieved at considerably higher impact energies, which suggest the importance of secondary processes, such as electron cascades and Auger decays, for the exciton stimulation (chap.1, sect. III.3).

In conclusion, the observed complex optical behavior of the Ag–MgO STM junction (figure 4.31**)** does not follow a single emission mechanism, but involves several channels that are active in different sample bias windows. These emission channels are schematically elucidated in figure 4.33.

IV. Conclusion

The relationship between the optical properties and the surface morphology of MgO thin films deposited on Mo(001) was investigated for different film thicknesses. As a first step, the film surface topography and crystallographic structure were explored using STM and Low Energy Electron Diffraction (LEED) as well as Grazing Incidence X-ray Diffraction (GIXD) techniques, respectively. The film morphology is found to depend on the number of MgO layers and passes through different stages with increasing thickness, whereby the MgO follows a layer-by-layer growth fashion. The stress resulting from the 5.3% mismatch between the MgO(001) and the Mo(001) lattices relaxes by inducing a periodic superstructure at the MgO/Mo interface. This relaxation structure consists of alternated flat and tilted mosaics involving the first 7ML of the MgO film. For film thicknesses around 12ML, the MgO topography starts to present new features, namely screw dislocations, MgO<100> oriented steps, and tilted planes. Flat and defect-poor MgO films were obtained for thicknesses higher than 25ML.

Using the Photon-STM, the optical properties of the MgO films were then analyzed by optical excitation with field-emitted or tunneling electron injection from the STM tip. In the field-emission excitation regime, the spectral distribution of the emitted light from differently thick MgO films are dominated by two emission bands located at 3.1eV and 4.4eV. These bands are assigned to the radiative decay of MgO excitons at 3-fold and 4-fold coordinated sites (corner, kinks, and step sites) and not at F-center sites for the following reasons: (i) Nucleation of Au particles at the low coordinated sites quenches the MgO optical signal, and (ii) creation or annihilation of F-centers in MgO surface does not alter the MgO emission bands. By performing optical excitation in the tunneling mode, different light emission mechanisms have been identified in an STM tip-MgO thin film junction, where Au and Ag tips were used. The onset of each mechanism is found to be dependent on the applied STM bias. At low sample bias, the optical response is determined by tip-induced plasmons that form between the noble metal tip and the Mo support and are weakly altered by the presence of the oxide layer. A dominant emission channel appears at bias voltages, at which electron transport in the junction is determined by field-emission resonances (FERs). Due to the insulating character of MgO, the FERs are sufficiently decoupled from the metal support to enable radiative electron transitions between higher and lower levels. A local increase of the MgO work function across the structural surface defects is deduced from the shift of the FER positions to higher energies. The optical signal related to excitons trapped at corners and kinks of the MgO surface are stimulated only by the injection of electrons at high sample bias, where the tip-sample distance is large. This results in a spatial resolution in the photon maps that is not better than 1nm, preventing the localization of the emission centers.

Summary and Outlook

Summary

The influence of the local morphological structure on the optical properties is studied using the Photon-STM for two systems: (1) Supported silver nanoparticle ensembles, and (2) MgO thin films deposited on Mo(001).

To study the influence of particle aspect ratio on the optical response to injected field-emitted electrons from the STM tip in Ag particle ensembles, dome- and disk-like particle ensembles with different densities were prepared on an alumina film grown on NiAl(110). The resonance energy of the excited Mie plasmon in the round Ag particle ensemble is found to shift to higher energies when the particle density increases. Such a shift is absent in the case of the disk-like particle ensemble, revealing an efficient electromagnetic coupling in ensembles of particles characterized by high aspect ratios. Besides, optical experiments were performed on ordered and disordered spherical Ag nanocolloids, prepared by a reverse micelle technique, on HOPG. The long-rang order of the size-selected Ag nanocolloids is found to weakly influence the Mie energy positions as compared to disordered ensembles.

In the thin MgO films grown on Mo(001), a periodic superstructure consisting of alternated flat and tilted mosaics generates at the MgO-Mo interface. This superstructure results from the relaxation of the stress caused by the 5.3% misfit between the MgO(001) and the Mo(001) lattice constants. The tiled mosaics gradually flatten with increasing the MgO thickness. The film surface levels off completely at thicknesses above 7ML. However, for a 12ML thick MgO film, other features, such as screw dislocations, tilted planes, and steps oriented along the <100> MgO directions, are clearly observed on the surface. These features are induced by the merging of relaxed MgO islands. Flat and defect-poor MgO films are only obtained for thickness above 25ML. The typical light emission spectra obtained from the MgO films are characterized by two emission bands located at 3.1eV and 4.4eV. Further experiments, namely, controlled Au nanoparticle nucleation and creation or removing of F-centers on the MgO surface, were performed to check the origin of the MgO optical response. The radiative exciton decay at the low coordinated sites in the MgO surface, such as steps, corners, and kinks, is deduced to be the source of the detected emitted light. The localization of the emission centers in the tunneling mode could not be achieved, since the intrinsic MgO emission is detected only for tunneling conditions where the spatial resolution is significantly reduced. Nevertheless, by performing spatially resolved optical measurements other light emission processes have been identified. These radiative mechanisms relate to tip-induced

plasmons excited in the cavity between the STM tip and the Mo support, and to radiative electron transitions between field-emission-resonance states that form in the STM tip-MgO film junction. The dependence of the latter process on the sample work function allowed the observation of a local increase of the MgO work function around the structural surface defects.

Future prospects

Although the initial aim of this work is essentially achieved, there are still some open points, which should be investigated in the future in order to reach better understandings, especially concerning the optical properties of the MgO/Mo(001) system.

Two prospects for future experiments are listed in the following:

- *Determination of the light emission centers in the MgO surface:* Two possible experiments may elucidate this point. (i) Perform atomically resolved optical measurements in the low bias regime, and create excitons by applying short pulses of high bias. The pulsed bias should be larger than the MgO bandgap to be able to create excitons, and the pulse duration has to be shorter than the response time of the STM feedback loop to avoid tip crashes or unwanted changes in the STM junction. (ii) Use of another simple oxide that is characterized by a smaller bandgap to enable exciton creation at much smaller excitation voltages than in case of MgO. A potential candidate for such an experiment is barium oxide (BaO), which has a bandgap[*] of around 4eV, corresponding to half the MgO bandgap.

- *Identification of the stoichiometry of the MgO surface structural-defects:* As noticed in this work, the local MgO work function is found to increase when going from a flat terrace to screw dislocation or dislocation step regions. This fact is tentatively traced back to local nonstoichiometry in these regions while no evidence is provided. Atomically resolved STM measurements of these defects in conjunction with DFT calculations might give better information on this point.

[*] R. J. Zollweg. *"Optical Absorption and Photoemission of Barium and Strontium Oxides, Sulfides, Selenides, and Tellurides"*. Phys. Rev. **111** (1958)113.

Bibliography

[1] N.V. Tkachenko. *"Optical Spectroscopy, Methods and Instrumentations"*. Elsevier, Amsterdam 2006.

[2] G. Binnig, H. Rohrer, Ch. Gerber, E. Weibel. *"Tunneling through a Controllable Vacuum Gap"*. *Appl. Phys. Lett.* **40**, (1982) 178.

[3] R. Berndt in: R. Wiesendanger, editor, *"Scanning Probe Microscopy and Spectroscopy: Analytical methods"*. Springer-Verlag, Berlin, Heidelberg, 1998, p 97.

[4] M. Yamashita, H. Shigekawa, and R. Morita. *"Mono-Cycle Photonics and Optical Scanning Tunneling Microscpy"*. Springer-Verlag Berlin Heidelberg, 2005.

[5] E. Betzig, J. K. Trautman, T. D. Harris, J. S. Weiner, and R. L. Kostelak. *"Breaking the Diffraction Barrier: Optical Microscopy on a Nanometric Scale"*. Science **251** (1991) 1468.

[6] N. Nilius, N. Ernst, H.-J. Freund.*"Photon Emission Spectroscopy of Individual Oxide-Supported Silver Clusters in a Scanning Tunneling Microscope"*. Phys. Rev. Lett. **84** (1992) 3994.

[7] U. Håkanson, M.K. Johansson, M. Holm, C. Pryor, L. Samuelson, W. Seifert. *"Photon Mapping of Quantum Dots using a Scanning Tunneling Microscope"*. Appl. Phys. Lett. **81** (2002) 4443.

[8] H. X. Qui, G.V. Nazin, W. Ho. *"Vibrationally Resolved Fluorescence Excited with Submolecular Precision"*. Science **299** (2003) 542.

[9] E. Cavar, M.-C. Blüm, M. Pivetta, F. Patthey, M. Chergui, W.D. Schneider. *"Fluorescence and Phosphorescence from Individual C60 Molecules Excited by Local Electron Tunneling"*. Phys. Rev. Lett. **95** (2005) 196102.

[10] B. Pettinger.*"Surface-Enhanced Raman Scattering – Physics and Applications"*. Topics Appl. Phys. **103** (2006) 217.

[11] D.L. Feldheim, C.A. Foss, Jr. in *"Metal Nanoparticles: Synthesis, Characterization, and Apllications"*. Marcel Dekker, New York 2001.

[12] U. Kreibig, W. Vollmer. *"Optical Properties of Metal Clusters"*, Springer Series Materials Science, vol. **25**, Springer, Berlin, 1995.

[13] G. Schmid. *"Nanoparticles: From Theory to Application"*. Wiley-VCH, Verlag-Weinheim, 2004.

[14] Y. Dirix, C. Bastiaansen, W. Caseri, P. Smith. *"Oriented Pearl-Necklace Arrays of Metallic Nanoparticles in Polymers: A New Route toward Polarization-Dependent Color Filters"*. Adv. Mater. **11** (1999) 223.

[15] S.A. Maier, P.G. Kik, H.A. Atwater, S. Meltzer, E. Harel, B.E. Koel, A.A.G. Requicha. *"Local Detection of Electromagnetic Energy Transport below the Diffraction Limit in Metal Nanoparticle Plasmon Waveguides"*. Nat. Mater. **2** (2003) 229.

[16] M. Quinten, A. Leitner, J.R. Krenn, F.R. Aussenegg. *"Electromagnetic Energy Transport via Linear Chains of Silver Nanoparticles"*. Opt. Lett. **23** (1998) 1331.

[17] K. Kneipp, Y. Wang, H. Kneipp, L.T. Perelman, I. Itzkan, R.R. Dasari, M.S. Feld. *"Single Molecule Detection Using Surface-Enhanced Raman Scattering (SERS)"*. Phys. Rev. Lett **78** (1997) 1667.

[18] H.-J. Freund, M. Baümer, H. Kuhlenbeck. *"Catalysis and Surface Science: What do we Learn from Studies of Oxide-Supported Cluster Model Systems?"*. Adv. Catal. 45 (2000) 333.

[19] K. Watanabe, Y. Matsumoto, M. Kampling, K. Al-Shamery, H.-J. Freund. *"Photochemistry of Methane on Pd/Al2O3 Model Catalysts: Control of Photochemistry on Transition Metal Surfaces"*. Angew. Chem. Int. Ed. **38** (1999) 2192.

[20] H.-J. Freund. *"Introductory Lecture: Oxide Surfaces"*. Farad. Disc. **114** (1999) 1.

[21] V.E. Henrich. *"The Chemical Physics of Solid Surfaces: Oxide Surfaces"*, Vol. **9**. Edited by D.P. Woodruff. Elsevier, Amsterdam 2001.

[22] M. Anpo, Y. Yamada, Y. Kubokawa, S. Coluccia, A. Zecchina, M. Che. *"Photoluminescence Properties of MgO Powders with Coordinatively Unsaturated Surface Ions"*. J. Chem. Soc., Faraday Trans. 1 **vol 84** (1988) 751.

[23] S. Stankic, M. Müller, O. Diwald, M. Sterrer, E. Knözinger, J. Bernardi. *"Size-Dependent Optical Properties of MgO Nanocubes"*. Angew. Chem. Int. Ed. **44** (2005) 4917.

[24] G. Pacchioni. *"The Chemical Physics of Solid Surfaces: Oxide Surfaces"*, Vol. **9**. Edited by D.P. Woodruff. Elsevier, Amsterdam 2001.

[25] R. Hacquart, J.-M. Krafft, G. Costentin, J. Jupille. *"Evidence for Emission and Transfer of Energy from Excited Edge Sites of MgO Smokes by Photoluminescence Experiments"*. Surf. Sci. **595** (2005) 172.

[26] A.L. Shluger, P.V. Sushko, L.N. Kantorovich. *"Spectroscopy of Low-Coordinated Sites: Theoretical Study of MgO"*. Phys. Rev. B **53** (1999) 2417.

[27] G. Binnig, H. Rohrer. *"Scanning Tunneling Microscopy: From Birth to Adolescence"*. Nobel Lecture, 1986. http://nobelprize.org/nobel_prizes/physics/laureates/1986/binnig-lecture.pdf

[28] R. Wiesendanger, editor, *"Scanning Probe Microscopy and Spectroscopy: Methods and Applications"*. Cambridge University Press, Cambridge, 1994.

[29] R. Wiesendanger, editor, *"Scanning Probe Microscopy and Spectroscopy: Analytical Methods"*. Springer-Verlag, Berlin, Heidelberg, 1998.

[30] C.J. Chen, *"Introduction to Scanning Tunneling Microscopy"*. Oxford University Press, New York, Oxford, 1993.

[31] R. M. Feenstra, W. A. Thompson, and A. P. Fein. *"Real-Space Observation of π-bonded Chains and Surface Disorder on Si(111)2×1"*. Phys. Rev. Lett. **56** (1986) 608.

[32] J.K. Gimzewski, B. Reihl, J.H. Coombs, R.R. Schlittler. *"Photon Emission with the Scanning Tunneling Microscope"*. Z. Phys. B – Condensed Matter **72** (1988) 497.

[33] R. Berndt, J. K. Gimzewski, P. Johansson. *"Inelastic Tunneling Excitation of Tip-Induced Plasmon Modes on Noble-Metal Surfaces"*. Phys. Rev. Lett. **67** (1991) 3796.

[34] R. Wiesendanger, H. J. Güntherodt, G. Güntherodt, R. J. Gambino and R. Ruf. *"Observation of Vacuum Tunneling of Spin-Polarized Electrons with the Scanning Tunneling Microscope"*. Phys. Rev. Lett. 65 (1990) 247.

[35] R. Wiesendanger, I.V. Shvets, D. Bürgler, G. Tarrach, H. J. Güntherodt, J.M.D. Coey and S. Gräser. *"Topographic and Magnetic-Sensitive Scanning Tunneling Microscope Study of Magnetite"*. Science **255 (**1992) 583.

[36] M. Bode. *"Topographic and Magnetic-Sensitive Scanning Tunneling Microscope Study of Magnetite"*. Rep. Prog. Phys. **66** (2003) 523.

[37] B. C. Stipe, M. A. Rezaei, and W. Ho. *"Single-Molecule Vibrational Spectroscopy and Microscopy"*. Science **280 (**1998) 1732.

[38] B. Pettinger, B. Ren, G. Picardi, R. Schuster and G. Ertl. *"Nanoscale Probing of Adsorbed Species by Tip-Enhanced Raman Spectroscopy"*. Phys. Rev. Lett. 92 (2004) 096101.

[39] R.M. Stöckle, Y.D. Suh, V. Deckert and R. Zenobi. *"Nanoscale Chemical Analysis by Tip-Enhanced Raman Spectroscopy"*. Chem. Phys. Lett. **318** (2000) 131.

[40] M. F. Crommie, C. P. Lutz, and D. M. Eigler. "*Imaging Standing Waves in a Two-Dimensional Electron Gas"*. Nature, **363** (1993) 524.

[41] M. F. Crommie, C.P. Lutz, and D. M. Eigler. "*Confinement of Electrons to Quantum Corrals on a Metal Surface"*. Science, **262** (1993) 218.

[42] N. Nilius, T. M. Wallis, and W. Ho. *"Development of One-Dimensional Band Structure in Artificial Gold Chains"*. Science, **297 (**2002**)** 1853.

[43] M. Bäumer, H.-J. Freund. *"Metal Deposits on Well-Ordered Oxide Films"*. Prog. Surf. Sci. **61** (1999) 127.

[44] M. Roßler, P. Geng, J. Wintterlin. *"A High-Pressure Scanning Tunneling Microscope for Studying Heterogeneous Catalysis"*. Rev. Sci. Instrum. 76 (2005) 023705.

[45] H.-J. Freund. *"Metal-supported ultrathin Oxide Film Systems as Designable Catalysts and Catalyst Supports"*. Surf. Sci. **601** (2007) 1438.

[46] K. Itaya. "*In situ Scanning Tunneling Microscopy in Electrolyte Solutions*". Prog. Surf. Sci. **58** (1998) 121.

[47] N.J. Tao, C.Z. Li, and H.X. He. *"Scanning Tunneling Microscopy Applications in Electrochemistry — Beyond Imaging"*. J. Electroanal. Chem. **492** (2000) 81.

[48] D. Friebel, C. Schlaup, P. Broekmann and K. Wandelt. *"Sulfidation of a Cu Submonolayer at the Au(1 1 1)/Electrolyte Interface – An in situ STM Study"*. Surf. Sci. **600** (2006) 2800.

[49] P. G. Arscott, G. Lee, V. A. Bloomfield, and D. F. Evan. *"Scanning Tunneling Microscopy of Z-DNA"*. Nature **339** (1989) 484.

[50] T.P. Beebe Jr, T.E. Wilson, D.F. Ogletree, J.E. Katz, R. Balhorn, M.B. Salmeron, and W.J. Siekhaus. *"Direct Observation of Native DNA Structures with the Scanning Tunneling Microscope"*. Science 243 (1989) 370.

[51] M.Q. Li. *"Scanning Probe Microscopy (STM/AFM) and Applications in Biology"*. Appl. Phys. A **68** (1999) 255.

[52] K. Tomatsu, K. Nakatsuji, T. Iimori, Y. Takagi, H. Kusuhara, A. Ishii, F. Komori. *"An Atomic Seesaw Switch Formed by Tilted Asymmetric Sn-Ge Dimers on a Ge (001) Surface"*. Science **315** (2007) 1696.

[53] P. Liljeroth, J. Repp, G. Meyer. "*Current-Induced Hydrogen Tautomerization and Conductance Switching of Naphthalocyanine Molecules"*. Science **317** (2007) 1203.

[54] J. Bardeen. "*Tunneling from a Many-Particle Point of View*". Phys. Rev. Lett. **6** (1961) 57.

[55] J. Tersoff, D.R. Hamann. *"Theory and Application for the Scanning Tunneling Microscope"*. Phys. Rev. Lett. **50** (1983) 1998.

[56] J. Tersoff, D.R. Hamann. "*Theory of the Scanning Tunneling Microscope"*. Phys. Rev. B **31** (1985) 805.

[57] C.J. Chen. *"Origin of Atomic Resolution on Metal Surfaces in Scanning Tunneling Microscopy"*. Phys. Rev. Lett. 65 (1990) 448.

[58] R.J. Hamers. *"Atomic-Resolution Surface Spectroscopy with The Scanning Tunneling Microscope"*. Annu. Rev. Phys. Chem. **40** (1989) 531.

[59] H. Ibach, *Physics of Surfaces and Interfaces*, Springer-Verlag Berlin Heidelberg, 2006.

[60] F. Bechstedt, *Principles of Surface Physics*, Springer-Verlag Berlin Heidelberg, 2003.

[61] M.W. Cole, M.H. Cohen. *"Image-Potential-Induced Surface Bands in Insulators"*. Phys. Rev. Lett. **23** (1969) 1238.

[62] P.M. Echnique, J.B. Pendry. *"The Existence and Detection of Rydberg States at Surfaces"*. J. Phys. C. Solid State Phys. **11** (1978) 2065.

[63] E.G. McRae. *"Electronic Surface Resonances of Crystals"*. Rev. Mod. Phys. 51 (1979) 541.

[64] D. Straub, W. Altmann, H. Scheidt, and V. Dose. "*Summary Abstract: Intrinsic unoccupied Surface States of GaP(110)"* . J. Vac. Sci. Technol. A **2** (1984) 529.

[65] V. Dose, W. Altmann, A. Goldmann, U. Kolac, and J. Rogozik. *"Image-Potential States Observed by Inverse Photoemission"*. Phys Rev. Lett. 52 (1984) 1919.

[66] U. Höfer, I.L. Shumay, Ch. Reuß, U. Thomann, W. Wallauer, Th. Fauster. *"Time-Resolved Coherent Photoelectron Spectroscopy of Quantized Electronic States on Metal Surfaces"*. Science **277** (1997) 1480.

[67] A.G. Borisov, J.P. Gauyacq, A.K. Kazansky, E.V, Chulkov, Y.M. Silkin, P.M. Echnique. *"Long-Lived Excited States at Surfaces: Cs/Cu(111) and Cs/Cu(100) Systems"*. Phys. Rev. Lett. **86** (2001) 488.

[68] S. Yang, R.A. Bartynski, G.P. Kochanski, S. Papadia, T. Fondén, M. Persson. "*Surface Barrier Resonances on a Simple Metal"*. Phy. Rev. Lett. **70** (1993) 849.

[69] S. Link, H.A. Dürr, W. Eberhardt. "*Lifetimes of Image-Potential States on the Pt(111) Surface probed by Time-Resolved Two-Photon Photoemission Spectroscopy"*. Appl. Phys. A **71** (2000) 525.

[70] G. Binning, K.H. Frank, H. Fuchs, N. Garcia, B. Reihl, H. Rohrer, F. Salvan, A.R. Williams. *"Tunneling Spectroscopy and Inverse Photoemission: Image and Field States"*. Phys. Rev. Lett. 55 (1985) 991.

[71] M. Pivetta, F. Patthey, M. Stengel, A. Baldereschi, W.-D. Schneider. *"Local Work Function Moiré Pattern on Ultrathin Ionic Films: NaCl on Ag(100)"*. Phys. Rev. B **72** (2005) 115404.

[72] K.H. Gundlach. *"Zur Berechnung des Tunnelstroms durch eine Trapezförmige potentialstuffe"*. Solid-State Electronics **9** (1966) 949.

[73] O.Yu. Kolesnyschenko,, Yu. A. Kolensischenko, O.I. Shklyarevskii, H. van Kempen. *"Field-Emission Resonance Measurements with Mechanically Controlled Break Junctions"*. Physica B **291** (2000) 246.

[74] R.H. Fowler, L. Nordheim. *"Electron Emission in Intense Electric Fields"*. Proc. Roy. Soc. A **119** (1928) 173

[75] R. Gomer, *Field Emission and Field Ionization*, Harvard University Press, Cambridge, Massachusetts, 1961.

[76] J.M. Pitarke, F. Flores, P.M. Echnique. *"Tunneling Spectroscopy: Surface Geometry and Interface Potenital Effects"*. Surf. Sci. **234** (1990) 1.

[77] E.D.L. Rienks, N. Nilius, H.-P. Rust, H.-J. Freund. *"Surface Potential of a Polar Oxide Film: FeO on Pt(111)"*. Phys. Rev. B **71** (2005) 241404.

[78] J.A. Kubby, W.J. Greene. *"Particle in a Variable-Size Box: The Influence of the Tip in thin-Film Electron Interferometry"*. Phys. Rev. B **48** (1993) 11249.

[79] G.V. Nazin, X.H. Qiu, and W. Ho. *"Atomic Engineering of Photon Emission with a Scanning Tunneling Microscope"*. Phys. Rev. Lett. **90** (2003) 216110-1.

[80] G. Hoffmann, T. Maroutian, R. Berndt. *"Color View of Atomic Highs and Lows in Tunneling Induced Light Emission"*. Phys. Rev. Lett. **93** (2004) 076102-1.

[81] P. Johansson, R. Berndt. *"Theory for Photon Emission from a Scanning Tunneling Microscope"*. Z. Phys. B – Condensed Matter **84** (1991) 269

[82] J. Aizpurua, S.P. Apell, R. Berndt. *"Role of Tip Shape in Light Emission from the Scanning Tunneling Microscope"*. Phys. Rev. B **62** (2000) 2065.

[83] R. Berndt, J.K. Gimzewski, P. Johansson. *"Electromagnetic Interactions of Metallic Objects in Nanometer Proximity"*. Phys. Rev. Lett. **71** (1993) 3493.

[84] G. Hoffmann, J. Aizpurua, P. Apell, R. Berndt. *"Influence of Tip Geometry in Light Emission from The Scanning Tunneling Microscope*". Surf. Sci. **482-485** (2001) 1159.

[85] K. Meguro, K. Sakamoto, R. Arafune, M. Satoh, S. Ushioda. *"Origin of Multiple Peaks in The Light Emission Spectra of a Au(111) surface induced by The Scanning Tunneling Microscope"*. Phys. Rev. B. **65** (2002) 165405.

[86] R. Berndt, J.K. Gimzewski. *"Isochromat Spectroscopy of Photons Emitted from Metal Surfaces in an STM"*. Ann. Physik **2** (1993) 133.

[87] G. Hoffmann, J. Kliewer, R. Berndt. *"Luminescence from Metallic Quantum Wells in a Scanning Tunneling Microscope"*. Phys. Rev. Lett. **87** (2001) 176803-1.

[88] B.N.J. Persson, A. Baratoff. "*Theory of Photon Emission in Electron Tunneling to Metal Particles*". Phys. Rev. Lett. **68** (1992) 3224.

[89] N. Nilius, N. Ernst, H.-J. Freund. "*Tip influence on plasmon excitations in single gold particles in an STM*". Phys. Rev. B **65** (2002) 115421.

[90] G. Mie, *"Beiträge zur Optik trüber Medien, speziell kolloidaler Metallösungen"*. Ann. Phys. (Leipzig) **25**, 377 (1908).

[91] I. Simonsen, R. Lazzari, J. Jupille, S. Roux."*Numerical modeling of the optical response of supported metallic particles*". Phys. Rev. B. **61** (2000) 7722.

[92] C. A. Foss, Jr., G.L. Hornyak, J.A. Stockert, CR. Martin. "*Template-Synthesized Nanoscopic Gold Particles: Optical Spectra and the Effects of Particle Size and Shape*". J. Phys. Chem. 98 (1994) 2963.

[93] P. Schmidt, R. Berndt. "*Ultraviolet Light Emission from Si in a Scanning tunneling Microscope*". Phys. Rev. Lett. **99** (2007) 246103.

[94] S.F. Alvarado, Ph. Renaud, D.L. Abraham, Ch. Schönenberger, D.J. Arent. "*Luminescence in Scanning Tunneling Microscopy on III-V nanostructures*". J. Vac. Sci. Technol. B **9** (1991) 409.

[95] R.C. Alig, S. Bloom, C. Struck. "*Scattering by Ionization and Phonon Emission in Semiconductors*". Phys. Rev. B **22** (1980) 22.

[96] R. Berndt, J.K. Gimzewski. "*Injection Luminescence from CdS$(11\bar{2}0)$ studied with Scanning Tunneling Microscopy*". Phys. Rev. B **45** (1992) 1495.

[97] A. Downes, M.E. Welland. "*Photon Emission from Si(111)-(7×7) Induced by Scanning Tunneling Microscopy: Atomic Scale and Material Contrast*". Phys. Rev. Lett. **81** (1998) 1857.

[98] C. Thirstrup, M. Sakurai, K. Stokbro, M. Aono. "*Visible Light Emission from Atomic Scale Patterns Fabricated by Scanning Tunneling Microscope*". Phys. Rev. Lett. **82** (1999) 1241.

[99] M. Sakurai, C. Thirstrup, M. Aono. "*Optical Selection Rules in Light Emission from the Scanning Tunneling Microscope*". Phys. Rev. Lett. **93** (2004) 046102.

[100] K. Besocke. "*An easily Operable Scanning Tunneling Microscope*". Surf. Sci. **181** (1987) 145.

[101] I. Horcas, R. Fernandez, J.M. Gomez-Rodriguez, J. Colchero, J. Gomez-Herrero , A. M. Baro. "*WSXM: A Software for Scanning Probe Microscopy and a Tool for Nanotechnology*". Rev. Sci. Instrum. 78, 013705 (2007).

[102] N. Nilius, "*Lichtemission aus einzelnen oxidgetragenen Metallpartikeln im Raster-tunnelmikroskop*", Thesis, Humboldt-Universität zu Berlin, Berlin (2001).

[103] M.-P. Pileni. "*Nanosized Particles Made in Colloidal Assemblies*". Langmuir **13** (1997) 3266.

[104] M.-P. Pileni in "*Metal Nanoparticles: Synthesis, Characterization, and Apllications*". Marcel Dekker, New York 2001.

[105] Y. Lu, G. L. Liu, L. P. Lee. *"High-Density Silver Nanoparticle Film with Temperature-Controllable Interparticle Spacing for a Tunable Surface Enhanced Raman Scattering Substrate"*. Nano Lett. **5** (2005) 5.

[106] R.M. Jaeger, H. Kuhlenbeck, H.-J. Freund, M. Wuttig, W. Hoffmann, R. Franchy, H. Ibach. *"Formation of a well-ordered Aluminum Oxide Overlayer by Oxidation of NiAl(110)"*. Surf. Sci. **259** (1991) 235.

[107] G. Kresse, M. Schmid, E. Napetschnig, M. Shishkin, L. Köhler, P. Varga. *"Structure of the Ultrathin Aluminum Oxide Film on NiAl(110)"*. Science **308** (2005) 1440.

[108] S. Ulrich, N. Nilius, H.-J. Freund. *"Growth of thin Alumina Films on a Vicinal NiAl Surface"*. Surf. Sci. **601** (2007) 4603.

[109] M. Kulawik, N. Nilius, H.-P. Rust, H.-J. Freund. *"Atomic Structure of Antiphase Domain Boundaires of a thin Al_2O_3 Film on NiAl(110)"*. Phy. Rev. Lett. **91** (2003) 256101.

[110] N. Nilius, M. Kulawik, H.-P. Rust, H.-J. Freund. *"Defect-induced Gap States in Al_2O_3 thin films on NiAl(110)"*. Phys. Rev. B **69** (2004) 121401.

[111] C. R. Henry.*"Morphology of Supported Nanoparticles"*.. Prog. Surf. Sci. **80** (2005) 92.

[112] C.T. Campbell. *"Ultrathin Metal Films and Particles on Oxide Surfaces: Structural, Electronic and Chemisorptive Properties"*. Surf. Sci. Rep. 27 (1997) 1.

[113] F. Silly, M.R. Castell. *"Selecting the Shape of Supported Metal Nanocrystals: Pd Huts, Hexagons, or Pyramids on $SrTiO_3(001)$"*. Phys. Rev. Lett. **94** (2005) 046103.

[114] G. Wulff.*"Zur Frage der Geschwindigkeit des Wachstums und der Auflösung der Krystallflachen."* Z. Kristallogr. Mineral. **34** (1901) 449.

[115] R. Lazzari, I. Simonsen. *"GranFilm: A Software for Calculating thin-Layer Dielectric Properties and Fresnel Coefficients"*. Thin Solid Films **419** (2002) 124.

[116] J.W. Little, T.A. Callcott, T.L. Ferrell, E.T. Arakwa. *"Surface Plasmon Radiation from Ellipsoidal Silver Spheroids"*. Phys. Rev. B **29** (1984) 1606.

[117] K.-H. Su, Q.-H. Wei, X. Zhang, J.J. Mock, D.R. Smith, S. Schultz. *"Interparticle Coupling Effects on Plasmon resonances of Nanogold Particles"*. Nano Lett. **3** (2003) 1087.

[118] C.L. Haynes, A.D. McFarland, L. Zhao, R.P. Van Duyne, G.C. Schatz, L. Gunnarsson, J. Prikulis, B. Kasemo, M. Käll. *"Nanoparticle Optics: The Importance of Radiative Dipole Coupling in Two-Dimensional Nanoparticle Arrays"*. J. Phys. Chem. B **107** (2003) 7337.

[119] W. Rechberger, A Hohenau, A. Leitner, J.R. Krenn, B. Lamprecht, F.R. Ausseneg. *"Optical Properties of two interacting Gold Nanoparticles"*. Opt. Commu. **220** (2003) 137.

[120] I. Simonsen, R. Lazzari, J. Jupille, S. Roux. *"Numerical Modeling of the Optical Rsponse of Supported Metallic Particles."* Phys. Rev. B **61** (2000) 7722.

[121] E.D. Palik (Ed.). *"Handbook of Optical Constants of Solids."* Academic Press, Orlando, 1985.

[122] A. Taleb, C. Petit, M.-P. Pileni. *"Synthesis of Highly Monodispersed Silver Nanoparticles from AOT Reverse Micelles: A way to 2D and 3D Self-Organization"*. Chem. Mater. **9** (1997) 950.

[123] F. Silly, A.O. Gusev, A. Taleb, F. Charra, M.-P. Pileni. *"Coupled Plasmon Modes in an Ordered Hexagonal Monolayer of Metal Nanoparticles: A direct observation"*. Phys. Rev. Lett. **84** (2000) 5840.

[124] N. Pinna, M. Maillard, A. Courty, V. Russier, M. P. Pileni. *"Optical Properties of Silver Nanocrystals Self-Organized in a Two-Dimensional Superlattice: Substrate Effect"*. Phys. Rev. B **66** (2002) 45415.

[125] V. Russier, M.P. Pileni. *"Optical Absorption Spectra of Arrays of Metal Particles from Cluster Calculations: Cluster Size and Shape Effects"*. Surf. Sci. **425** (1999) 313.

[126] L. Bergmann, C. Schäfer (Eds.). *"Lehrbuch der Experimentalphysik: Optik"*, **vol. 3**, de Gruyter, Berlin, 1966.

[127] A. Taleb, V. Russier, A. Courty, M.P. Pileni. *"Collective Optical Properties of Silver Nanoparticles Organized in Two-Dimensional Superlattices"*. Phys. Rev. B **59** (1999) 13350.

[128] H. Hövel, S. Fritz, A. Hilger, U. Kreibig, M. Vollmer. *"Width of Cluster Plasmon Resonances: Bulk Dielectric Functions and Chemical Interface Damping"*. Phys. Rev. B **48** (1993) 18178.

[129] M. Henyk, K.M. Beck, M.H. Engelhard, A.G. Joly, W.P. Hess, J.T. Dickinson. *"Surface Electronic Properties and Site-specific Laser Desorption Processes of Highly Structured Nanoporous MgO thin Films"*. Surf. Sci. **593** (2005) 242.

[130] C. Tegenkamp, H. Pfnür, W. Ernst, U. Malaske, J. Wollschläger, D. Peterka, K.M. Schröder, V. Zielasek, M. Henzler. *"Defects in Epitaxial Insulating Thin Films"*. J. Phys. Cond. Mat. **11** (1999) 9943.

[131] S. Colluccia. A. Barton. A.J. Tench. *"Reactivity of Low-Coordination Sites on the Surface of Magnesium Oxide"*. J. Chem. Soc. Faraday Trans. 1 vol **77** (1981) 2203.

[132] H. Hattori. *"Solid Base Catalysts: Generation of Basic Sites and Application to Organic Synthesis"*. Appl. Catal. A: General **222** (2001) 247.

[133] M.-L. Bailly, C. Chizallet, G. Costentin, J.-M. Krafft, H. Lauron-Pernot, M. Che. *"A Spectroscopy and Catalysis Study of The Nature of Active Sites of MgO Catalysts: Hermodynamic Brønsted Basicity versus Reactivity of Basic Sites"*. J. Catal. **235** (2005) 413.

[134] S. Abbet, A. Sanchez, U. Heiz, W.-D. Schneider, A. M. Ferrari, G. Pacchioni, N. Rösch. *"Acetylene Cyclotrimerization on Supported Size-Selected Pd_n Clusters ($1 \leq n \leq 30$): One Atom Is Enough!"*. J. Am. Chem. Soc. **122** (2000) 3453.

[135] O. Meerson, G. Sitja, and C.R. Henry. *"Low Temperature and Low Pressure CO Oxidation on Gold Clusters Supported on MgO(100)"*. Eur. Phys. J. D **34**, (2005) 119.

[136] B. Yoon, H. Häkkinen, U. Landman, A.S. Wörz, J.-M.Antonietti, S. Abbet, K. Judai, U. Heiz. *"Charging Effects on Bonding and Catalyzed Oxidation of CO on Au_8 Clusters on MgO"*. Science **307** (2005) 403.

[137] B. Hammer. *"Special Sites at Noble and Late Transition Metal Catalysts"*. Top. Catal. **37** (2006) 3.

[138] A.M. Volodin. *"Photoinduced Phenomena on The Surface of Wide-Band-Gap Oxide Catalysts"*. Catal. Today **58** (2000) 103.

[139] S. Yuasa, T. Nagahama, A. Fukushima, Y. Suzuki, K. Ando. *"Giant Room-Temperature Magnetoresistance in Single-Crystal Fe/Mgo/Fe Magnetic Tunnel Junctions"*. Nature Materials **3** (2004) 868.

[140] P.G. Mather, J.C. Read, R.A. Buhrman. *"Disorder, Defects, and Band Gaps in Ultrathin (001) MgO Tunnel Barrier Layers"*. Phys. Rev. B **73** (2006) 205412.

[141] T. Sakaguchi, H. Choi, A. Sung-Jin, T. Sugimura, M. Park, M.Oogane, H. Oh, J. Hayakawa, S. Ikeda, Y.M.Lee2, T. Fukushima, T. Miyazaki, H. Ohno, M. Koyanagi. *"Fabrication and Evaluation of Magnetic Tunnel Junction with MgO Tunneling Barrier"*. Jpn. J. Appl. Phys. **45** (2006) 3228.

[142] M. Yamamoto et al. *"Highly Spin-Polarized Tunneling in Fully Epitaxial Magnetic Tunnel Junctions with a Co-Based Full-Heusler Alloy Thin Film and a MgO Barrier"*. In the book series: *"Advances in Solid State Physics"*. Springer Berlin / Heidelberg, 2008.

[143] G. Pacchioni. *"The Chemical Physics of Solid Surfaces: Oxide Surfaces"*, Vol. **9**. Edited by D.P. Woodruff. Elsevier, Amsterdam 2001.

[144] V.E. Henrich, G. Dreselhaus, H.J. Zeiger. *"Energy-Dependent Electron-Energy-Loss Spectroscopy: Application to The Surface and Bulk Electronic Structure of MgO"*. Phys. Rev. B **22** (1980) 4764.

[145] E. Knözinger, K.-H. Jacob, S. Singh, P. Hofmann. *"Hydroxyl Groups as IR Active Surface Probes on MgO Crystallites"*. Surf. Sci. **290** (1993) 388.

[146] G. Spoto, E.N. Gribov, G. Ricchiardi, A. Damin, D. Scarano, S. Bordiga, C. Lamberti, A. Zecchina. *"Carbon Monoxide MgO from Dispersed Solids to Single Crystals: A Review and New Advances"*. Prog. Surf. Sci. **76** (2004) 71.

[147] Y.D. Kim, J. Stultz, D.W. Goodman. *"Identification of Defect Sites on MgO(100) Surfaces"*. Langmuir **18** (2002) 3999.

[148] M. Sterrer, E. Fischbach, M. Heyde, N. Nilius, H.-P. Rust, T. Risse, H.-J. Freund. *"Electron Paramagnetic Resonance and Scanning Tunneling Microscopy Investigations on the Formation of F^+ and F^0 Color Centers on the Surface of Thin MgO(001) Films"*. J. Phys. Chem. B **110** (2006) 8665.

[149] K.J. Caulfield, R. Cooper, J.F. Boas. *"A Temperature Effect in the Luminescence Emission from Electron-Irradiated MgO"*. J. Chem. Phys. **92** (1990) 6441.

[150] S. Collucia, A.M. Dean, A.J. Tench. *"Photoluminescence Spectra of Surface States in Alkaline Earth Oxides"*. J**.** Chem. Soc., Faraday Trans. 1 **vol. 74** (1978) 2913.

[151] O. Diwald, M. Sterrer, E. Knözinger, P.V. Suchko, A.L. Shluger. *"Wavelength Selective Excitation of Surface Oxygen Anions on Highly Dispersed MgO"*. J. Chem. Phys. **116** (2002) 1707.

[152] M. Ohring. *"The Material Science of Thin Films"*. Academic Press. London. 1992.

[153] J. Wollschläger, J. Viernow, C. Tegenkamp, D. Erdös, K.M. Schröder, H. Pfnür. *"Stoichiometry and Morphology of MgO Films grown reactively on MgO"*. Appl .Surf. Sci. **142** (1999) 129.

[154] S. Schintke, S. Messerli, M.Pivetta, F. Patthey, L. Libioulle, M. Stengel, A. De Vita, W.-D. Schneider. *"Insulator at The Ultrathin Limit: MgO on Ag(001)"*. Phys. Rev. Lett. **87** (2001) 267801.

[155] S. Valeri, S. Altieri, U. del Pennino, A. di Bona, P. Luches, A. Rota. *"Scanning Tunneling Microscopy of MgO Ultrathin Films on Ag(001)"*. Phys. Rev. B **65** (2002) 245410.

[156] M. Sterrer, M. Heyde, M. Novicki, N. Nilius, T. Risse, H.-P. Rust, G. Pacchioni, H.-J. Freund. *"Identification of Color Centers on MgO(001) Thin Films with Scanning Tunneling Microscopy"*. J. Phys. Chem. B **110** (2006) 46.

[157] H.L. Meyerheim, R. Popescu, J. Kirschner. N. Jedrecy, M. Sauvage-Simkin, B. Heinrich, R. Pinchaux. *"Geometrical and Compositional Structure at Metal-Oxide Interfaces: MgO on Fe(001)"*. Phys. Rev. Lett. **87** (2001) 076102.

[158] M.-C. Wu, J.S. Corneille, J.-W. He, C.A. Estrada, D.W. Goodman. *"Synthesis and, Characterizations of Ultrathin MgO Films on Mo(001)"*. J. Vac. Sci. Technol. A **10** (1992) 1467.

[159] M.C. Gallagher, M.S. Fyfield, L.A. Bumm, J.P. Cowin, S.A. Joyce. *"Structure of Ultrathin MgO Films on Mo(001)"*. Thin Solid Films **445** (2003) 90.

[160] M. Sterrer, E. Fischbach, T. Risse, H.-J. Freund. *"Geometric Characterization of a Singly Charged Oxygen Vacancy on a Single-Crystalline MgO(001) Film by Electron Paramagnetic Resonance Spectroscopy"*. Phys. Rev. Lett. **94** (2005) 186101.

[161] M. Sterrer, T. Risse, M. Heyde, H.-P. Rust, H.-J. Freund. *"Crossover from Three-Dimensional to Two-Dimensional Geometries of Au Nanostructures on Thin MgO(001) Films: A Confirmation of Theoretical Predictions"*. Phys. Rev. Lett. **98** (2007) 206103.

[162] C.C. Chusuei, D.C. Meier, D.W. Goodman. *"The Chemical Physics of Solid Surfaces: Oxide Surfaces"*, Vol. **9**. Edited by D.P. Woodruff. Elsevier, Amsterdam 2001.

[163] Y.D. Kim, J. Stultz, D.W. Goodman. *"Characterization of MgO(100) thin film growth on Mo(100)"*. Surf. Sci. **50**6 (2002) 228.

[164] B. Hallstedt. *"The Magnesium-Oxygen System"*. CALPHAD **17** (1993) 281.

[165] B. Predel. *"Mg-O (Magnesium-Oxygen)"*. Landolt-Börnstein – Group IV: Physical Chemistry, Volume **5H,** Physics and Astronomy, Springer-Verlag 1997.

[166] P. Franke, D. Neuschütz, Scientific Group Thermodata Europe (SGTE). *"Binary Systems. Part 3: Binary Systems from Cs-K to Mg-Zr"*. Landolt-Börnstein – Group IV: Physical Chemistry, Volume **19B3,** Physics and Astronomy, Springer Berlin Heidelberg 2005.

[167] Magnesium compounds in: *www.webelements.com*.

[168] T.S. Duffy, R.J. Hemley, H.-K. Mao. *"Equation of State and Shear Strength at Multimegabar Pressures: Magnesium Oxides to 227GPa"*. Phys. Rev. Lett. **74** (1995) 1371.

[169] A. Strachan, T. Çağin, and W.A. Goddard III. *"Phase Diagram of MgO from Density-Functional Theory and Molecular-Dynamics Simulations"*. Phys. Rev. B **60** (1999) 15084.

[170] O. Madelung, U. Rössler and M. Schulz. *"Magnesium oxide (MgO) Crystal Structure, Lattice Parameters, Thermal Expansion"*. Landolt-Börnstein – Group III: Condensed Matter, Volume **41B**, Physics and Astronomy, Springer-Verlag 1999.

[171] O. Madelung, U. Rössler and M. Schulz. *"Magnesium oxide (MgO) Energy Gap, Interband Transition Energies"*. Landolt-Börnstein – Group III: Condensed Matter, Volume **41B**, Physics and Astronomy, Springer-Verlag 1999.

[172] V. E. Henrich, P. A. Cox. *"The Surface Science of Metal Oxides"*. Cambridge University Press, Cambridge, 1994.

[173] D. Fritsch, H. Schmidt, M. Grundmann. *"Pseudopotential Band Structures of Rocksalt MgO, ZnO, and $Mg_{1-x}Zn_xO$"*. Appl. Phys. Lett. **88** (2006) 134104.

[174] C. Juna, L. Lin, T. Lu, and L. Yong. *"Electronic Structure of F, F+-center in MgO"*. Eur. Phys. J. B 9 (1999) 593.

[175] A.F. Moodie, C.E. Warble. *"Electron Microscopic Investigations of MgO Morphology and Surfaces"*. J. Crystal Growth **10** (1971) 26.

[176] S. Coluccia, A.J. Tench, R.L. Segall. *"Surface Structure and Surface States in Magnesium Oxide Powders"*. J. Chem. Soc., Faraday Trans. 1, **vol 75** (1979) 1769.

[177] D.P. Norton. *"Synthesis and Properties of Epitaxial Electronic Oxide Thin-Film Materials"*. Mater. Sci. Eng. R **43** (2004) 139.

[178] P.A. Stampe, R.J. Kennedy. *"X-Ray Characterization of MgO Thin Films Grown by Laser Ablation on Yttria-Stabilized Zirconia"*. J. Cryst. Growth **191** (1998) 472.

[179] J.L. Vassent, A. Marty, B. Gilles, C. Chatillon. *"Thermodynamic Analysis of Molecular Beam Epitaxy of MgO(s): I. MgO Vaporization by Electron Bombardment"*. J. Cryst. Growth **219**(2000) 434.

[180] D. Cáceres, I. Colera, I. Vergara, R. González, E. Román. *"Characterization of MgO Thin Films Grown by RF-Sputtering"*. Vacuum **67** (2002) 577.

[181] M. Ritter, W. Ranke, W. Weiss. *"Growth and Structure of Ultrathin FeO Films on Pt(111) studied by STM and LEED"*. Phys. Rev. B **57** (1998) 7240.

[182] M. Henzler. *"Growth of Epitaxial Monolayers"*. Surf. Sci. **357-358** (1996) 809.

[183] J. Wollschläger, D. Erdös, H. Goldbach, K.M. Schröder. *"Growth of NiO and MgO Films on Ag(100)"*. Thin Solid Films **400** (2001) 1.

[184] M. Dynna, J.L. Vassent, A. Marty, B. Gilles. *"A Low-Energy Electron Diffraction Investigation of The Surface Deformation Induced by Misfit Dislocation in Thin MgO Films Grown on Fe(001)"*. J. App. Phys. **80** (1996) 2650.

[185] M. Horn-von Hoegen, A. Al-Falou, H. Piettsch, B.H. Müller, M. Henzler. *"Formation of Interfacial Dislocation Network in Surfactant Mediated Growth of Ge on Si(111) investigated by SPA-LEED"*. Surf. Sci. **298** (1993) 29.

[186] G. Springholz, K. Wiesauer. *"Nanoscale Dislocation Patterning in PbTe/PbSe(001) Lattice-Mismatched Heteroepitaxy"*. Phys. Rev. Lett. **88** (2002) 015507.

[187] D.C. Sayle, C.R.A. Catlow, J.H. Harding, M.J.F. Healy, S.A.M. Maicaneanu, S.C. Parker, B. Slater, G.W. Watson. *"Atomistic Simulation Methodologies for Modeling the Nucleation Growth and Structure of Interfaces"*. J. Mater. Chem. **10** (2000) 1315.

[188] J. Goniakowski, C. Noguera. *"Electronic States and Schottky Barrier Height at Metal/MgO(100) Interfaces"*. Interface Science **12** (2004) 93.

[189] O. Madelung, U. Rössler and M. Schulz. *"Magnesium Oxide (MgO) Young's, Shear and Bulk Moduli, Poisson's Ratio"*. Landolt-Börnstein – Group III: Condensed Matter, Volume **41B**, Physics and Astronomy, Springer-Verlag 1999.

[190] G. Welder, C.M. Schneider, A. Trampert, R. Koch. *"Strain Relief of Heteroepitaxial bcc-Fe(001) Films"*. Phys. Rev. Lett. **93** (2004) 236101.

[191] L. B. Freund, S. Suresh. *"Thin Film Materials: Stress, Defect Formation and Surface Evolution"*. Cambridge University Press, 2003,

[192] A.M. Ferrari, S. Casassa, C. Pisani, S. Altieri, A. Rota, S. Valeri. *"Polar and Non-Polar Domain Borders in MgO Ultrathin Films on Ag(001)"*. Surf. Sci. **588** (2005) 160.

[193] M. Henzler in *"Electron Spectroscopy for Surface Analysis"*. **Vol.4**, edited by H. Ibach, Springer-Verlag Berlin Heidelberg 1977.

[194] K. Heinz. *"LEED and DLEED as Modern Tools for Quantitative Surface Structure Determination"*. Rep. Prog. Phys. 58 (1995) 637.

[195] T. Kizuka.*"Formation and Structural Evolution of Magnesium Oxide Clusters under Electron Irradiation"*. Jpn. J. Appl. Phys. **40** (2001) L 1061.

[196] D.M. Roessler, W.C. Walker. *"Electronic Spectrum and Ultraviolet Optical Properties of Crystalline MgO"*. Phys. Rev. B. **159** (1967) 733.

[197] P.V. Sushko, A.L. Shluger, C.R.A. Catlow. *"Relative Energies of Surface and Defect States: ab initio Calculations for the MgO(001) Surface"*. Surf. Sci. **450** (2000) 153.

[198] Y. Chen, J.L. Kolopus, W.A. Sibley. *"Luminescence of the F^+ Center in MgO*". Phys. Rev. **186** (1969) 865.

[199] G.H. Rosenblatt, M.W. Rowe, G.P. Williams, Jr., R.T. Williams. *"Luminescence of F and F^+ Centers in Magnesium Oxide"*. Phys. Rev. B. **39** (1989) 10309.

[200] J. Kramer, W. Ernst, C. Tegenkamp, H. Pfnür. *"Mechanism and Kinetics of Color Center Formation on Epitaxial Thin Films of MgO"*. Surf. Sci. **517** (2002) 87.

[201] S. Stankic, J. Bernardi, O. Diwald, E. Knözinger. *"Optical Surface Properties and Morphology of MgO and CaO Nanocrystals"*. J. Chem. B. **110** (2006) 13866.

[202] D. Ricci, A. Bongiorno, G. Pacchioni, U. Landman. *"Electron trapping at neutral divacancy sites on the MgO surface"*. Phys. Rev. Lett. **97** (2006) 036106.

[203] J. Schmitt, P. Mächtle, D. Eck, H. Möhwald, C. A. Helm. *"Preparation and Optical Properties of Colloidal Gold Monolayers"*. Langmuir **15** (1999) 3256.

[204] N. Nilius, N. Ernst, H.-J. Freund. *"Photon Emission from Individual Supported Gold Clusters: Thin Film versus Bulk Oxide."* Surf. Sci. **478** (2001) L327.

[205] C.R. Henry, M. Meunier. *"Helium Diffraction Study of the Nucleation and Growth of Supported Metal Clusters"*. Mat. Sci. Engin. A **217** (1996) 239.

[206] M. Sterrer, M. Yulikov, E. Fischbach, M. Heyde, H. P. Rust, G. Pacchioni, T. Risse, H.-J. Freund. *"When the Reporter induces the Effect: Unusual IR Spectra of CO on Au_1/MgO(001)/Mo(001)"*. Angewandte Chemie-Int Ed. **45** (2006) 2630.

[207] G. Pacchioni, L. Giordano, M. Baistrocchi. *"Charging of Metal Atoms on Ultrathin MgO/Mo(100) Films"*. Phys. Rev. Lett. **94** (2005) 226104.

[208] L. Giordano, F. Cinquini, G. Pacchioni. *"Tuning The Surface Metal Work Function by Deposition of Ultrathin Oxide Films: Density functional calculations"*. Phys. Rev. B **73** (2005) 045414.

[209] J.F. Jia, K. Inoue, Y. Hasegawa, W.S. Yang, T. Sakurai. *"Variation of The Local Work Function at Steps on Metal Surfaces studied with STM"*. Phys. Rev. B **58** (1998) 1193.

[210] R. Smoluchowski. *"Anisotropy of the Electronic work Function of Metals"*. Phys. Rev. **60** (1941) 661.

[211] Ch. Sommerhalter, Th.W. Matthes, Th. Glatzel, A. Jäger-Waldau. *"High-Sensitivity Quantitative Kelvin Probe Microscopy by Noncontact Ultra-High-Vacuum Atomic Force Microscopy"*. Appl. Phys. Lett. **75** (1999) 286.

[212] S. Sadewasser, Th. Glatzel, R. Shikler, Y, Rosenwaks, M.Ch. Lux-Steiner. *"Resolution of Kelvin Probe Force Microscopy in Ultrahigh Vacuum: Comparison of Experiment and Simulation"*. Appl. Sur. Sci. **210** (2003) 32.

[213] Th. Glatzel, S. Sadewasser, R. Shikler, Y, Rosenwaks, M.Ch. Lux-Steiner. *"Kelvin Probe Microscopy on III-V Semiconductore: The Effect of Surface Defects on The Local Work Function"*. Mater. Sci. Eng. B**102** (2003) 138.

[214] N. Shibata, M. F. Chisholm, A. Nakamura, S. J. Pennycook, T. Yamamoto, Y. Ikuhara. *"Nonstoichiometric Dislocation Cores in α-Alumina"*. Science **316** (2007) 82.

[215] M. Kim, G. Duscher, N.D. Browning, K. Sohlberg. *"Nonstoichiometry and The Electrical Activity of Grain Boundaries in $SrTiO_3$"*. Phys. Rev. Lett. **86** (2001) 4056.

[216] C.J. Lu, L.A. Bendersky, K. Chang, I. Takeuchi. *"Dissociation and Evolution of Threading Dislocations in Epitaxial $Ba_{0.3}Sr_{0.7}TiO_3$ Thin Films grown on (001) $LaAlO_3$"*. J. Appl. Phys. **93** (2003) 512.

[217] P. Johansson, G. Hoffmann, R. Berndt. *"Light Emission from Na/Cu(111) Induced by a Scanning Tunneling Microscope"*. Phy. Rev. B **66** (2002) 245415.

[218] K. Ito, S. Ohyama, Y. Uehara, S. Ushioda. *"STM Light Emission Spectroscopy of Surface Micro-Structures on Granular Au Films"*. Surf. Sci. **324** (1995) 282.

[219] M.M. Bischoff, M.C. van der Wielen, H. van Kempen. *"STM-induced Photon Emission Spectroscopy of Granular Gold Surfaces in Air"*. Surf. Sci. **400** (1998) 127.

Publications

1. H.M. Benia, M. Guemmaz, G. Schmerber, A. Mosser and J.-C. Parlebas. "*Investigation on Non-Stoichiometric Zirconium Nitrides"*. Appl. Surf. Sci. **200** (2002) 231,

2. H.M. Benia, M. Guemmaz, G. Schmerber, A. Mosser and J.-C. Parlebas. *"Optical Properties of Non-Stoichiometric Sputtered Zirconium Nitride Films"*. Appl. Surf. Sci. **211** (2003) 146,

3. H.M. Benia, M. Guemmaz, G. Schmerber, A. Mosser and J.-C. Parlebas. *"Optical and Electrical Properties of Sputtered ZrN Compounds"*. Catalysis Today **89** (2004) 307**,**

4. N. Nilius, H.M. Benia, C. Salzemann, G. Rupprechter, H.-J. Freund, A. Brioude, and M.-P. Pileni. *"Light Emission Spectroscopy of Self-Assembled Arrays of Silver Nano-Crystals with the STM"*. Chem. Phys. Lett. **413** (2005) 10,

5. H.M. Benia, N. Nilius and H.-J. Freund. *"Effect of Electromagnetic Interactions on Plasmon Excitations in Silver Particle Ensembles"*. Surf. Sci. **600** (2006) L28,

6. S. Benedetti, H.M. Benia, N. Nilius, S. Valeri and H.-J. Freund. *"Morphology and Optical Properties of MgO Thin Films on Mo(001)"*. Chem. Phys. Lett. **430** (2006) 330,

7. H.M. Benia, N. Nilius and H.-J. Freund. *"Photon Mapping of MgO Thin Films with an STM"*. Surf. Sci. **601** (2007) L55,

8. H.M. Benia, X. Lin, H.-J. Gao, N. Nilius and H.-J. Freund. *"Nucleation and Growth of Gold on MgO Thin Films: A Combined STM and Luminescence Study"***.** J. Phys. Chem. C **111**, (2007) 10528,

9. H.M. Benia, P. Myrach, N. Nilius, *"Photon Emission Spectroscopy of Thin MgO Films with the STM: From a Tip-Mediated to an Intrinsic Emission Characteristic"*. New. J. Phys. **10** (2008) 13010.

10. S. Benedetti, P. Torelli, S. Valeri, H.M. Benia, N. Nilius, G. Renaud. *"Structural and Morphological Evolution of Thin MgO Films on Mo(001)"*. Phys. Rev. B **78** (2008) 195411.

11. H.M. Benia, P. Myrach, N. Nilius, H.-J. Freund. *"Morphological, Electronic and Optical Characterization of Ultra-Thin MgO Layers on Mo(001) with the STM"*. In preparation

Lebenslauf

Selbständigkeitserklärung

Hiermit erkläre ich, die vorliegende Arbeit selbständig und ohne fremde Hilfe verfasst und nur die angegebene Literatur und Hilfsmittel verwendet zu haben.

Hadj Mohamed Benia
Berlin, den 25 Juni 2008